THÈSE

En vue de l'obtention du

DOCTORAT DE L'UNIVERSITÉ DE TOULOUSE

Délivré par : *l'Université Toulouse 3 Paul Sabatier (UT3 Paul Sabatier)*

Présentée et soutenue le *25/10/2024* **par :**

Sasank BUDARAJU

Monte Carlo investigations of Dirac and Chiral Spin Liquids

JURY

Frédéric Mila	EPFL, Lausanne	Rapporteur
Andreas Läuchli	EPFL, Lausanne et PSI, Würenlingen	Rapporteur
Michel Caffarel	LCPQ, Toulouse	Membre du Jury
Anne E. B. Nielsen	Aarhus University	Membre du Jury
Karlo Penc	Wigner Research Centre for Physics, Budapest	Membre du Jury
Subhro Bhattacharjee	ICTS, Bengaluru	Membre du Jury
Didier Poilblanc	LPT, Toulouse	Co-directeur
Yasir Iqbal	IIT Madras	Co-directeur
Federico Becca	University of Trieste	Invité

École doctorale et spécialité :
SDM : Physique de la matière - CO090

Unité de Recherche :
Laboratoire de Physique Théorique de Toulouse (UMR 5152)

Directeur(s) de Thèse :
Didier Poilblanc et *Yasir Iqbal*

Rapporteurs :
Frédéric Mila et *Andreas Läuchli*

Abstract

Quantum Spin Liquids (QSLs) are exotic states of matter characterized by their many-body quantum entanglement and emergent fractionalized excitations, whose low energy physics is described using gauge theories. The experimental realization of QSLs in crystalline materials and their existence as stable ground states in spin models have been fundamental and widely studied questions in condensed matter physics in recent years. In this thesis, we employ quantum Monte Carlo simulations to investigate two questions related to QSLs in two dimensions: one focused on gapped spin liquids and the other on gapless spin liquids.

The first question concerns whether Projected Entangled Pair States (PEPS, a type of Tensor Network) can accurately represent Chiral Spin Liquids (CSL). Questions have been raised due to a no-go theorem preventing free fermion PEPS representations of chiral non-interacting states. We construct fermionic PEPS (fPEPS) approximants of Gutzwiller-projected Chern insulators (a type of CSL), and demonstrate that fPEPS (of finite bond dimension) can capture the correct topological ground-state degeneracy of the CSL. Further, more general fPEPS are optimized to describe the CSL phase of a frustrated Heisenberg antiferromagnet, and the chiral edge modes in the entanglement spectrum are shown to follow the predictions from conformal field theory. Consequently, our work provides additional supporting evidence that PEPS can effectively represent CSL phases.

The second question focuses on the nature of low-energy excitations in gapless Dirac Spin Liquids (DSLs), which, unlike gapped spin liquids, lack well-defined fractionalized quasiparticle excitations. Since mean-field descriptions of DSLs may not fully capture their behavior, it is crucial to account for gauge fluctuations beyond the mean-field level. Additionally, the stability of DSLs as ground states in frustrated Heisenberg antiferromagnets remains an unsettled question. In this work, we construct variational ansatzes for low-energy excitations of DSLs. Our results indicate that Heisenberg models on triangular and Kagome lattices support gapless monopole and spinon excitations even after Gutzwiller projection. We also analyze the momentum quantum numbers of the monopoles, before and after projection. Further, the energetics for monopole excitations of generic charge agree remarkably well with field theory computations on the conformal sphere (in the limit of large number of fermion modes). Finally, we construct flux excitations localized on (pairs of) individual plaquettes which are gapped in the thermodynamic limit due to having a large overlap with the Dirac state. All our findings lend support to a stable U(1) Dirac spin liquid in these two frustrated spin models.

Acknowledgements

My PhD has been a wonderful journey of both intellectual and personal growth, and I am deeply indebted to many people who have supported and guided me along the way.

First and foremost, I would like to thank my advisors, Didier Poilblanc, Yasir Iqbal and Federico Becca for their constant guidance, time and support. Daily discussions with them have taught me so much about physics and the research process. Needless to say, none of the work I have carried out would have been possible without their guidance. I leave with a strong desire to improve my knowledge of the subject, and their lessons will strongly guide me in my pursuit.

The environment at LPT has been wonderful, and I have been very lucky to engage in enriching discussions with other faculty members, including Fabien Alet, Sylvain Capponi, Pierre Pujol and Nicolas Laflorencie. I am grateful for their insightful comments and suggestions about my research. The 'Junior Journal Club' seminars offered a valuable space for PhDs and postdocs to engage in informal discussions about the field, which significantly contributed to my learning and growth. I'm grateful to Jeanne Colbois for collaborating with me in initiating these seminars.

A huge thanks to Malika and Mathilde for their patience and efficiency in helping me navigate the numerous (or rather innumerous!) administrative procedures in France. I also owe a great deal to Alejandro Estana, who helped me greatly in setting up numerical simulations and connecting to the high-performance cluster in Toulouse. I began my PhD with no experience in coding, but his constant guidance helped me get up to speed very quickly.

I would like to express my deep gratitude to Sen Niu and Jeanne Colbois for many inspiring discussions, and their patience and generosity in addressing my countless questions. I'm also indebted to them for reviewing parts of this thesis. Thanks also to several of lab members and friends in Toulouse, for lovely discussions during lunch (and at dinners at my home!). Some of them are: Ravi, Bhupen, Sap, Pranay, Alejandro, Clara, Noam, Thomas, Naimo, Faedi, Asmi, Saurav, Aditya and Andreas. I also thank the Toulouse Indian Music Group for including me in various music performances for Indian events in Toulouse, which I greatly enjoyed.

I am extremely grateful for the support of my friends, Ardra, Puneeth, Ruchira, Shradha, Soumya, Varun, Swastika, and Kausthub. Their companionship has given me strength during challenging times. I am also indebdted to Sughosh, Swathi, and Vivek for giving me a home in Toulouse away from India. Finally I thank my parents, my brother and my grandma for their unconditional love and support. Their sacrifices and belief in me have allowed me to get where I am today.

I stand on the shoulders of all the above people, and their contributions have been as crucial to this journey as my own efforts.

TABLE OF CONTENTS

"Don't be afraid of moving slowly, be afraid of standing still."

Milkha Singh

CHAPTER 1

INTRODUCTION

This thesis concerns Quantum Spin Liquids (QSLs), exotic phases of matter that have gained prominence over the past few decades. Quantum spin liquids are most often characterized by their absence of magnetic order even at zero temperature, but as we shall see, exhibit several other exotic properties. These states have significant connections to several important areas in physics and technology, including quantum computing, high-temperature superconductivity, and lattice gauge theories [1–4].

Enormous amount of theoretical work has helped shape our understanding of this subject (gauge theories, QFT, topology…). Additionally, numerical methods have also been devised to represent quantum spin liquid states and look for them in spin models. The latter is crucial because these states are typically beyond the reach of exact analytical solutions (except in rare and beautiful cases). Robust numerical techniques at times can be the only line of attack to understand the physics of real-world spin systems. Despite their power, numerical methods come with limitations and biases that need caution and careful consideration.

Finally, extensive experimental efforts have been made to identify quantum spin liquids in nature, but a universal consensus on a material exhibiting all the predicted characteristics of QSLs has not yet been reached. This is because the low energy behaviour of QSLs are very subtle, characterized by new emergent particles and many-body entanglement - both of which are extremely difficult to study in experiment. Typically, a combination of different techniques (e.g. NMR, Inelastic Neutron Scattering, thermodynamic measurements) must be used to develop a complete picture of a candidate material. Nevertheless, the search continues to be a frontier in condensed matter physics, and the number of QSL candidates has grown substantially in the past decade. Surely the discovery of a true QSL material will be a great achievement of condensed matter physics, and will have profound implications for practical applications.

In this thesis, we shall use numerical techniques (predominantly the variational quantum

monte carlo method) to understand better the properties of some QSLs in two dimensions. Specifically, the two main questions we address in our thesis are:

1. **Can topological properties of gapped chiral spin liquids be faithfully represented using Tensor Networks?**

2. **What are the properties of low energy excitations of Dirac spin liquids?**

In the subsequent chapters, we will describe in more detail the context of the problems we address, why they are important, our results and their implications. To set the stage, in this chapter we give a brief overview into the field of quantum spin liquids. We discuss the main properties of QSLs, and their classification via the projective symmetry group approach, an exactly solvable model, and some experimental considerations.

1.1 Quantum Spin Liquids

The concept of quantum spin liquids (QSLs) has developed over several decades, with different aspects of their behavior gaining prominence at various times. Historically, a QSL was first defined as a system of interacting quantum spins that remains magnetically disordered even at zero temperature due to quantum fluctuations. QSLs were proposed by Anderson in his seminal work [5]. Although QSLs must satisfy the above definition, it may be considered too broad, as it also includes states like Valence Bond Solids (VBS), which, while not breaking spin rotational symmetry, do break some lattice symmetries. To refine the definition, a QSL must not break either lattice or spin rotational symmetry. A state that preserves all symmetries is known as a fully symmetric spin liquid [6]. In this thesis, we will also focus on a different class of spin liquids known as chiral spin liquids, which break time-reversal and parity symmetries, but preserve their combined product (and also preserve spin rotation and lattice symmetries).

From a modern perspective, it has become evident that the defining feature of quantum spin liquids (QSLs) is their entanglement. QSLs cannot be continuously transformed into a trivial product state without crossing a gap-closing phase transition, highlighting their inherent long-range quantum entanglement [1]. Simultaneously, it has been recognized that gauge theories offer a natural framework for understanding these states [7–9]. The introduction of topological order has further refined the classification of spin liquids, giving rise to the concept of topological spin liquids. These states are characterized by the presence of emergent quasiparticles at low energies, which possess fractional quantum numbers. We will discuss an example of such a state in section 1.2.

It is well established that frustrating interactions are a key ingredient for stabilizing quantum spin liquid (QSL) ground states in spin systems [10]. In fact, Anderson's initial proposal for a QSL was based on the nearest-neighbor triangular lattice Heisenberg model. Although it is now known that this particular model has a ground state with magnetic order [11], the inclusion of

both nearest and next-nearest-neighbor interactions indeed stabilizes a QSL phase, which will be explored in Chapter 5 of this thesis. With advances in both theoretical and numerical methods, we now know numerous spin models that host QSL states in their ground state phase diagrams.

Conventional phases of matter are understood through the Landau paradigm of symmetry breaking, where the symmetry groups on either side of a phase transition are related, with one being a subgroup of the other. So, different phases can be distinguished by their respective sets of symmetries [12]. However, quantum spin liquids (QSLs) do not break any symmetries, which raises the question: how can we distinguish different types of spin liquids? The Projective Symmetry Group (PSG) framework provides an answer to this question, and it was introduced by Xiao-Gang Wen in his seminal works [9, 13, 14]. He proposed that "quantum orders," which classify zero-temperature phases of quantum matter, are inherently richer than classical orders because they pertain to the properties of many-body wavefunctions which are generally complex [13]. He pointed out that "internal symmetries," arising from gauge theory, are the key to distinguishing between different spin liquid phases. Here, we will briefly introduce this idea. For more detailed exposition, we direct the interested reader to the sources [9, 13, 15–17].

Consider a spin system governed by a generic Heisenberg hamiltonian $H = \sum_{ij} J_{ij} \vec{S}_i \cdot \vec{S}_j$. The general way to study spin liquids at the mean field level is to use the parton decomposition of the spin operator

$$\vec{S}_i = \frac{1}{2} f^\dagger_{i\alpha} \vec{\sigma}_{\alpha\beta} f_{i\beta} \tag{1.1}$$

where $\vec{\sigma}$ is the vector of Pauli matrices, and we choose f_i to be fermions i.e $\{f_i, f^\dagger_j\} = \delta_{ij}$ [1]. It can be easily verified that the $SU(2)$ commutation relations of the spin operators are satisfied. In this fractionalization picture, each spin is "split" into two fermions, which carry spin 1/2 but not charge. There are two important consequences of the rewriting in equation (1.1). Firstly, the Hilbert space is enlarged to four dimensions at each site, as it now includes unphysical states such as the vacuum and double occupancy. To correctly describe the physical spin model of interest, we must enforce the constraint:

$$f^\dagger_{i\uparrow} f_{i\uparrow} + f^\dagger_{i\downarrow} f_{i\downarrow} = 1 \quad \forall i \tag{1.2}$$

We can now perform a mean-field analysis of the Hamiltonian H. By substituting equation (1.1) into the Heisenberg model, quartic terms emerge, which can be decoupled through mean-field approximations, transforming the problem into a non-interacting one. The gauge fields can then be determined self-consistently. A general mean field 'auxiliary' Hamiltonian would have the

[1] One can also choose to do a parton decomposition in terms of bosons or Majorana fermions. At the mean field level, the descriptions of the spin liquid state depend on the choice of decomposition. However, if all fluctuations are taken into account exactly, then the physics of the spin model is independent of the parton decomposition.

following terms:

$$H = \sum_{\langle i,j\rangle,\sigma} t_{ij} f^\dagger_{i\sigma} f_{j\sigma} + \sum_{\langle i,j\rangle} \Delta_{ij} f^\dagger_{i\uparrow} f^\dagger_{j\downarrow} - \sum_{i,\sigma} \mu_i f^\dagger_{i\sigma} f_{i\sigma} + \text{h.c.} \tag{1.3}$$

The parameters $\{t_{ij}, \Delta_{ij}, \mu_i\}$ constitute a mean-field ansatz for the spin liquid. It is important to note that since the mean-field solution does not lie within the correct Hilbert space of the spin model, gauge fluctuations—at least the temporal ones, which enforce the one-particle-per-site Gutzwiller constraint—must be considered to accurately describe the spin model's physics. These temporal fluctuations can be accounted for exactly using the Variational Monte Carlo (VMC) technique, as will be discussed in chapter 2. When we study excitations of Dirac spin liquids in chapter 5, we will construct them using (simplified) auxiliary Hamiltonians of the above type, followed by Gutzwiller projection using VMC.

The second consequence of the rewriting in (1.1) is the emergence of a gauge symmetry. To see this clearly, consider the object

$$\Phi_i = \begin{pmatrix} c_{i\uparrow} & c_{i\downarrow} \\ c^\dagger_{i\downarrow} & -c^\dagger_{i\uparrow} \end{pmatrix} \tag{1.4}$$

In terms of this composite object, the physical spin operator can be easily written down as ($\alpha = x, y, z$)

$$S^\alpha_i = \frac{1}{4} \text{Tr}\left[\Phi^\dagger_i \Phi_i (\sigma^\alpha)^T\right] \tag{1.5}$$

Now, we observe that the spin operator remains invariant if we make the transformation $\Phi^\dagger_i \to W_i \Phi^\dagger_i$ where W_i represents a local $SU(2)$ transformation. This implies that there is an $SU(2)$ freedom at each site that does not influence the physical observables. This gauge freedom is what allows for the distinction between different spin liquids that possess identical physical symmetries. Mean-field ansatzes related by $SU(2)$ gauge transformations describe the same physical state. We point out that since this gauge freedom arises directly from equation (1.1), it is known as the 'high-energy gauge group'.

Now we are in a position to define the Projective Symmetry Group (PSG) for a given ansatz. The PSG extends the concept of physical symmetry operations to include gauge transformations. Specifically, the PSG is the set of all symmetry operations of the physical system combined with appropriate gauge transformations such that, when applied together, they leave the mean-field ansatz invariant. Therefore, different mean field ansatzes with the same physical symmetries can have different PSGs. Another crucial quantity in the mean-field theory of spin liquids is the Invariant Gauge Group (IGG). The IGG is defined as the group of gauge transformations that leave the mean-field ansatz invariant (this corresponds to the physical symmetry operation being just the identity). It is a normal subgroup of the PSG.

The IGG characterizes the internal gauge redundancy of the quantum spin liquid and plays a fundamental role in determining its low-energy properties. In fact, the fluctuations beyond the mean-field picture are also governed by the IGG. When referring to different spin liquids as $U(1)$, $\mathbb{Z}_2$, etc., we are actually referring to the IGG, and not the high-energy gauge group. For instance,

the Dirac spin liquid ansatz discussed in Chapter 5 has an IGG that is the $U(1)$ group, and is thus called a $U(1)$ spin liquid.

Finally, we end with a remark about phase transitions between different spin liquid phases. Analogous to the Landau symmetry-breaking picture, where the symmetry group of one phase must be a subgroup of the other phase, here the PSG of one phase must be a subgroup of the PSG of the other phase. Thus, the PSG approach provides a robust framework for classifying all possible quantum spin liquid phases at the mean field level, and the possible transitions between them.

1.2 Toric code: an exactly solvable QSL model

Although most theoretical models of spin liquids require numerical study, there are notable exceptions where the ground state and elementary excitations can be derived analytically. In one dimension, the quantum Heisenberg model can be exactly solved using the Bethe ansatz, revealing a disordered, gapless ground state with spinon excitations [18] (which have been observed in experiment! [19]). In two dimensions, Alexei Kitaev's pioneering work introduced two exactly solvable models on the square and honeycomb lattices [20, 21], providing concrete proof that spin liquids can indeed exist as stable ground states in two dimensions. The insights gained from these models are invaluable, offering a deep understanding of the stability and properties of spin liquid phases. In this section, we will explore the toric code model on the square lattice and briefly comment on other related models.

Consider an $L \times L$ square lattice with open boundary conditions, where spin 1/2 degrees of freedom live on the *edges* of the lattice, instead of the vertices. The hamiltonian is defined as

$$H = -\sum_v A_v - \sum_p B_p, \tag{1.6}$$

where A_v acts on the four spins around a vertex v, $A_v = \prod_c \sigma^z$, and B_p acts on the four spins around a plaquette p, $B_p = \prod \sigma^x$ (see figure 1.1 for an illustration). Since each A_v and B_p term is a tensor product of Pauli operators, their eigenvalues are ± 1. It is easily shown that the terms in (1.6) mutually commute. Consequently, all the terms can be simultaneously diagonalized, and the ground state must satisfy $A_v = 1$ and $B_p = 1$ for all vertices v and plaquettes p. Now, there is a simple physical way to picture the ground state. If we interpret states with $\sigma^z = -1$ as the presence of an imaginary "string" on a given edge, then it becomes clear that all A_v constraints can only be satisfied if these "strings" have no endpoints, i.e., they form closed loops. Thus, any configuration of spins corresponding to closed loops of strings represents a ground state of $\sum_v A_v$. What about the plaquette terms? The role of $\sum_p B_p$ is to break this huge degeneracy. The action of B_p on a plaquette p is to create strings where there are none present, and destroy strings where they are present. This implies that for a state to be an eigenstate of a single B_p, it must be of the

form $|\psi\rangle + B_p |\psi\rangle$. Extending this statement to the whole system, it is clear that the ground state of the toric code model is unique, and is given by equal superposition of all loop configurations on the lattice. This state is highly entangled and breaks no symmetries; it is a quantum spin liquid state.

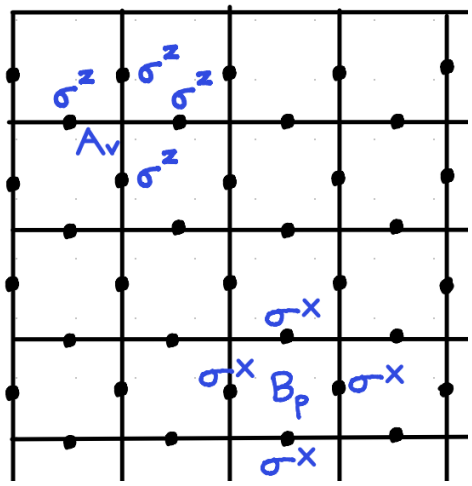

Figure 1.1: Toric code hamiltonian consists of the vertex terms A_v and the plaquette terms B_p acting on spin 1/2 degrees of freedom on the edges of the lattice.

A key feature of the toric code is that its ground state degeneracy depends on the geometry of the space in which the model is defined. When the toric code is placed on a torus, the analysis remains the same as for the planar case, but with an important difference: the ground state becomes four-fold degenerate. This degeneracy arises because, one can construct loops that wind around the incontractible cycles of the torus. Since there are two independent, incontractible loops on a torus, this gives rise to four distinct topological sectors. Each sector is characterized by a $\mathbb{Z}_2$ invariant, which corresponds to the parity of the number of loops that wind around these cycles. Crucially, these four ground states are locally indistinguishable—no local operator can differentiate between them. Only non-local operators, which span the entire lattice, can determine the topological sector. This property leads to the topological stability of the ground states: information stored in which ground state the system occupies is protected against local perturbations, which cannot cause a transition between different sectors. This topological protection is a fundamental feature of the toric code and is a key reason why these states are considered promising for quantum information storage and processing.

Let us move further and study the excitations above the ground state. These excitations manifest as violations of the $A_v = 1$ and $B_p = 1$ constraints. Specifically, violating the constraint at a single vertex (or plaquette) results in the creation of a pair of quasiparticles, termed "electric" e (or "magnetic" m) excitations respectively. These quasiparticles can be thought of as residing on the vertices and centers of plaquettes, and they are always created in pairs. To separate

these excitations, one must apply "string operators," which are products of either σ^zs or σ^xs, as illustrated in Figure 1.2. Remarkably, the energy required to move these excitations infinitely apart is *finite*, as the only energy cost is the initial $\Delta E = +2$ incurred to create the excitations. This property means that the excitations are 'deconfined,' unlike, for instance, domain wall excitations in a ferromagnet.

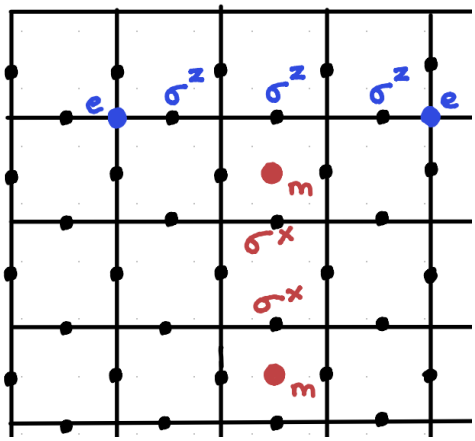

Figure 1.2: Anyon excitations e and m in the toric code. Applications of σ^z and σ^x move the anyons across the lattice with no energy cost.

Further, the phase acquired in the wavefunction by exchanging an e and m particle is $e^{i\pi/2}$, rather than ± 1 (this can be easily shown using the anticommutation relations of Pauli operators). This implies that these particles do not follow conventional fermionic or bosonic statistics! Consequently, the excitations in the toric code are (abelian) anyons, quasiparticles with fractional exchange statistics. These anyonic excitations are supported by the long range entanglement in the system, and are robust to small (even symmetry breaking) perturbations in the Hamiltonian. This phase is termed a "topologically ordered" phase, one characterized by a finite gap to all excitations, a ground state degeneracy that depends on topology of space, and non-local fractional excitations. Topologically ordered phases have been understood to a great extent and show unique signatures in the entanglement entropy [22–25]. In fact, the fractional quantum Hall states are examples of topological ordered states, and also host anyonic excitations (which have very recently been experimentally observed in quantum Hall interferometers! [26]).

We conclude this section with a few remarks. The toric code is, in fact, a realization of a $\mathbb{Z}_2$ lattice gauge theory, where each link hosts a $\mathbb{Z}_2$ variable that can take values ± 1. The ground state of this model corresponds to the deconfined phase of the theory, a $\mathbb{Z}_2$ QSL. Kitaev extended this concept to more general models where the local degrees of freedom are representations of other discrete groups [21]. These models are now known as "quantum double" models and can host *non-abelian* anyonic excitations, which are of great interest for universal quantum computation [27]. Further generalizations have also been developed, where the local degrees of freedom do not necessarily have a group structure. These are based on more general algebraic

structures known as tensor categories and are realized in the Levin-Wen string-net models, which have also been extensively studied [14, 28–31].

In 2006, Kitaev introduced another model on the honeycomb lattice [20], characterized by only two-body interactions, which remains exactly solvable through a mean-field decomposition in terms of Majorana fermions. This model features a richer phase diagram, encompassing both gapless and gapped $\mathbb{Z}_2$ quantum spin liquid (QSL) phases, which host both abelian and non-abelian anyons. Significant ongoing research is focused on experimental realization of these so-called "Kitaev materials."

1.3 Spin liquids and experiments

1.3.1 Candidate materials

The number of spin liquid candidate materials has grown substantially over the past decade. Here we will briefly highlight some key candidates. Our discussion will be limited to materials that are potential hosts for Dirac and chiral spin liquids, as they are the focus of this thesis.

On the Kagome lattice, the compound $ZnCu_3(OH)_6Cl_2$ (known as Herbertsmithite) is possibly the most widely studied [32] QSL candidate. Although it clearly shows a lack of magnetic ordering, the presence of disorder has created difficulties in interpreting experimental results (e.g see [33]). This is a common issue in many QSL materials. Moreover, neutron scattering data has been argued to be explainable by random-singlet states, which are product states and not QSLs [34]. Another Kagome compound recently gaining prominence is $YCu_3(OH)_6Br_2[Br_x(OH)_{1-x}]$ [35], in which signatures of Dirac cones in the spectral factor were recently reported [36]. Coming to the triangular lattice, the spin-orbit-coupled insulator $YbMgGaO_4$ has garnered significant attention [37–42]. However, there remains debate, with alternative proposals for a spin glass phase stabilized by onsite Mg/Ga disorder [43–46]. Sodium chalcogenides $NaYbX_2$ (X = S, O, Se) are free from structural disorder and are emerging as prominent spin liquid candidates [47–52]. Finally, organic salts such as $\kappa(ET)_2Cu_2(CN)_3$ [53] and $EtMe_3Sb[Pd(dmit)_2]_2$ [54] (figure 1.4) show encouraging results. The most recent proposal has been the compound $YbZn_2GaO_5$ [55] (discussed in figure 1.5).

Turning to chiral spin liquids, significant attention has been focused on spin-orbit coupled materials under external magnetic fields [2, 56, 57]. This interest stems from the pioneering proposal by Jackeli and Khaliullin [58], who suggested that the bond-dependent Kitaev interactions could actually be realized in real materials with strong spin-orbit coupling, such as certain iridates and ruthenates. These interactions have since been identified as crucial in the search for chiral spin liquids. Additionally, in Moiré heterostructures, the layer degree of freedom regarded as a pseudo-spin facilitates realization of pseudo-chiral spin liquids [59].

Finally, we note as an aside that the realization of spin liquids in quantum simulator platforms is a rapidly developing area of research [60]. There has been a surge of exciting work demonstrating the possibility of realizing toric code topological order in Rydberg atom arrays [61–64]. Additionally, chiral spin liquids have been proposed in cold atom systems using Floquet driving [65] (see also [66]) and in Rydberg arrays [67–70], where the chirality of edge modes can be experimentally detected. These platforms offer a promising avenue for the realization of spin liquid states and their controlled manipulation.

1.3.2 Experimental techniques and signatures

Detecting QSLs in experiments presents a significant challenge, primarily due to the difficulty in probing their non-local excitations and many-body entanglement. While experimental techniques are highly effective at studying local excitations, probing non-local ones is much more challenging. There is no single 'smoking-gun' signature that can unambiguously confirm the presence of a QSL in a material. Instead, researchers typically rely on a combination of different experimental techniques to build a case for QSL behavior. Below, we briefly summarize a few experimental methods and the associated signatures that are indicative of QSLs. A more comprehensive discussion can be found in the reviews [1, 3, 71].

1. **Neutron Scattering** is one of the most powerful techniques for investigating magnetic materials and has been extensively used in the search for QSLs. The quantity probed by the experiment is the dynamical spin structure factor $S(q,\omega)$, given by

$$\mathbf{S}(q,\omega) = \sum_{\text{exc}} \left| \langle \Psi^q_{\text{exc}} | \mathbf{S}_q | \Psi_g \rangle \right|^2 \delta(\omega - E^q_{\text{exc}} + E_g) \tag{1.7}$$

   where $|\Psi\rangle_g$ is the ground state with energy E_g, and the summation is over all excited states at wavevector q, with energies E^q_{exc}. In conventional magnetically ordered systems, the structure factor exhibits sharp peaks at specific momentum points corresponding to the ordering vector. In contrast, neutron scattering experiments on QSL candidates typically reveal a broad continuum of excitations rather than discrete magnon peaks. This continuum suggests the presence of fractionalized excitations, such as spinons, which are a hallmark of QSLs. An example of Herbertsmithite, a famous Kagome lattice QSL candidate, is shown in figure 1.3. We note however that the broad continuum could also be caused by other factors like impurities and disorder, and it is important to rule out these effects.

2. **Nuclear Magnetic Resonance (NMR)** is a technique that probes the local environments of nuclear moments within a material. By applying sequences of magnetic field pulses, NMR manipulates the net nuclear magnetization, and studies its response. The relaxation of the longitudinal magnetization back to equillibrium is characterized by a parameter T_1. This quantity encodes information about the hyperfine coupling between nuclear and surround-

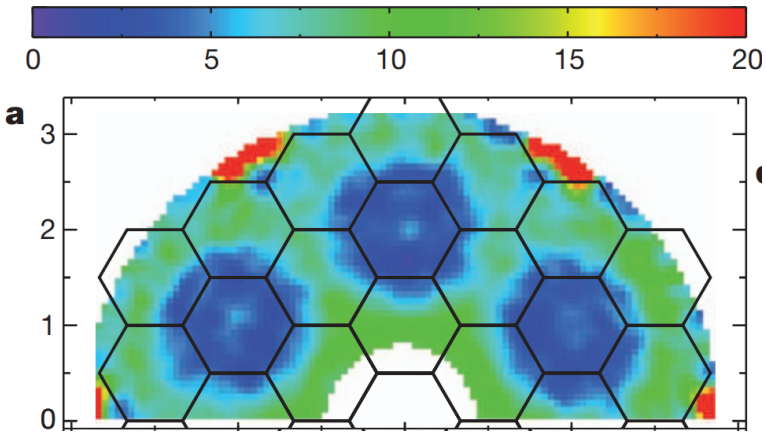

Figure 1.3: Inelastic neutron scattering experiments on Herbertsmithite, revealing a continuum of low energy excitations in the Brilluoin zone. Figure taken from [72].

ing electronic spins, and is directly connected to the spin susceptibility. In magnetically ordered states, T_1 typically exhibits a pronounced increase near the ordering temperature, signaling the onset of magnetic order. In contrast, in T_1 displays broad features in disordered states. See figure 1.4 for results on the triangular lattice antiferromagnetic QSL candidate $EtMe_3Sb[Pd(dmit)_2]_2$. Additionally, we note that broadening or splitting in the "chemical shift" can serve as further evidence of magnetic ordering.

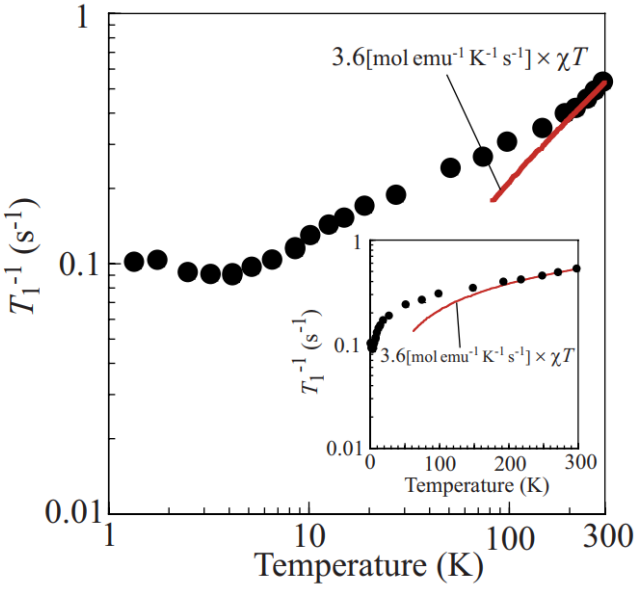

Figure 1.4: Behavior of the NMR relaxation rate T_1 for the compound $EtMe_3Sb[Pd(dmit)_2]_2$ as a function of temperature. Deviation from linear behavior as temperature is reduced from $200K$ indicates increasing antiferromagnetic correlations. Figure taken from [73].

3. **Specific heat measurements** are a valuable tool for investigating quantum spin liquids (QSLs). Phase transitions as a function of temperature are clearly revealed by divergences of the specific heat. Additionally, the low-temperature behavior of the magnetic specific heat provides insights into the nature of the phase. For gapped phases, it exhibits an exponential suppression, while for gapless QSLs, it follows a power-law behavior, with an exponent depending on the underlying gauge structure of the theory. For example, a $c_v \sim T^2$ behavior is predicted for Dirac spin liquids [74], and has recently been observed in the candidate $YbZn_2GaO_5$ [55], see figure 1.5.

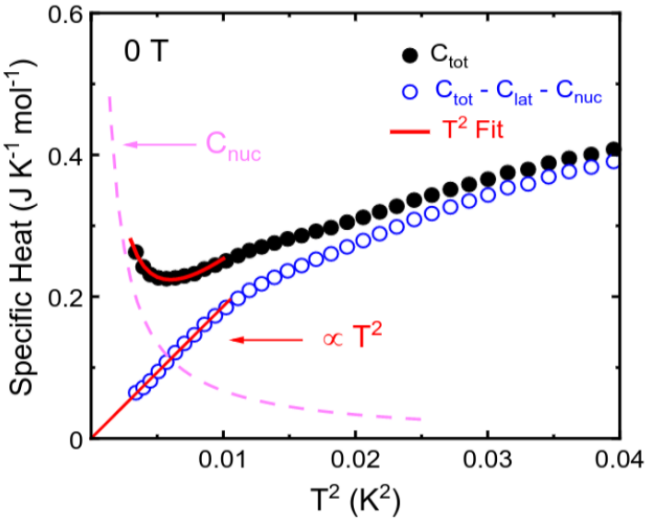

Figure 1.5: Specific heat measurements of the triangular lattice compound $YbZn_2GaO_5$. The magnetic specific heat (blue open circles) is obtained after subtracting the lattice and nuclear Schottky contributions, and shows a T^2 dependence. Figure taken from [55].

In addition to these methods, techniques such as muon spin resonance (μSR), Raman scattering, and optical methods are also employed to study QSLs.

1.4 Thesis outline

With the brief introduction to spin liquids established, we now turn to the core content of this thesis. The structure of the thesis is as follows: in Chapters 2 and 3, we introduce the numerical methods central to this work, namely Variational Monte Carlo (VMC) and Tensor Networks (TN). These two methods are among the most widely used techniques for studying lattice systems and are particularly effective for approximating ground states and low-energy excitations of spin models. The primary technique employed throughout this thesis is VMC, which we utilize to investigate the topological properties of fermionic Projected Entangled Pair States (PEPS)

ansatzes in Chapter 4, and study the energetics of monopole excitations in Dirac spin liquids in Chapter 5. These two chapters, 4 and 5, contain the key results of this thesis.

In the final chapter, 6, we offer concluding remarks, summarizing the insights gained and outlining potential directions for future research. A list of publications resulting from the work presented in this thesis can be found in Chapter 7, and a brief summary of the thesis in French is provided in Chapter 8.

CHAPTER 2

VARIATIONAL MONTE CARLO

In this chapter, we give a basic overview into the numerical method used throughout this thesis: the Variational Monte Carlo (VMC) technique. VMC is a powerful method for investigating the zero-temperature phase diagrams, ground states and low-energy excitations of quantum many-body systems.

Originating in the 1960s, VMC was initially developed to study the ground state of liquid helium [75–77]. Since then, it has become a standard technique across many fields including nuclear physics [78], quantum chemistry [79], and strongly correlated systems [80]. Sophisticated optimization schemes (e.g., stochastic reconfiguration [81, 82]) have enabled the study of variational wavefunctions with a large number of parameters. Recent progress has also involved integrating VMC sampling techniques with neural network ansatzes [83–85]. In some cases, VMC has also been combined with tensor network states to leverage the advantages of both methods [86–88]. Indeed, this will be the subject of chapter 4 of this thesis.

VMC is particularly suited to study spin liquids, because starting from tight-binding models of spinons/partons, Gutzwiller projection can be implemented exactly to construct variational wavefunctions that live in the spin Hilbert space. Different spin liquid states with the required lattice and gauge symmetries can be constructed according to the projective symmetry group (PSG) classification discussed in the previous chapter. Since we work directly at zero temperature, the VMC technique does not suffer from the infamous 'sign problem' [89], and thus places no restriction on the terms in the Hamiltonian. Given that frustration is a key factor in stabilizing spin liquid phases, VMC proves to be a powerful tool for investigating such systems.

In this section, we will discuss the VMC method in detail, highlighting its basic principles, strengths and limitations. The treatment here is borrowed from [80], and is restricted to ansatzes with $SU(2)$ spin rotational symmetry. Some examples and additional considerations relevant to this thesis are also mentioned. Before delving into this method, we note that Quantum Monte

Carlo is a generic term that encompasses a wide range of techniques, each tailored to study different systems, with distinct advantages and limitations. These methods all involve stochastic sampling, typically either of the system's configuration space or paths in the partition function. Here is a brief one-line summary of some other methods not discussed in this chapter:

- Diffusion Monte Carlo (DMC): This method solves the continuous space Schrödinger equation using multiple random walkers in real space, whose movement is controlled by the potential energy landscape [90].

- Auxiliary Field Monte Carlo (AFMC): AFMC introduces auxiliary fields to transform an interacting problem into a non-interacting one coupled to these fields (through the Hubbard-Stratanovich transformation). These auxiliary fields are then sampled to compute observables [91, 92].

- Green's function Monte Carlo: This method is used to project out the ground state wavefunction by iteratively applying the Green's function to a trial wavefunction (power method) [81].

- Path Integral Monte Carlo (PIMC): samples paths in imaginary time to calculate the partition function and thermodynamic properties at finite temperatures [89].

2.1 Main Idea

At its core, VMC begins with a family of trial wavefunctions $|\Psi(\{\alpha_i\})\rangle$ parameterized by a set of variational parameters $\{\alpha_i\}$ proposed to describe the ground state of a system H of interacting particles. Monte Carlo sampling is then employed to compute the variational energy of these wavefunctions

$$E = \frac{\langle\Psi|H|\Psi\rangle}{\langle\Psi|\Psi\rangle} \tag{2.1}$$

The variational principle of quantum mechanics guarantees that E is bounded from below by the true ground state energy E_{gs} of the system. Therefore, by optimizing the variational parameters $\{\alpha_i\}$, the technique seeks to minimize the energy, thereby achieving the best approximation to the ground state within the chosen family of wavefunctions.

Consider a system of N spin 1/2 particles on a lattice. The Hilbert space describing the states of this system is 2^N dimensional. Therefore, for systems of even moderate sizes, the computer memory required for storing the many body Hamiltonian and wavefunction explodes [1]. It is clear that the above expectation value cannot be evaluated exactly.

[1] A spin 1/2 system with 20 sites would require roughly 8.7TB of memory to store the Hamiltonian.

To combat this difficulty, we recast the expectation value by introducing an identity $\mathbb{I} = \sum_x |x\rangle \langle x|$

$$\begin{aligned} \frac{\langle \Psi | H | \Psi \rangle}{\langle \Psi | \Psi \rangle} &= \sum_x \frac{|\langle x | \Psi \rangle|^2}{\langle \Psi | \Psi \rangle} \frac{\langle x | H | \Psi \rangle}{\langle x | \Psi \rangle} \\ &\equiv \sum_x p(x)\, e_L(x) \end{aligned} \tag{2.2}$$

where $p(x)$ is a normalized probability distribution

$$p(x) = \frac{|\langle x | \Psi \rangle|^2}{\langle \Psi | \Psi \rangle} \tag{2.3}$$

and $e_L(x)$ is termed the local estimator of H

$$e_L(x) = \frac{\langle x | H | \Psi \rangle}{\langle x | \Psi \rangle} \tag{2.4}$$

The above equation (2.2) is exact if we sum over all basis states $|x\rangle$ in the Hilbert space, which is clearly unfeasible. However, we only choose a tiny subset[2] of the whole space, and this choice is made by *sampling* the probability distribution using standard Monte Carlo procedures e.g. Metropolis algorithms. Thus, if the sampling can be performed, the estimate for the variational energy is given by

$$\langle H \rangle = \frac{1}{M} \sum_{\{x_i\}}^{M} e_L(x_i) \tag{2.5}$$

where $\{x_i\}$ is the set of all M states accessed by the Markov chain. The local estimator is typically evaluated by introducing another complete set of states, as follows

$$\frac{\langle x | H | \Psi \rangle}{\langle x | \Psi \rangle} = \sum_{x'} \langle x | H | x' \rangle \frac{\langle x' | \Psi \rangle}{\langle x | \Psi \rangle} \tag{2.6}$$

If the Hamiltonian involves local interactions (as will be the case in the spin systems we study), then the quantity $\langle x | H | x' \rangle$ will be non-zero for very few $|x'\rangle$, and is easy to evaluate. Then the main quantity at the heart of all VMC simulations is the overlap ratio

$$\boxed{O(x', x) = \frac{\langle x' | \Psi \rangle}{\langle x | \Psi \rangle}} \tag{2.7}$$

This quantity also is central to the metropolis algorithm, where the acceptance probability of the move $|x\rangle \to |x'\rangle$ depends on the ratio

$$\frac{p(x')}{p(x)} = \left| \frac{\langle x' | \Psi \rangle}{\langle x | \Psi \rangle} \right|^2 \tag{2.8}$$

[2]For a system with 40 sites, a long Monte Carlo run would involve around 10^7 samples, but the size of the Hilbert space is around 10^{12} meaning we only access 0.001% of all states! This fraction reduces even further with increasing system size.

The intuition behind this is that the primary contributions to the average in (2.2) come from the states $|x\rangle$ that are near the maxima of $p(x)$. Consequently, the Metropolis algorithm increases the likelihood of sampling those configurations which have a significant overlap with $|\Psi\rangle$, thereby enhancing the accuracy of the approximation.

In the subsequent sections, we will discuss how to evaluate the overlaps in (8.7) and how to build a general Monte Carlo simulation. Before doing so, we note that another crucial observable to keep track of is the variance, given by

$$\sigma^2 = \frac{\langle\Psi|H^2|\Psi\rangle}{\langle\Psi|\Psi\rangle} - E^2 = \frac{\langle\Psi|(H-E)^2|\Psi\rangle}{\langle\Psi|\Psi\rangle} \tag{2.9}$$

This quantity vanishes if $|\Psi\rangle$ is an exact eigenstate of H. Therefore, the variance is a useful measure because it has a clear lower bound of zero. During a typical VMC optimization, both the energy and variance are tracked, and they reduce as the optimization progresses. Additionally, the variational energy typically depends linearly on the variance for small values of the latter: $E \approx E_{\text{gs}} + \text{const} \times \sigma^2$. An example run is shown in Figure 2.1, where an initial variational ansatz is optimized using Lanczos steps. [3]

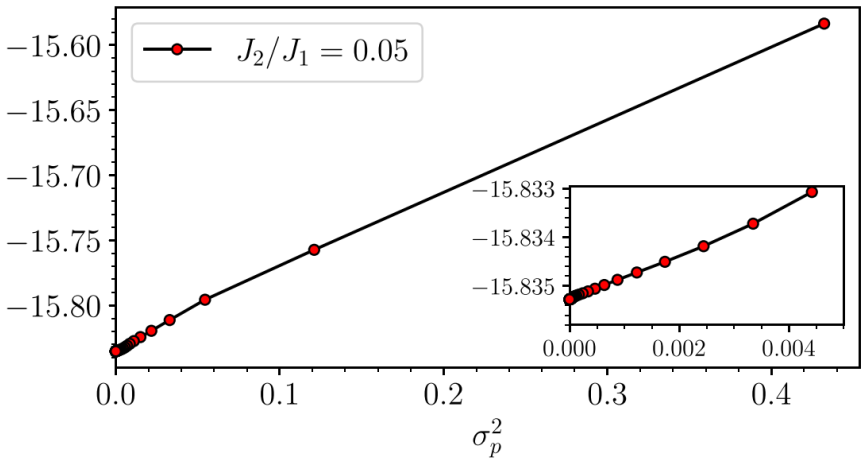

Figure 2.1: Energy as a function of variance for the $J_1 - J_2$ model on the Kagome lattice for a system of 36 sites. The Dirac wavefunction is optimized using repeated Lanczos steps. Figure taken from [93].

2.2 Overlap as a Slater determinant

As described in the previous chapter, one approach to build variational wavefunctions for QSLs is to begin with an auxiliary non-interacting Hamiltonian in terms of the partons, evaluate its

[3] The Lanczos method involves iteratively applying the Hamiltonian to the variational ansatz, systematically taking it toward the ground state. In the limit of infinite Lanczos steps, this method projects any generic wavefunction exactly to the ground state (assuming the initial state was not orthogonal to the ground state).

ground state, and then perform a Gutzwiller projection of the ground state onto the subspace of the spins (one spin per site). In this spirit, let us consider a simple example of a mean field hamiltonian:

$$H_{\mathrm{MF}} = \sum_{i,j,\sigma} \chi_{ij}\, c^{\dagger}_{i,\sigma} c_{j,\sigma} + \mathrm{h.c.} \tag{2.10}$$

where i, j denote spins on a lattice with N sites, and $\sigma = \{\uparrow, \downarrow\}$ is the spin index. We choose hoppings χ_{ij} to be independent of σ for simplicity, ensuring spin rotational symmetry. This hamiltonian can be easily diagonalized, to obtain the single-particle orbitals $\phi^{\dagger}_{\alpha,\sigma}$

$$\phi^{\dagger}_{\alpha,\sigma} = \sum_{R=1}^{N} U_{R\alpha} c^{\dagger}_{R\sigma} \tag{2.11}$$

The matrix U is the $N \times N$ eigenvector matrix obtained by diagonalizing H_{MF} in one spin sector. We then construct the mean field ground state by filling the lowest energy eigenstates upto the Fermi level.

$$|\Phi\rangle = \left[\prod_{\alpha=1}^{N/2} \phi^{\dagger}_{\alpha,\uparrow}\right] \left[\prod_{\alpha=1}^{N/2} \phi^{\dagger}_{\alpha,\downarrow}\right] |0\rangle \tag{2.12}$$

This is the starting point of a VMC simulation. Generically, this wavefunction will contain terms with two (or zero) particles on some site. To obtain a valid spin wavefunction, we must apply the Gutzwiller projector, $|\Psi\rangle = P_G |\Phi\rangle$ that eliminates these unphysical configurations. In the simulation, we compute the overlaps of the wavefunction $|\Psi\rangle$ with a generic configuration $|x\rangle$

$$|x\rangle = \left[c^{\dagger}_{r_1\uparrow} c^{\dagger}_{r_2\uparrow} \ldots\right] \left[c^{\dagger}_{r'_1\downarrow} c^{\dagger}_{r'_2\downarrow} \ldots\right] |0\rangle \tag{2.13}$$

where $\{r_i\}$ ($\{r'_i\}$) is a list of the locations of the up (down) spins. All elements within both the lists must be distinct according to Pauli's exclusion. In the case where $|x\rangle$ has no sites with vacancies or double occupancies, it is easy to see that the overlaps $\langle x|\Phi\rangle$ and $\langle x|\Psi\rangle$ coincide. In the models considered in this thesis, this condition is always satisfied. Thus, by sampling only those $|x\rangle$ that lie in the subspace containing one particle per site, the Gutzwiller projection is taken into account implicitly in the VMC algorithm.

Focusing on the unprojected wavefunction, let us compute the overlap $\langle x|\Phi\rangle$. Clearly, we can break it down into separate calculations for each spin sector. It turns out that each of these overlaps are given by the determinant of a smaller matrix constructed out of U (Slater determinants). We shall first provide an example, and then state the general result.

Example: Consider a lattice of 6 sites, and the following configuration of spins

$$|x\rangle = \left[c^{\dagger}_{1\uparrow} c^{\dagger}_{4\uparrow} c^{\dagger}_{5\uparrow}\right] \left[c^{\dagger}_{2\downarrow} c^{\dagger}_{3\downarrow} c^{\dagger}_{6\downarrow}\right] |0\rangle \equiv |\uparrow\downarrow\downarrow\uparrow\uparrow\downarrow\rangle \tag{2.14}$$

Let us compute the overlap separately for each spin flavor. For the ↑ spin, we get

$$\begin{aligned}&\langle 0|\left[c_{5\uparrow}c_{4\uparrow}c_{1\uparrow}\right]\left[\phi^{\dagger}_{1\uparrow}\phi^{\dagger}_{2\uparrow}\phi^{\dagger}_{3\uparrow}\right]|0\rangle \\ &= \langle 0|\left[c_{5\uparrow}c_{4\uparrow}c_{1\uparrow}\right]\Big[\Big(\sum_{p=1}^{6}U_{p1}\,c^{\dagger}_{p\uparrow}\Big)\Big(\sum_{q=1}^{6}U_{q2}\,c^{\dagger}_{q\uparrow}\Big)\Big(\sum_{r=1}^{6}U_{r3}\,c^{\dagger}_{r\uparrow}\Big)\Big]|0\rangle\end{aligned} \tag{2.15}$$

Clearly, the only non-zero contributions to the above term arise when the set $\{p,q,r\}$ is some permutation of the set $\{1,4,5\}$. Keeping track of the fermion signs, one can easily obtain

$$\begin{aligned}\langle 0|\left[c_{5\uparrow}c_{4\uparrow}c_{1\uparrow}\right]\left[\phi^{\dagger}_{1\uparrow}\phi^{\dagger}_{2\uparrow}\phi^{\dagger}_{3\uparrow}\right]|0\rangle &= U_{11}U_{42}U_{53}-U_{11}U_{43}U_{52} \\ &+U_{41}U_{52}U_{13}-U_{41}U_{12}U_{53}+U_{51}U_{12}U_{43}-U_{51}U_{42}U_{13} \\ &= \det\begin{bmatrix}U_{11} & U_{12} & U_{13}\\ U_{41} & U_{42} & U_{43}\\ U_{51} & U_{52} & U_{53}\end{bmatrix}\end{aligned} \tag{2.16}$$

A similar calculation for the ↓ spin would yield

$$\langle 0|\left[c_{6\uparrow}c_{3\uparrow}c_{2\uparrow}\right]\left[\phi^{\dagger}_{1\downarrow}\phi^{\dagger}_{2\downarrow}\phi^{\dagger}_{3\downarrow}\right]|0\rangle = \det\begin{bmatrix}U_{21} & U_{22} & U_{23}\\ U_{31} & U_{32} & U_{33}\\ U_{61} & U_{62} & U_{63}\end{bmatrix} \tag{2.17}$$

Therefore, the total overlap is a product of two determinants

$$\langle x|\Phi\rangle = \det\begin{bmatrix}U_{11} & U_{12} & U_{13}\\ U_{41} & U_{42} & U_{43}\\ U_{51} & U_{52} & U_{53}\end{bmatrix}\det\begin{bmatrix}U_{21} & U_{22} & U_{23}\\ U_{31} & U_{32} & U_{33}\\ U_{61} & U_{62} & U_{63}\end{bmatrix} \tag{2.18}$$

The above calculation additionally illustrates that the ordering of spin operators in $|x\rangle$ can affect the sign of the overlap. Therefore, to avoid errors - one typically chooses a convention to order the spins, and sticks to this convention throughout the simulation.

Now it is intuitive that generically for N particles, one can write the overlap as

$$\boxed{\langle x|\Phi\rangle = \det U_{\{R^{\uparrow}\alpha\}}\,\det U_{\{R^{\downarrow}\alpha\}}} \tag{2.19}$$

where $R^{\uparrow}$ ($R^{\downarrow}$) denotes the positions of all ↑ (↓) spins, α denotes the orbitals occupied, and $U_{\{R^{\uparrow}\alpha\}}$ is the notation we use for the submatrix of U. We remind the reader that if the system doesn't have SU(2) symmetry in (2.10), one must work in the larger space of $2N\times 2N$ matrices, and the above equation will have just one determinant, since there will generically be mixing between the ↑ and ↓ spin sectors.

2.3 Fast update

We know that the overlaps $\langle x|\Phi\rangle$ are central to a VMC simulation. However, they are rather costly to compute: evaluating the determinant of a $N \times N$ matrix involves $O(N^3)$ operations. However, notice that the simulation only requires ratios of overlaps: $\frac{\langle x'|\Phi\rangle}{\langle x|\Phi\rangle}$. Therefore, if the configurations $|x'\rangle$ and $|x\rangle$ are only slightly different, one could imagine that there might be a more cost effective method to compute this ratio.

Indeed, this is the case. Usually, in the metropolis algorithm, a new configuration $|x'\rangle$ is proposed by acting the Hamiltonian on a couple of spins. When we're dealing with Heisenberg-like models, the most natural choice is to pick a random bond of the lattice, and exchange both spins on the bond (if they are different) [4]. Let's discuss first a single electron hopping process with the previous example: $|x\rangle = |\uparrow\downarrow\downarrow\uparrow\uparrow\downarrow\rangle$. Suppose we propose a new configuration

$$|x'\rangle = c^\dagger_{6\uparrow} c_{4\uparrow} |x\rangle = \left[c^\dagger_{1\uparrow} c^\dagger_{6\uparrow} c^\dagger_{5\uparrow}\right]\left[c^\dagger_{2\downarrow} c^\dagger_{3\downarrow} c^\dagger_{6\downarrow}\right]|0\rangle = -\left[c^\dagger_{1\uparrow} c^\dagger_{5\uparrow} c^\dagger_{6\uparrow}\right]\left[c^\dagger_{2\downarrow} c^\dagger_{3\downarrow} c^\dagger_{6\downarrow}\right]|0\rangle \tag{2.20}$$

What would be the ratio of overlaps $\frac{\langle x'|\Phi\rangle}{\langle x|\Phi\rangle}$? Clearly the $\downarrow$ spins have not been affected, so the determinants of the $\downarrow$ spin cancel in the ratio. For the $\uparrow$ spin, we must compute the ratio

$$\frac{\det \begin{bmatrix} U_{11} & U_{12} & U_{13} \\ U_{61} & U_{62} & U_{63} \\ U_{51} & U_{52} & U_{53} \end{bmatrix}}{\det \begin{bmatrix} U_{11} & U_{12} & U_{13} \\ U_{41} & U_{42} & U_{43} \\ U_{51} & U_{52} & U_{53} \end{bmatrix}} = \frac{\det U_{\{R'^{\uparrow}\alpha\}}}{\det U_{\{R^{\uparrow}\alpha\}}} \tag{2.21}$$

Expanding the above, we get

$$\frac{\langle x'|\Phi\rangle}{\langle x|\Phi\rangle} = \frac{\left[U_{61}(U_{13}U_{52} - U_{12}U_{53}) + U_{62}(-U_{13}U_{51} + U_{11}U_{53}) + U_{63}(U_{12}U_{51} - U_{11}U_{52})\right]}{\det U_{\{R^{\uparrow}\alpha\}}} \tag{2.22}$$

It turns out that the above expression can be rewritten exactly as

$$\sum_{\beta=1}^{3} U_{6\beta} \left(U^{-1}_{\{R^{\uparrow}\alpha\}}\right)_{\beta,2} \tag{2.23}$$

The two numbers highlighted in red are crucial: they refer to the location to which the $\uparrow$ spin has hopped (6), and the position of the electron which hopped, in the ordering of the state (2.14) (the

[4] For the discussion that follows, one could also pick two random locations on the lattice and flip their spins.

$c^\dagger_{4\uparrow}$ was second in the list of up spins) [5]. Therefore, if one defines the matrix

$$W^\uparrow_{Ij} = \sum_\beta U_{I\beta} \left(U^{-1}_{\{R^\uparrow \alpha\}}\right)_{\beta,j} \tag{2.24}$$

Then we have exactly [6]

$$\frac{\langle x'|\Phi\rangle}{\langle x|\Phi\rangle} = W^\uparrow_{62} \tag{2.25}$$

Therefore, elements of this matrix can directly give us the ratios of the overlaps. Defining and keeping track of this matrix in the Monte Carlo routine forms what is known as the 'fast update' in VMC. For clarity, we state some properties of the W matrix below:

- The W matrix depends on both the ansatz wavefunction and the configuration $|x\rangle$. In the current example with SU(2) symmetry, it is defined separately for the $\uparrow$ and $\downarrow$ spin. Note also that it is rectangular, having dimensions 6×3 in this example.
- It can be verified that the elements $W^\uparrow_{51}, W^\uparrow_{12}, W^\uparrow_{52}, W^\uparrow_{41}$ are exactly 0, consistent with the Pauli's exclusion principle: an $\uparrow$ spin cannot move to a site where there is already an $\uparrow$ spin present.
- Further, $W^\uparrow_{11} = W^\uparrow_{42} = W^\uparrow_{53} = +1$, consistent with the fact that such a hopping process does not change the state $|x\rangle$.

However, we are not yet done. The W matrix also requires $O(N^3)$ operations to compute. Since it depends on $|x\rangle$, it must be modified once a new configuration is accepted in the metropolis algorithm. This seems to suggest that we have not made any progress: if one must compute this matrix at every configuration, isn't it simpler to calculate the determinants $\langle x'|\Phi\rangle$ and $\langle x|\Phi\rangle$ separately and take their ratio?
The trick lies in the fact that the W matrix does not have to be computed from scratch; it can be 'updated' in just $O(N^2)$ operations. In our toy example, if the move $|x\rangle \to |x'\rangle$ is accepted, then the W matrix changes as [7]

$$W^\uparrow_{Ij} \to W'^\uparrow_{Ij} = W^\uparrow_{Ij} - \frac{W^\uparrow_{I2}}{W^\uparrow_{62}} \left(W^\uparrow_{6j} - \delta_{2j}\right) \tag{2.26}$$

We will not prove the above equation. However, we will argue that it makes sense because of the following properties of W':

- $W'^\uparrow_{62} = 1$, consistent with the fact that the second $\uparrow$ electron is already present on the 6th site in $|x'\rangle$.

[5] Now we can see that it is crucial to keep track of the ordering of the spins to get the correct fermion sign.

[6] We caution that the two matrix indices of W are on different footing: the first index denotes a site on the real space lattice, and the second index refers the "position index" of the electron of a given spin. It's certainly possible (and common) to find the "first" $\uparrow$ spin at the site 20, and the "second" $\uparrow$ spin at site 1 at some point in the Markov chain.

[7] We emphasise that this is not an approximation, the updating is exact.

- $W'^{\uparrow}_{6j} = \delta_{2j}$, since no other $\uparrow$ spin can now move to site 6.
- $W'^{\uparrow}_{52} = W'^{\uparrow}_{12} = 0$ again due to Pauli's exclusion.
- $W'^{\uparrow}_{I2} = W^{\uparrow}_{I2}/W^{\uparrow}_{62}$. This makes sense if we go back to (2.21). Let's define $|x'_6\rangle$ and $|x'_I\rangle$ as configurations where the second $\uparrow$ spin has moved to sites 6 and I respectively. Rewriting the RHS, we have

$$\frac{W^{\uparrow}_{I2}}{W^{\uparrow}_{62}} = \frac{\frac{\langle x'_I|\Phi\rangle}{\langle x|\Phi\rangle}}{\frac{\langle x'_6|\Phi\rangle}{\langle x|\Phi\rangle}} = \frac{\langle x'_I|\Phi\rangle}{\langle x'_6|\Phi\rangle} \equiv W'^{\uparrow}_{I2} \tag{2.27}$$

  The last equivalence makes sense because $W'^{\uparrow}_{I2}$ physically represents the process where the second $\uparrow$ spin (which is now in position 6) is now going to move to site I.

For a comprehensive proof of the (2.26), including ansatzes that break $SU(2)$ symmetry, we refer the reader to [80]. Nevertheless, the gist of our discussion above is that the W matrix can indeed be updated in $O(N^2)$ operations, therefore obtaining a factor of N reduction in the computational complexity of the algorithm. For example, for the 10×10 triangular lattice, the time taken to reach 10^6 Monte Carlo steps in both methods is

10^6 steps	Determinants from scratch	Fast Update
Time	660 min	35 min

As the system size increases, computing determinants from scratch becomes increasingly impractical [8]. Therefore, fast update techniques become invaluable. We close with some final remarks:

- Typically, an additional factor of N must be included in the metropolis algorithm to produce uncorrelated samples to compute observables (see next section). Therefore, the computational cost of a VMC simulation goes as $O(N^4)$ if all determinants are computed from scratch, and $O(N^3)$ with the fast update.
- If the initial projected wavefunction $|\Psi\rangle$ is a superposition of wavefunctions, then the above W matrix procedure cannot be applied, and one typically must compute all the determinants from scratch.

2.4 Typical VMC simulation, practical considerations

In this section, we will outline the basic structure of a VMC simulation, and the main computations involved.

0. Initialize the following prerequisite objects:

[8] In practice, this is feasible for systems with up to about 100 sites.

- Eigenvector matrix U that defines the ansatz, $\Psi(\{\alpha\})$. Typically this is obtained by diagonalizing a tight-binding auxiliary Hamiltonian.

- An initial starting basis state $|x_0\rangle = |\uparrow\downarrow\downarrow\uparrow\uparrow\ldots\rangle$, and a vector that keeps track of ordering of the fermion operators in $|x_0\rangle$. [9]

- Tables of nearest neighbors (and further if necessary) for every site.

- The matrices $W^{\uparrow}, W^{\downarrow}$ corresponding to the configuration $|x_0\rangle$.

1. Create two loops, one nested inside the other. After each iteration of outer loop, observables of the spin model will be computed.

2. The inner loop typically is of $O(N)$ steps (for creating uncorrelated samples). At each iteration, propose a new configuration $|x'\rangle$ (typically connected to $|x\rangle$ by a spin flip). Compute $p(x',x) = \left|\frac{\langle x'|\Psi\rangle}{\langle x|\Psi\rangle}\right|^2$ and compare this ratio to a random number $r \in [0,1]$.

   - If $p(x',x) > r$, the proposed spin flip must be accepted. Change $|x\rangle \to |x'\rangle$ and update the W matrix according to (2.26).

   - If $p(x',x) \leq r$, don't accept the move.

3. At the end of the inner loop, compute observables of interest, and write them to an output file.

The above outlines the main steps of a VMC run. Error analysis of the local observables is performed at the end of the simulation. As an example, Figure 2.2 shows a typical Monte Carlo run on the triangular lattice, displaying the energy per site and error bars as a function of the number of Monte Carlo steps N_{MC}. As shown in the inset, the error decreases as $1/\sqrt{N_{MC}}$.

[9] Typically, it is verified that the overlap $\langle x_0|\Psi\rangle$ exceeds a specified minimum value.

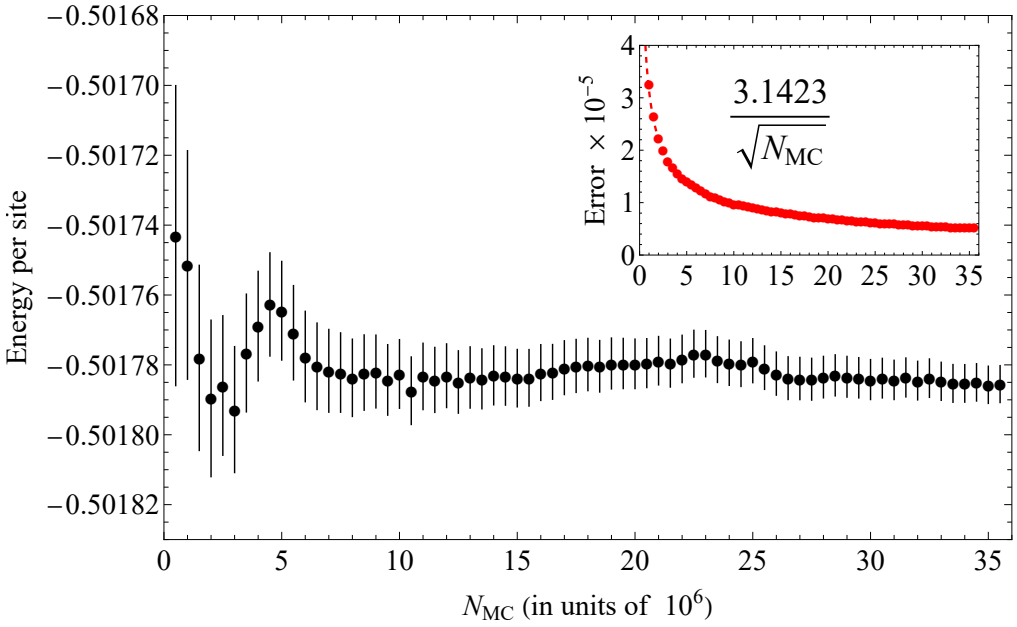

Figure 2.2: Energy per site for the 6×6 triangular lattice Dirac spin liquid (defined in chapter 5) as a function of the number of Monte Carlo steps N_{MC}. In the inset, we show the trend of the standard deviation (with the same x axis), clearly displaying a $1\sqrt{N_{MC}}$ behaviour. The dashed red line denotes the best fit curve to the data, given by $3.1423/\sqrt{N_{MC}}$.

Some additional remarks are listed below:

- The Gutzwiller projector is enforced by only sampling those $|x\rangle$ with one spin on every site. The spin flips proposed on the Markov chain clearly do not take us out of this sector.
- Connected to the above, if one wants to study states in a different spin sector (e.g. the $S = 1$ triplet monopoles constructed in Chapter 5), one must begin with the spin imbalance already present in $|x\rangle_0$.
- It's beneficial to compute the $W^{\uparrow}, W^{\downarrow}$ from scratch every once in a while to prevent compilation of numerical errors in the fast update.
- VMC simulations are "embarrassingly parallelizable". To compute observables, multiple Markov chains can be run in parallel on different computers, each with a different random number seed, without the need for communication between them.

2.5 Optimizing parameters

So far we have discussed how, given an initial ansatz $|\Psi\rangle = |\Psi(\{\alpha\})\rangle$, one can run a Monte Carlo simulation sampling the probability distribution $|\langle x|\Psi\rangle|^2$ and compute expectation values of observables of interest (e.g. variational energy).

Now, we briefly outline how one can use the *same* Monte Carlo routine to optimize the parameters of the wavefunction $\{\alpha\}$ to construct better approximants to the ground state of a system. The objects of interest are the 'forces' in parameter space

$$f_k = -\frac{\partial E}{\partial \alpha_k} = -\frac{\partial}{\partial \alpha_k}\frac{\langle \Psi | H | \Psi \rangle}{\langle \Psi | \Psi \rangle} \tag{2.28}$$

Estimating the set of forces $\{f\}$ tells us the direction in which the parameters should be modified to move towards an energy minimum. It turns out that these forces can be evaluated via a Monte Carlo sampling. This involves computing the derivatives

$$O_k(x) = \frac{\partial \ln \langle x|\Psi\rangle}{\partial \alpha_k} = \frac{1}{\langle x|\Psi\rangle}\frac{\partial \langle x|\Psi\rangle}{\partial \alpha_k} \tag{2.29}$$

The derivative $O_k(x)$ can be computed exactly with the knowledge of the mean field spectrum and eigenvectors [80]. Then, the forces are sampled according to the following equation

$$f_k \approx -2\mathrm{Re}\left[\frac{1}{N}\sum_{i=1}^{N} e_l^*(x_i)\left(O_k(x_i) - \bar{O}_k\right)\right] \tag{2.30}$$

where $e_l^*(x)$ is the complex conjugate of the local energy defined in (8.4), and $\bar{O}_k$ is the average

$$\bar{O}_k = \frac{1}{N}\sum_{i=1}^{N} O_k(x_i) \tag{2.31}$$

Once the forces are computed, we use the standard steepest descent approach. We modify

$$\begin{aligned} \alpha_k^{'} &= \alpha_k + \delta\alpha_k \\ \delta\alpha_k &= \tau f_k \end{aligned} \tag{2.32}$$

and recalculate the forces, repeating the process until the variational energy converges. In the last equation, the proportionality factor τ can be kept constant or modified over the course of the optimization. We note that more complicated optimization schemes also exist, like the stochastic reconfiguration approach [81, 82], which is particularly useful when there are many parameters and the energy landscape is relatively flat in this parameter space.

2.6 What observables can be computed?

In the table below, we briefly outline some quantities that can (and cannot) be accessed by VMC simulations, particularly concerning spin systems.

Can be computed	Cannot be computed
Spin-spin correlations: $\langle \vec{S}_i \cdot \vec{S}_j \rangle$ and other local observables.	Thermodynamic quantities e.g. Specific heat, susceptibility, etc.
Variational energy: $\langle \Psi \vert H \vert \Psi \rangle / \langle \Psi \vert \Psi \rangle$ of ground state and low lying excitations.	
Projected wave function overlaps $\langle \Psi_1 \vert \Psi_2 \rangle$: enabling calculations of Fidelity susceptibility [94], topological degeneracy [95] and modular matrices [96].	Properties of excited states in middle of spectrum.
	Other limitations
Real time quantum dynamics [97–99]	
Static and dynamical structure factors [100–102].	Biased towards the nature of trial wavefunctions.
SWAP operators: enabling calculations of Renyi and topological entanglement entropy [103, 104].	

CHAPTER 3

TENSOR NETWORKS

In this chapter, we will give a brief introduction to the central ideas of Tensor Networks (TN) in one and two dimensions. Tensor networks are a powerful mathematical framework used to efficiently represent certain classes of many-body quantum states and study their properties. Tensor network states serve as variational ansatzes, similar to Variational Monte Carlo, for approximating the ground states and excitations of spin models. While TN methods have become invaluable tools in condensed matter physics, they have also found deep applications in diverse fields like deep learning [105], lattice gauge theories [106] and quantum gravity [107]. One of the most compelling features of tensor networks is their ability to explicitly and intuitively capture the entanglement structure of quantum states. Although they are limited by the amount of entanglement they can capture, this limitation does not prevent us from studying the states we are most interested in: the ground states and low-energy excitations of local Hamiltonians.

One-dimensional tensor networks, known as Matrix Product States (MPS), are closely related to the Density Matrix Renormalization Group (DMRG) technique [108, 109] which has become the gold standard for studying 1D quantum systems due to its efficiency and wide applicability.

Projected Entangled Pair States (PEPS) extend the MPS formalism to two dimensions and beyond [110, 111]. Although computing observables is much more challenging than in one dimension, PEPS have nevertheless been very successful in studying 2D quantum systems. The PEPS framework has also been extended to study fermionic systems [112–114]; these fermionic PEPS are the subject of the next chapter. Finally, we note that tensor networks are particularly valuable for studying topologically non-trivial states due to their ability to encode topological order by imposing gauge symmetries [115].

In this chapter, we will discuss some main ideas of MPS and PEPS, and how they are used to study lattice models. The discussion here is heavily inspired by the sources [116–118], and

we direct the reader to these for additional details. We note that we will not be discussing other kinds of TNs, such as the Multiscale Entanglement Renormalization Ansatz (MERA) [112, 119], which have been particularly useful in studying critical states.

3.1 Diagrammatic Notation

The central feature of tensor networks is representing many-body quantum states and operators using diagrams. This visual representation makes many operations on the state transparent and is analogous to the success of Feynman diagrams in studying interaction processes in quantum field theory due to their simplicity and clarity.

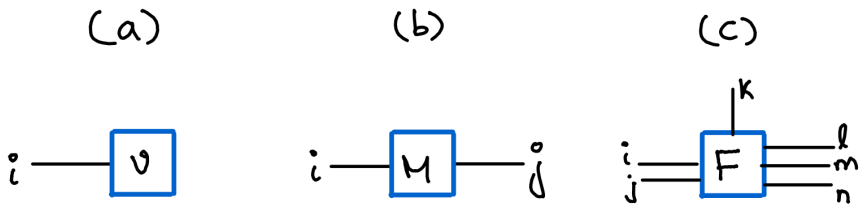

Figure 3.1: Pictorial representation of (a) a vector $\vec{v}$, (b) a matrix M, and (c) a tensor F_{ijklmn}.

In tensor networks, quantum states (and operators) are represented using tensor diagrams. The number of legs (lines attached to the tensor) indicates the number of free indices. Some examples are shown in figure 3.1. [1] For instance, in 3.1(c), specifying the values of $i \dots n$ would yield a complex number, and to completely determine F, one must specify F_{ijklmn} for all possible values of the indices.

When two tensors are combined, the legs that connect them are summed over. In this manner, complex mathematical operations involving many tensors can be easily visualized using TN diagrams (figure 3.2).

An important factor to consider when contracting tensors is the computational cost i.e. number of operations needed. Multiplication of two $D \times D$ matrices requires $O(D^3)$ operations. More generally, the cost of contracting two tensors is given by $O(D^q)$ where q is the total number of legs attached to both tensors. Let's consider the second diagram in 3.2 and assume all indices take D values. It is easy to see that different sequence of contractions give different cost. This is illustrated in figure 3.3; one contraction has a cost of $O(D^5)$ but the other has $O(D^6)$. When contracting tensor networks, it is important to choose the most optimal scheme for contraction.

[1] We do not distinguish between upper and lower indices, or the location of the legs in the tensor. Note that different indices of the same tensor can have different 'dimensions' i.e. different number of possible values.

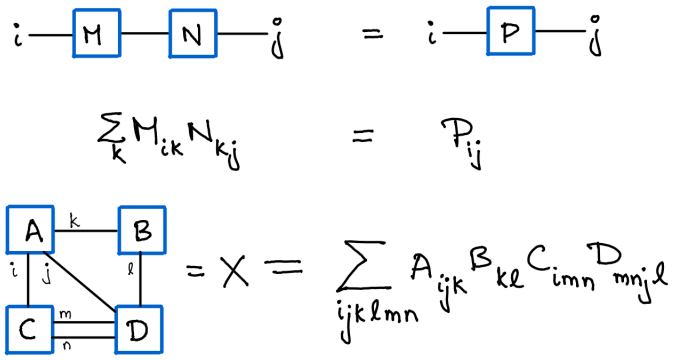

Figure 3.2: Examples of tensor contraction

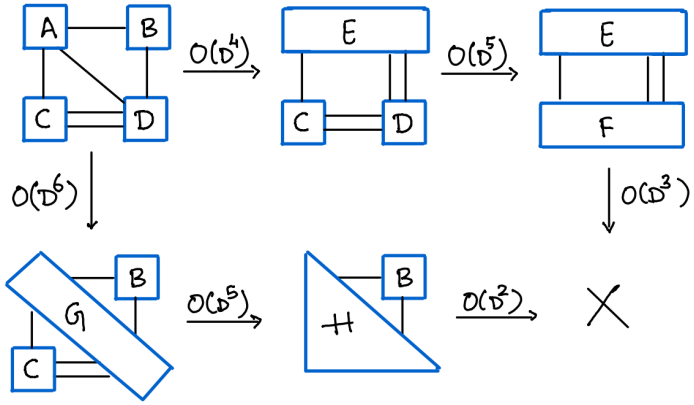

Figure 3.3: Different tensor contractions take different number of operations

3.2 Matrix Product States (MPS) and Projected Entangled Pair States (PEPS)

Consider a lattice system of N sites, where each site has a local Hilbert space of dimension p, $\mathscr{H} = \mathbb{C}^p$ with states $|0\rangle, |1\rangle, \ldots |p-1\rangle$. Then, a generic quantum state in the many body Hilbert space of N partices can be written as

$$|\Psi\rangle = \sum C_{i_1,i_2,\ldots i_N} |i_1\rangle \otimes |i_2\rangle \otimes \ldots \otimes |i_N\rangle \tag{3.1}$$

Thus, the number of parameters (coefficients C) required to specify the state is p^N, exponential in the number of sites. For large systems, one cannot even store all these coefficients in a classical computer. Additionally, the nature of entanglement in the state $|\Psi\rangle$ is not at all apparent from the coefficients.

Tensor network states approximate have a different structure (see figures 3.4 and 3.5 for examples in one and two dimensions). Here, each site of the lattice is associated with a tensor, and these tensors are interconnected by 'virtual' degrees of freedom. The total number of parameters

needed to describe the state scales linearly with the number of sites, specifically $O(NpD^2)$ for Matrix Product States (MPS) and $O(NpD^4)$ for Projected Entangled Pair States (PEPS) on a square lattice [2]. The additional parameter D is a constant known as the bond dimension, and it characterizes the tensor network (p is usually called the physical dimension, and D the virtual dimension). If $D = 1$, the tensor network state is simply a product of disconnected pieces for each site, and thus represents a product state. Thus, the entanglement in the many body wavefunction is 'carried' by the virtual bonds. The larger the bond dimension, the larger is the entanglement that can be captured by the tensor network state.

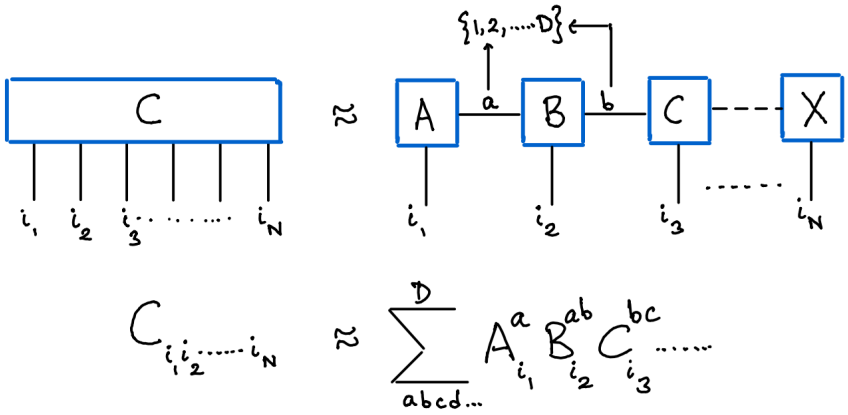

Figure 3.4: Expressing the many body wavefunction as an MPS.

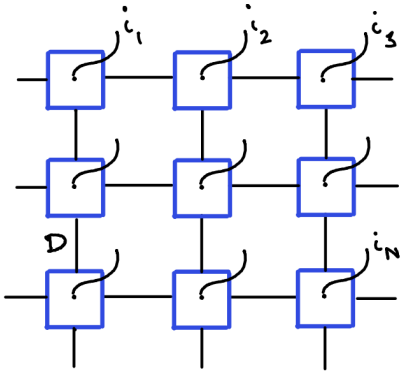

Figure 3.5: A general PEPS ansatz. The curved lines represent the physical indices coming out of the plane.

At first glance, this approximation of exponentially reducing the number of parameters seems very severe, and should not be valid/good enough to represent general many-body states $|\Psi\rangle$ [3]. The catch however, is that the ground states of local Hamiltonians are *very* different from generic quantum states in the many body Hilbert space. The former satisfy the so-called area law of

[2] If we consider a tensor network state with translational invariance, then the number of parameters does not scale at all with the size of the system.

[3] Unless D itself is exponential in N.

entanglement, which states that the entanglement entropy of the reduced density matrix of a region R of the lattice scales as the boundary of the region; $S(R) \sim \partial R$ [4]. General states would instead behave according to a Volume law $S(R) \sim R$, the entanglement of a region would scale as the volume of the region. This area law has been rigorously proven for 1D gapped systems [121] (where it is a constant asymtotically), and is believed to hold for higher dimensions as well. [5]. In fact, not only the ground state, but states obtained through the unitary evolution of local Hamiltonians over polynomial time acting on the ground state also obey the area law. In this sense, the physics essential to the real world of quantum many body systems takes place in an exponentially small corner of the Hilbert space [123]. Fortunately, it turns out that it is precisely this corner of the Hilbert space that MPS and PEPS target and can represent efficiently. We will soon see how this is the case.

We note in passing that highly non-trivial states can be captured in the MPS formalism already using low values of D. For example, the Majumdar-Ghosh ground state discussed in the previous chapter can be written as an exact MPS with $D = 3$. This is illustrated for periodic boundary conditions in the figure 3.6. The matrices $A^{\uparrow}$ and $A^{\downarrow}$ are the same at every site, and are given by

$$A^{\uparrow} = \begin{pmatrix} 0 & 1 & 0 \\ 0 & 0 & -1 \\ 0 & 0 & 0 \end{pmatrix}, \quad A^{\downarrow} = \begin{pmatrix} 0 & 0 & 0 \\ 1 & 0 & 0 \\ 0 & 1 & 0 \end{pmatrix} \tag{3.2}$$

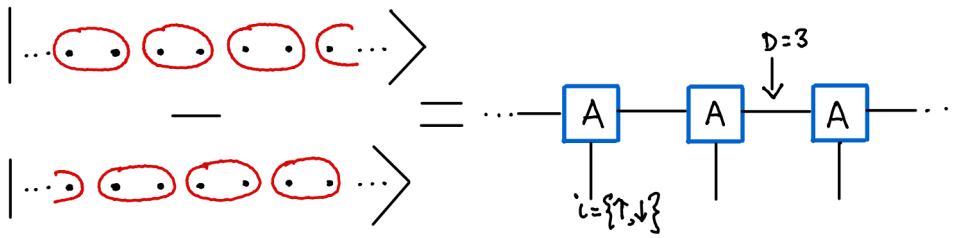

Figure 3.6: Casting ground state of Majumdar-Ghosh model in MPS form. The singlet pairs are denoted by the red circles.

In addition, the toric code ground state can be exactly written as a 2D PEPS with $D = 2$ [124], and the RVB spin liquid state can be exactly represented with $D = 3$ [125].

[4] The area law was first discussed in the context of entropy of black holes [120]

[5] We note that for critical systems there is a subleading logarithmic contribution, and for 2D systems with topological order, there is an additional negative universal constant known as the topological entanglement entropy. [122]

3.3 Singular Value Decomposition (SVD)

One of the central tools used in tensor networks is the SVD, which is a decomposition of *any* complex matrix of dimensions $m \times n$ as follows

$$M = USV^\dagger \tag{3.3}$$

where U and V are unitary matrices of dimensions $m \times m$ and $n \times n$ respectively, and S is a $m \times n$ diagonal matrix with non-negative, that can be chosen to be arranged in descending order.

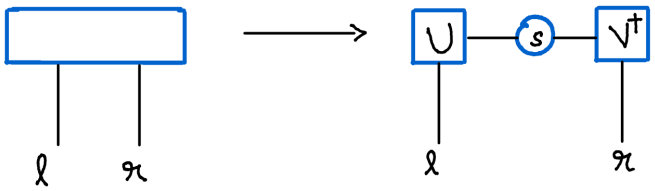

Figure 3.7: Singular Value Decomposition of a tensor

As an example, let's consider a state $|\Psi\rangle = \sum_{pq} \Psi_{pq} |p\rangle |q\rangle$ represented by a tensor with two legs of different dimensions l and r (figure 3.7). Writing out the matrix equation, we have (assuming $l > r$)

$$\Psi_{pq} = \sum_{\alpha=1}^{l} \sum_{\beta=1}^{r} U_{p\alpha} S_{\alpha\beta} V^*_{q\beta} = \sum_{\alpha=1}^{l} \sum_{\beta=1}^{r} U_{p\alpha} s_{\beta\beta} \delta_{\alpha\beta} V^*_{q\beta} = \sum_{\beta=1}^{r} U_{p\beta} s_{\beta\beta} V^*_{q\beta} \tag{3.4}$$

Therefore, the state $|\Psi\rangle$ can be recast as

$$|\Psi\rangle = \sum_{p=1}^{l} \sum_{q=1}^{r} \sum_{\beta=1}^{r} U_{p\beta} s_{\beta\beta} V^*_{q\beta} |p\rangle |q\rangle = \sum_{\beta=1}^{r} s_{\beta\beta} \left(\sum_{p=1}^{l} U_{p\beta} |p\rangle \right) \left(\sum_{q=1}^{r} V^*_{q\beta} |q\rangle \right) \equiv \sum_{\beta=1}^{r} s_{\beta\beta} |u_\beta\rangle |v_\beta\rangle \tag{3.5}$$

Thus, we have rewritten the wavefunction into a single summation that runs up to the smaller index. This is known as Schmidt decomposition of $|\Psi\rangle$, and the number of terms in the summation is known as the Schmidt rank [126]. Note that due to the unitarity of U and V, we must have $\langle u_k | u_{k'} \rangle = \delta_{kk'} = \langle v_k | v_{k'} \rangle$.

It is straightforward to see that the Schmidt values $s_{\beta\beta}$ determine the entanglement in the system. Let us compute the reduced density matrix ρ_l

$$\rho_l = \mathrm{Tr}_r \left(|\Psi\rangle \langle\Psi| \right) = \sum_k \langle v_k | \left(s_{\beta\beta} s_{\beta'\beta'} |u_\beta\rangle |v_\beta\rangle \langle u_{\beta'}| \langle v_{\beta'}| \right) |v_k\rangle = \sum_k s_{kk} |u_k\rangle \langle u_k| \tag{3.6}$$

Thus the von Neumann entanglement entropy of the subregion l is simply

$$S_l = \sum_k^r \lambda_k \log \lambda_k, \qquad \lambda_k = s_{kk}^2 \tag{3.7}$$

For a normalized state $\langle\Psi|\Psi\rangle = 1$, the Schmidt values must satisfy $\sum_k \lambda_k = 1$. Thus, we can clearly see that the greater the number of terms in the Schmidt decomposition, the larger the entanglement in the state. For a maximally entangled state of dimension r, all the terms are finite, $\lambda_k = 1/r \ \forall k$, and S_l attains its maximum bound of $\log r$.

Any generic many-body wavefunction can be exactly reshaped into a tensor network form, through a sequence of SVDs. For example, in the 1D case, we start from the ends of the chain, gradually increasing the bond dimension, reaching up to $D^{N/2}$ in the middle of the chain. However, such a large bond dimension is impossible to deal with numerically. In practice, a cutoff is applied to limit the maximum bond dimension (thereby constraining the entanglement in the system), and a subsequent scaling analysis is performed with increasing bond dimension. Likewise, if one has an estimate of the amount of entanglement in the system S, then the number of states to be included in the Schmidt decomposition would be roughly $\exp S$.

We would like to mention that aside from the entanglement entropy (which is just a number), the set of all eigenvalues of the reduced density matrix can be thought of as the spectrum of an "entanglement Hamiltonian". It has been shown that the entanglement spectrum contains much richer information about the system [127, 128]. We will discuss entanglement spectra in more detail in the next chapter.

3.4 Area law of Entanglement

From the above discussion, it directly follows that tensor networks satisfy the area law. Consider a region A of an MPS with L sites, whose reduced density matrix we wish to compute. We can perform an SVD at the bond intersecting the remainder of the system. Since the dimension of this virtual bond is D, the maximum number of terms in the Schmidt decomposition is D. Thus, the entanglement of a region with L sites is bounded by $\log D$, a constant independent of the system size. Consequently, MPS satisfy the area law. This principle extends to higher dimensional tensor networks as well, and an illustration for $2D$ PEPS is given in figure 3.8. Each bond intersected by the boundary contributes a maximum of $\log D$ to the entanglement entropy. By reshaping the tensors, we observe that the bond dimension of the virtual bond connecting the two regions grows as D^L. Therefore, the entanglement entropy is bounded by its logarithm:

$$S(A) \leq L \log D \implies S(A) \sim L \tag{3.8}$$

Thus we see that the bond dimension is a crucial quantity that controls how much entanglement the state possesses, and determines the size of the accessible portion of the Hilbert space (see figure 3.9).

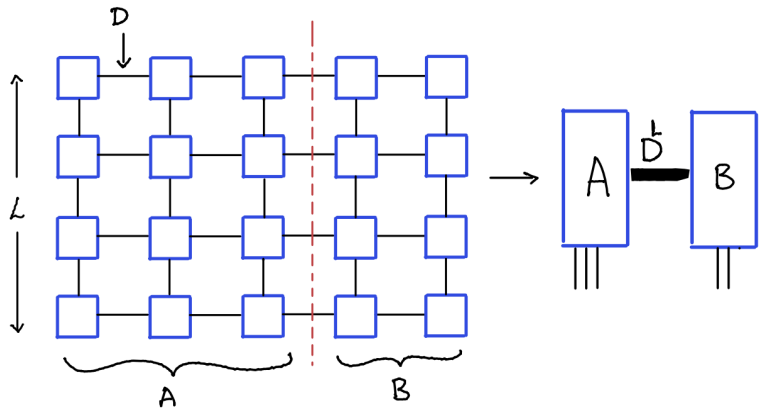

Figure 3.8: Area law of entanglement for two dimensional tensor networks. All virtual legs on the left have bond dimension D. The physical legs for the tensors are not shown but assumed to be present.

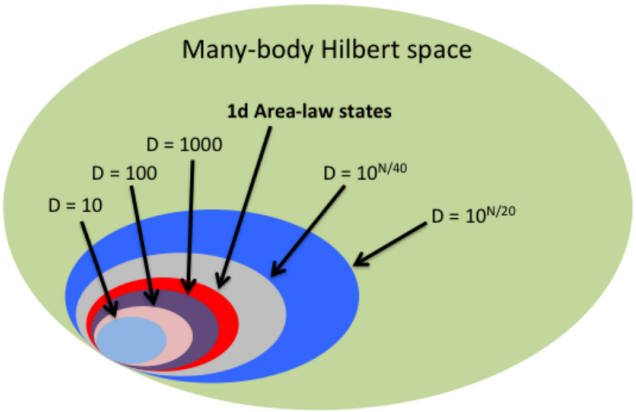

Figure 3.9: Illustration of many-body Hilbert space. As D is increased, more and more states are accesible. If D is allowed to grow exponentially, states beyond the area law can also be described. Figure taken from Ref [117].

3.5 Computing Observables

To compute the expectation value of a local operator $\langle\Psi|\hat{O}|\Psi\rangle$ (e.g., an operator acting on a single site like magnetization), we sandwich the operator between the state and its conjugate, and then contract the network from the left and right boundary vectors toward the operator site.

In the 1D case, such computations can be performed efficiently i.e. with a polynomial scaling in the number of sites. As an example, we show the computation of the norm of an MPS, $\langle\Psi|\Psi\rangle$ in figure 3.10. Each contraction step in the bulk has the same cost of $O(pD^3)$. Therefore, the total computational cost would grow linearly with the number of sites.

What about observables for PEPS? Here we come across a cruicial difference between tensor networks in one and higher dimensions. The computation of the expectation value of a local

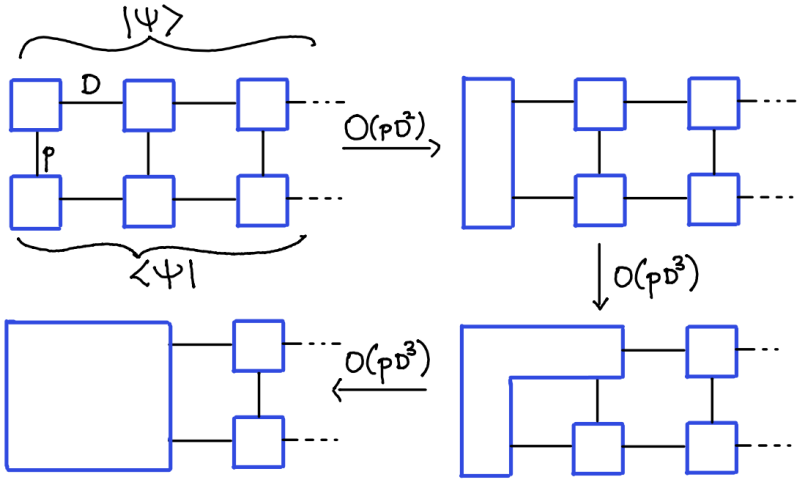

Figure 3.10: Norm of the state $|\Psi\rangle$ computed in MPS form by sequential contraction of tensors.

observable $\hat{O}$ for a 2D PEPS is shown in figure 3.11. We note that the bond dimension of the tensors grow as the contraction proceeds and eventually becomes exponential in system size. This exponential growth is unavoidable, making exact contraction impossible except for very small systems. Therefore, even though we can represent a PEPS ansatz with a polynomial number of parameters, computing observables cannot be done exactly. Therefore, we must rely on approximate methods, the development of which remains an active field of research. Some techniques proposed to address this challenge are MPS-MPO based approaches [129–131], the Tensor Renormalization Group (TRG) [132, 133], Tensor Network Renormalization [134], Loop optimization [135], and the Corner Transfer Matrix Renormalization Group (CTMRG) [136, 137]. In this thesis we use the latter technique, which will briefly be outlined in the next section.

We note that there is a gauge freedom in how we define the MPS/PEPS ansatz. This is illustrated in figure 3.12. We can introduce an identity XX^{-1} rewrite the whole TN in terms of $B = X^{-1}AX$. Therefore, infinitely many tensor networks describe the same physical state. This gauge freedom can be exploited in 1 dimension to compute observables extremely efficiently and elegantly. One chooses a gauge known as the canonical form, where the MPS tensors are orthonormalized in the sense that the tensors to the left and to the right of a specific site satisfy certain orthogonality conditions. This is directly related to the Schmidt decomposition previously discussed: for a leg joining two tensors, performing a Schmidt decomposition of the wavefunction across this leg results in a set of wavefunctions for the left and right subsystems. In the canonical gauge, each value of the virtual index corresponds to the Schmidt vectors on the left and right of the cut. In other words, in the canonical form the sum over the virtual index is exactly the last expression in (3.5).

This canonical form does not exist in general for 2D tensor networks. [6]

[6]However, we note that a subclass of PEPS known as isometric tensor networks have been recently proposed

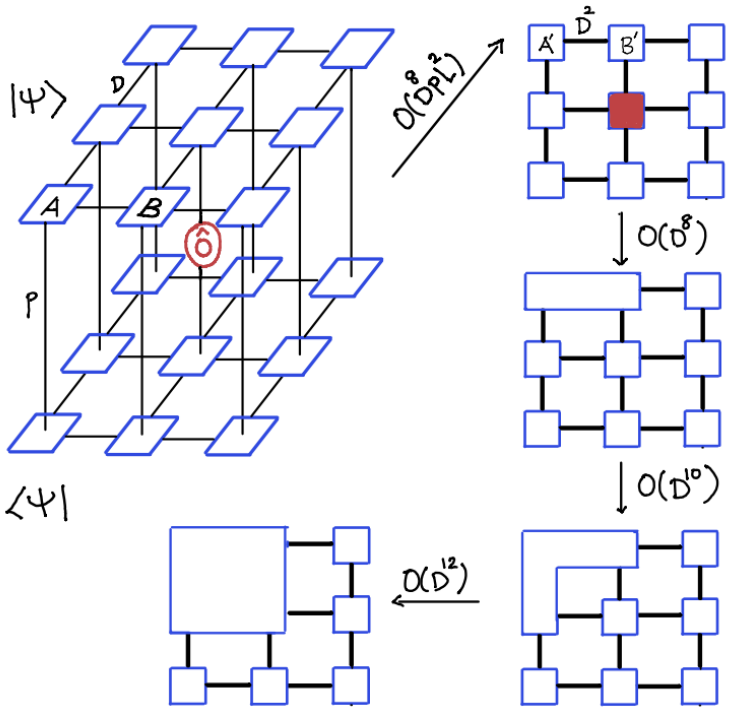

Figure 3.11: Expectation value of a single site operator $\langle\Psi|\hat{O}|\Psi\rangle$ computed by sequential contraction of tensors. In the first step we perform a contraction of all the physical indices, resulting in one layer of square tensors with bond dimension D^2. One tensor is shaded in red to indicate that the contraction with the observable has taken place.

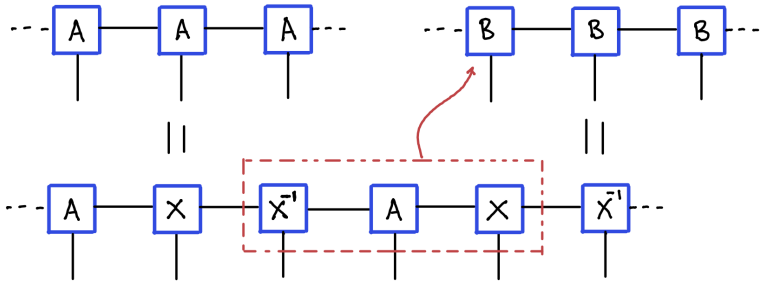

Figure 3.12: Gauge freedom of tensor networks. Both A and B describe exactly the same wavefunction.

3.6 Corner Transfer Matrix Renormalization Group (CTMRG)

The CTMRG method is an efficient technique used to approximate the contraction of two-dimensional infinite tensor networks (e.g. infinite PEPS or "iPEPS") [139, 140]. The Corner transfer matrix was first introduced to compute the partition function for 2D classical models by Baxter [141, 142].

Suppose we wish to compute an expectation value of a local observable $\hat{O}$ on a site. We first

which do permit a canonical form [138].

define the tensors C_i, T_i, $i = 1 \ldots 4$ that describe the environment around the site of interest (see figure 3.13). As these environment tensors cannot be contracted exactly due to the exponential cost, we introduce a parameter known as the environment bond dimension χ, which dictates the maximum rank of the environment tensors. Its clear that χ controls the entanglement of the central site with the environment. Taking the limit $\chi \to \infty$ would yield the exact result. The

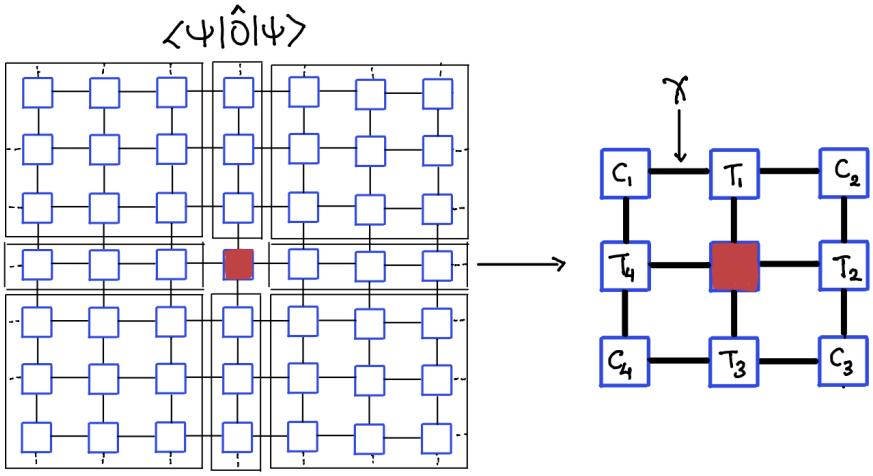

Figure 3.13: Defining the environment tensors C and T for contracting an infinite 2D tensor network. The contraction is approximated by the environment bond dimension χ.

CTMRG method involves iteratively refining the environment tensors $\{C, T\}$ by letting the system grow in all directions and renormalizing them. In figure 3.14 we describe a 'left move', where the system is enlarged by duplicating a column of C and T tensors to the left of the site of interest. Then, these are absorbed into the existing tensors which increases the bond dimension. Lastly, we perform an SVD and truncate the bond dimension to χ. Identical moves along all four directions are performed, and this procedure is repeated many times, until convergence is reached; typically one checks that the spectra of the environment tensors no longer change appreciably. Finally, a systematic scaling analysis of the observables is performed as a function of both χ and D.

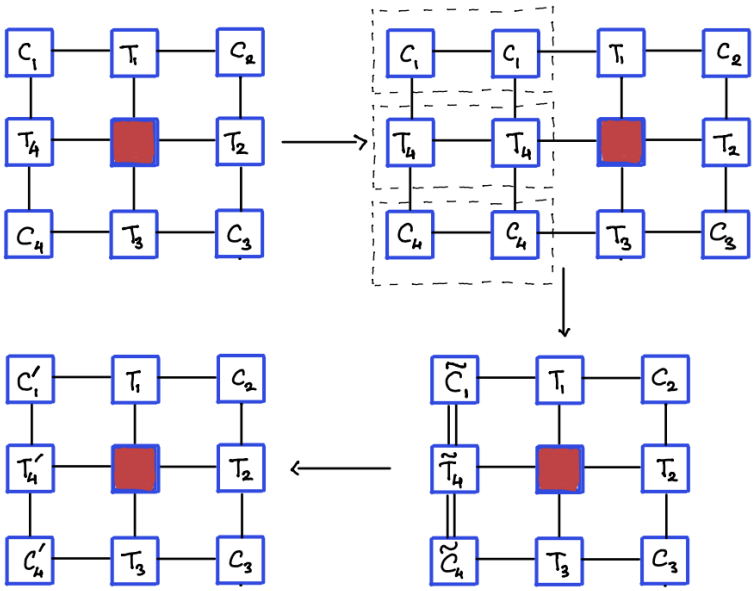

Figure 3.14: Performing a 'left move' to renormalize the C and T tensors to the left of the central site. First an additional column is inserted, followed by an absorption of the column to the left, and finally a renormalization where the environment bond dimensions are reduced back to their original value χ.

CHAPTER 4

FERMIONIC PEPS FOR CHIRAL SPIN LIQUIDS

4.1 Motivation

In this chapter (which is based on our work [143]), we will discuss the properties of fermionic PEPS wavefunctions describing Chiral Spin Liquids (CSLs). As mentioned in chapter 1, CSLs are exotic states of matter characterized by the absence of magnetic ordering while breaking time-reversal (T) and parity (P) symmetries [144]. They can also exhibit topological order [145]. They have been encountered in several quantum spin models with SU(2) [146–153] or higher SU(N) [154–161] symmetry in the presence of a chiral term breaking explicitly T and P. In some cases, P and T can be broken spontaneously, as demonstrated in both Hubbard/Heisenberg-like models [162–169] and Kitaev models [170] on lattices with odd plaquettes [171–178]. Parent Hamiltonians have also been devised for CSLs [179–181].

As CSLs typically emerge in strongly correlated systems, numerical tools for determining phase diagrams of generic Hamiltonians and characterizing CSLs are desired. Tensor networks like Projected Entangled Pair States (PEPS) [110] are well suited to the investigation of spin liquids. Topological orders can be encoded naturally by imposing virtual gauge symmetries [115, 182]. In addition, chiral forms of PEPS can describe CSL [183, 184] and be used as an efficient variational scheme to attack frustrated quantum spin models hosting CSL phases [185, 186]. On the other hand, infinite PEPS (iPEPS) is an ideal tool as it defines states in the thermodynamic limit directly, avoiding finite size extrapolations.

Despite the above mentioned successes and strengths of the PEPS framework, it has remained challenging to figure out completely whether conventional bosonic PEPS can truly describe CSL. In particular, it is still unclear whether topological obstruction (to be discussed in section 4.3) affects the global topological properties like the topological GS degeneracy or the correct conformal field theory (CFT) counting in the entanglement spectrum (ES). For the non-chiral case, PEPS

is believed to be a conceptually good ansatz. In contrast, whether chiral PEPS give the correct topological degeneracy of CSLs is still unsettled in general due to expensive computation cost [183], except in very rare cases where bond dimension is very small [187].

In our work, based on the recently proposed projected fermionic PEPS (fPEPS) ansatz, we show using VMC techniques, that PEPS can represent CSLs with correct topological degeneracy. Further, using this fPEPS ansatz as an initial state, we perform variational optimization to attack a frustrated $J_1 - J_2 - J_\chi$ square lattice model [188] in the regime of chiral spin liquid [185, 189, 190]. The fPEPS approach has competitive energy compared to the conventional bosonic PEPS, and crucially shows correct entanglement spectrum degeneracy.

This chapter is organized as follows. As CSLs can be constructed by Gutzwiller projecting copies of Chern insulators, an introduction to the latter topic is presented in section 4.2. Then, in section 4.3, we discuss the challenges in representing chiral states using tensor networks. In 4.4, we discuss the numerical techniques employed in our work, including the construction of the parton ansatz and the VMC and PEPS methods. Then, in section 4.5 we show results of the VMC analysis of fPEPS states on finite clusters, and in section 4.6 we discuss the variational optimization of the fPEPS states on the infinite plane to study the $J_1 - J_2 - J_\chi$ model. Finally, we conclude with a summary of our findings in section 4.7.

4.2 Chern Insulators

4.2.1 Berry connection and Chern number

The study of Chern insulators has its origins in the Integer Quantum Hall effect (IQHE), a phenomenon observed in two-dimensional electron systems subjected to strong magnetic fields. Discovered in 1980 by Klitzing, Korda, and Pepper [191], the IQHE manifests as a quantized Hall conductance that is remarkably robust against disorder and impurities. This quantization was soon linked to the topological properties of the system [192]. Indeed, the Hall conductance is quantized in integer multiples of e^2/h, and the proportionality factor is obtained as the sum of the 'Chern numbers' of all the bands that lie below the Fermi level. The Chern number (defined below) is a topological invariant which characterizes the global properties of the electronic wavefunctions in the bulk of the material. Thus the IQHE was the first physical phenomena that linked topological invariants to observable physical quantities.

Chern insulators extend the concepts of the IQHE to systems without an external magnetic field, and were first theoretically proposed in the pioneering work by Haldane in 1988 [193]. Haldane's model consists of a honeycomb lattice with complex next-nearest-neighbor hopping terms that break time-reversal symmetry. Thus, in some region of the phase diagram, the Bloch bands have a non-zero Chern number and thus a quantized Hall conductance. This model provided a conceptual framework for understanding how topological phases could arise in systems where the total magnetic flux through the unit cell is zero.

Let us now understand these states better, and we start by defining the ideas of Berry connection, Berry curvature and Chern number. Consider a translationally invariant system whose k space hamiltonian is the $q \times q$ matrix $\hat{H}(\mathbf{k})$. Denote its eigenvectors as $|\psi^{(n)}(\mathbf{k})\rangle$, $n = 1,\ldots,q$. Then, the Berry connection for the n^{th} band is the following vector field

$$\mathbf{A}(\mathbf{k}) = i \langle \psi^{(n)}(\mathbf{k}) | \nabla_{\mathbf{k}} | \psi^{(n)}(\mathbf{k}) \rangle \tag{4.1}$$

The line integral of the Berry connection over a closed path in the Brillouin zone yields the Pancharatnam-Berry phase [194, 195], which is the geometrical contribution to the phase acquired by the eigenstates along the path. It has found ubiquitous application in many areas in condensed matter physics [196]. The curl of the Berry connection is known as the Berry curvature $F(\mathbf{k})$

$$\mathbf{F}(\mathbf{k}) = \nabla_{\mathbf{k}} \times \mathbf{A}(\mathbf{k}) \tag{4.2}$$

The Berry connection is gauge dependent, but the Berry curvature is not. For a two dimensional Brillouin zone, the latter has just one component given by

$$F(\mathbf{k}) = \partial_{k_x} A_y(\mathbf{k}) - \partial_{k_y} A_x(\mathbf{k}) \tag{4.3}$$

The Chern number is a topological invariant, which measures the 'flux' of the Berry curvature through the whole Brillouin zone

$$C = \frac{1}{2\pi} \int_{\text{BZ}} \mathbf{F}(\mathbf{k})\, d^2k \tag{4.4}$$

The Chern number is necessarily an integer, due to the periodicity of $\mathbf{k}$ space and the single valuedness of the vector potential $A(\mathbf{k})$. This principle underpins the robustness of the Hall conductance: small perturbations to the Hamiltonian that do not close the bulk gap cannot alter the Chern number. For the system to change this topological invariant, it must undergo a quantum phase transition. A crucial aspect of Chern insulators, as with other topological phases, is the bulk-boundary correspondence [197]. This principle states that the non-trivial topology of the bulk bands, characterized by a non-zero Chern number, guarantees the existence of robust gapless edge states at the boundaries of the material. These edge states are chiral, meaning they propagate in a single direction along the edge of the sample. Importantly, these states are protected against backscattering from impurities or disorder, which leads to dissipationless edge transport. We note that time reversal symmetry breaking (though either complex phases or external magnetic field) is essential for having Chern bands.

Chern insulators have been experimentally observed in several systems, including magnetically doped thin-films, and moiré graphene [198]. Additionally, these exotic states have also been simulated using cold atom platforms where artificial gauge fields can be engineered with high precision [199, 200]. We also note in passing that partially filled Chern bands in the presence of interactions exhibit the Fractional Quantum Hall Effect, and these states are known as

Fractional Chern Insulators (FCI) [201, 202]. Finally, over the last two decades, a new phase of matter known as Topological Insulators (TI) has emerged. Unlike Chern insulators which require time reversal symmetry breaking, these materials preserve time-reversal symmetry while maintaining a bulk energy gap and supporting gapless edge modes. The unique properties of topological insulators are made possible by the presence of spin-orbit coupling [203].

We next discuss in detail the properties of the square lattice Hofstadter model, an example of a Chern insulator. Before describing the model, we will first explain how magnetic fields are incorporated into lattice models.

4.2.2 Peierls Substitution

Peierls substitution is a method used to incorporate the effects of a magnetic field into lattice tight-binding models [204]. The main idea is to modify the hopping amplitudes of the model by introducing complex phases that account for the influence of the vector potential $\mathbf{A}$ associated with the magnetic field $\mathbf{B} = \nabla \times \mathbf{A}$. These phases are equivalent to those in the Aharonov-Bohm effect [205], which describes how the presence of a magnetic field affects the phase of a particle's wavefunction.

Consider a free fermion hopping model on a lattice with real hoppings t_{ij}

$$H = \sum_{i,j} t_{ij} c_i^\dagger c_j + \text{h.c.} \tag{4.5}$$

where $c_i^\dagger$ and c_j are fermionic creation and annihilation operators at sites i and j, respectively. The Peirels substitution involves making the transformation

$$t_{ij} \to t_{ij} \exp\left(i \frac{e}{\hbar} \int_{\mathbf{r}_i}^{\mathbf{r}_j} \mathbf{A} \cdot d\mathbf{l} \right) \tag{4.6}$$

where the line integral is in between the sites i and j in some specified path. The phase factor $\exp\left(i \frac{e}{\hbar} \int_{\mathbf{r}_i}^{\mathbf{r}_j} \mathbf{A} \cdot d\mathbf{l} \right)$ represents the accumulated phase due to the magnetic field as an electron hops between lattice sites. This substitution can be justified as follows: if the vector potential is slowly varying (across the length scale of the lattice spacing), then one can show that the continuum limit of the above approximation yields the minimal coupling Hamiltonian $H \sim (\mathbf{p} + e\mathbf{A})^2$ [206]. From Stokes' theorem, the line integral of the vector potential $\mathbf{A}$ around a closed loop γ on the lattice is equal to the magnetic flux Φ piercing the enclosed area $\text{Ar}(\gamma)$. Therefore, the phase accumulated as a fermion traverses a loop is

$$\exp\left(i \frac{e}{\hbar} \oint_\gamma \mathbf{A} \cdot d\mathbf{l} \right) = \exp\left(i \frac{e}{\hbar} \int_{\text{Ar}(\gamma)} \mathbf{B} \cdot d\mathbf{S} \right) \equiv \exp\left(i \frac{2\pi\Phi}{\Phi_0} \right) \tag{4.7}$$

where Φ_0 is the flux quantum h/e. This approach effectively incorporates the influence of the magnetic field into the lattice model. We will use this method throughout this thesis; the monopole

excitations constructed in the next chapter also involve tight binding models with non-trivial fluxes through the plaquettes of the lattice. Finally, we note that due to the presence of complex hoppings, the Hamiltonian breaks time reversal symmetry.

4.2.3 Hofstadter model

The Hofstadter model is a tight binding model of electrons hopping on a square lattice under the influence of an uniform magnetic field [207]. Consider an $L \times L$ square lattice with sites (m,n) and define the creation (annihilation) operators $c^\dagger_{m,n}$ ($c_{m,n}$) for a fermion on each site. Then, the hamiltonian in real space can be written as [1]

$$H = -J \sum_{m,n}^{L} \left(c^\dagger_{m,n} c_{m+1,n} + e^{i2\pi\alpha m} c^\dagger_{m,n} c_{m,n+1} + \text{h.c.} \right) \tag{4.8}$$

Here, $\alpha = p/q$ is a rational number that characterizes the flux through every plaquette which is $2\pi\alpha$ (p,q are chosen to be coprime) [2]. With the choice of gauge chosen, the system is invariant under translations along y by unit lattice spacing, but along x only by q lattice spacings. Thus, the enlarged magnetic unit cell is of size $q \times 1$, leading to q energy bands in k space. Due to the breaking of time reversal symmetry, the bands in the Hofstadter problem are topological and have non-zero chern number. The energy spectrum of this model as a function of α features a starkling fractal pattern, arising due to the two competing length scales in the problem (the lattice spacing and the magnetic length), known as the Hofstadter butterfly, shown in figure 4.1.

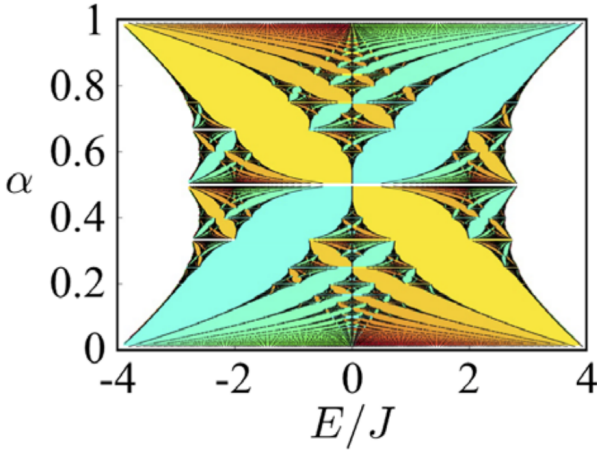

Figure 4.1: Energy spectrum of hamiltonian (4.8) as a function of α. The colors in the band gaps represent the sum of Chern numbers of all the bands below the gap. Warm (cold) indicate positive (negative) Chern number. Figure taken from [208].

[1] We choose a specific gauge for the vector potential, known as the Landau gauge. Observables like the fluxes though plaquettes and the energy spectrum are independent of the gauge choice.

[2] We assume periodic boundary conditions, implying that for uniform flux through every plaquette, q must divide L.

The momentum space hamiltonian can be easily obtained by fourier transforming (4.8). Upto a unitary transformation, it is given by the following $q \times q$ matrix [3]

$$\tilde{H}(k_x, k_y) = \begin{bmatrix} -2\cos\left(k_y - 2\pi p/q\right) & 0 & \dots & -e^{-iqk_x} \\ 0 & -2\cos\left(k_y - 4\pi p/q\right) & \dots & 0 \\ \vdots & \vdots & \dots & \vdots \\ -e^{iqk_x} & 0 & \dots & -2\cos\left(k_y\right) \end{bmatrix} \tag{4.9}$$

Note that the hamiltonian in k space has the periodicity $\tilde{H}(k_x + 2\pi/q, k_y) = \tilde{H}(k_x, k_y)$. As an example, we discuss the energy spectrum for the case $\alpha = 1/5$, plotted in figure 4.2(a). All the bands have non-zero Chern numbers, given by $C = 1, 1, -4, 1, 1$, in increasing order of energy. The Chern numbers of the bands were computed using the Fukui-Hatsugai-Suzuki algorithm [209], which is outlined in appendix B. We note that the total Chern number of all the bands of the system is zero, since completely filling all the bands would yield a trivial insulator. As mentioned earlier, a non-zero Chern number in the bulk implies the presence of topologically protected edge modes if the system has boundaries. To check this, we diagonalize the same Hamiltonian on a cylinder, with periodic boundary conditions along the y direction and finite extent along x. The result is shown in figure 4.2(b). We can clearly observe dispersive modes that connect the previously separated bands. These additional modes are localized on the boundaries of the cylinder. They are robust to perturbations that do not close the gap between the bulk bands, and can conduct electricity without dissipation. If the Fermi energy is in between two bulk bands, the number of edge modes (on one edge) is given by the sum of Chern numbers of all occupied bands (i.e., all bands below the Fermi level). This is clearly evident from figure 4.2b. [4]

4.3 Representing chiral states using Tensor Networks: Topological Obstruction

Tensor Networks have been remarkably successful in representing quantum many-body states and probing the physics of spin systems. However, as mentioned before, representing chiral spin liquids has remained non-trivial and challenging. In fact, Dubail and Read demonstrated that free-fermion PEPS cannot exactly represent gapped chiral states [210] (see also [211]). They proved a no-go theorem stating that the parent hamiltonians for chiral free-fermion PEPS must be gapless (if short ranged), implying an infinite correlation length. Although this was rigorously shown only for the free-fermion case, numerical studies suggest that this holds true even for PEPS describing chiral states with interactions [183, 185, 186, 211, 212]. This difficulty is linked to the fact that, in a non-interacting system with translational symmetry, Wannier functions (Fourier transforms of the Bloch wavefunctions [213, 214]) cannot be exponentially localized if

[3] We assume $J = 1$ for the rest of this section.

[4] Note the change in chirality of the edge modes after crossing the $C = -4$ band.

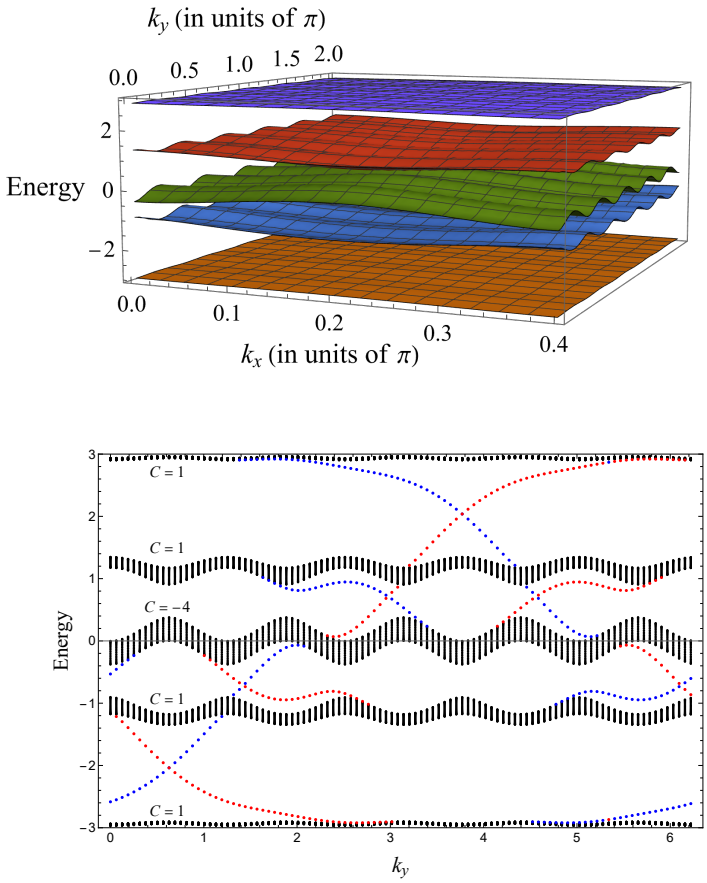

Figure 4.2: (a) Energy bands of the Hofstadter hamiltonian (4.8) with $\alpha = 1/5$ on a torus. The bands are well separated, and have Chern numbers $C = 1, 1, -4, 1, 1$. (b) The same model diagonalized on a cylinder, with periodic boundary conditions along the y direction, and finite extent along x (we choose $L_x = 100$). The band structure features edge modes which are localized either on the left (red) or the right (blue) edge of the cylinder.

the bands are topologically non-trivial i.e. have non-zero Chern number [215]. It is well known that for topologically non-trivial bands, the Bloch wavefunctions cannot be analytic across the entire Brillouin zone (the phase of the wavefunction cannot be chosen continuously). Brouder et al. [215] showed that this fact disallows the construction of exponentially localized Wannier functions.

These findings have sparked considerable debate and skepticism about studying chiral spin liquids (CSLs) using Tensor Networks. However, there is still hope. Subsequent research has shown that although the no-go theorem cannot be violated, it does not pose a practical barrier to *approximately* representing CSLs using PEPS. For instance, while the spin-spin correlations are indeed long-ranged, they exhibit two distinct regions: an initial short-range exponential decay, followed by a long-range "Gossamer" tail, which results in the infinite correlation length. As an example, in figure 4.3, we show the spin-spin correlations obtained from a bosonic PEPS optimization for a spin model (defined later in (4.18)) in a parameter region that hosts a chiral

spin liquid [212]. The two regions mentioned above are clearly visible. The region with the exponential decay steadily increases with increasing bond dimension, and the correlations at $r \to \infty$ (equivalent to the square of the magnetization) approach 0 as χ increases, indicating stabilization of the CSL phase. Additionally, the magnitude of the long-range tail is very small, showing that it contributes minimally to the overall spin-spin correlations.

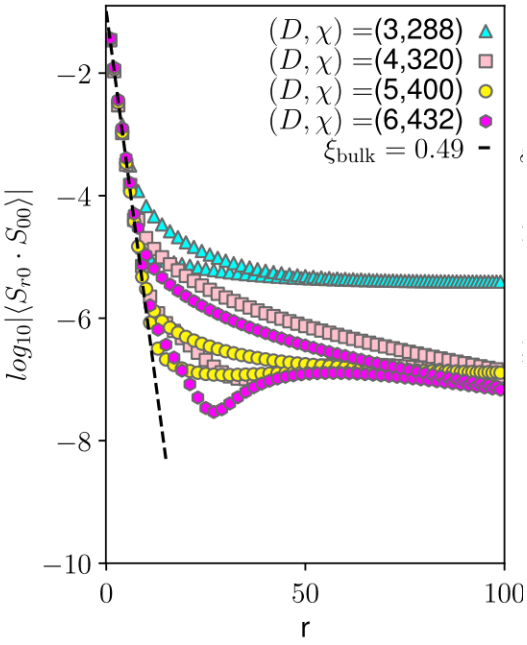

Figure 4.3: Spin-spin correlations as a function of distance for different values of bond dimension D and environment bond dimension χ. Figure taken from [212]. Each (D,χ) has two curves, corresponding to odd and even sites, due to the oscillation in the sign of the correlations.

Moreover, the optimized variational energies (when studying spin models hosting CSL phases) are highly competitive with other numerical approaches, which is an encouraging sign [185, 212, 216]. Finally, the entanglement spectrum (defined later in section 4.6.2) of these PEPS states matches exactly with the predictions of conformal field theory, suggesting that PEPS can accurately capture the entanglement properties of these states. The only caveat being that in bosonic chiral PEPS there's an unphysical doubling of the chiral edge branch in the odd topological sector [183, 184] which seems to persist in the case of fully optimized wave functions for Abelian SU(N)$_1$ and non-Abelian CSLs [154, 185, 186, 216–218]. This feature is not present in fermionic PEPS, as we will see in section 4.6.

In light of these findings, the emerging consensus is that while the no-go theorem manifests as long-range tails in the correlation functions, some global topological properties of CSLs can indeed be captured by PEPS. Our work provides further supporting evidence, by demonstrating that the topological degeneracy of a CSL on a torus is accurately represented by fermionic PEPS ansatzes at *finite* bond dimensions. In the next section, we discuss the specifics of the CSL we

consider, the fermionic PEPS approximation and the numerical methods used for analyzing the properties of the fPEPS states. This is followed by a presentation of our results.

4.4 Numerical techniques

4.4.1 Parton ansatze

In order to construct a simple CSL, we first consider a Chern insulator state with $C = 1$, obtained by diagonalizing the following (free electron) Hofstadter hamiltonian on the square lattice

$$H = \sum_{\langle ij\rangle,\sigma} t_1 \chi_{ij} c^\dagger_{i\sigma} c_{j\sigma} + \sum_{\langle\langle ik\rangle\rangle,\sigma} t_2 c^\dagger_{i\sigma} c_{k\sigma} e^{i\theta_{ik}} + \text{h.c.} \tag{4.10}$$

where $\langle ij\rangle$ ($\langle\langle ik\rangle\rangle$) denotes nearest (next-nearest) neighbor bonds and σ is the spin index, $\sigma = \{\uparrow, \downarrow\}$. The hoppings are identical for both spin species. We fix $t_2 = 0.5t_1$, $\chi_{ij} = \pm 1$ to ensure a π flux through every square plaquette and choose the complex phases θ_{ik} to obtain a $\pi/2$ flux in all triangles. We choose the gauge (used in Ref. [219]) such that the unit-cell contains two nearest neighbour sites along the x direction, see figure 4.4(a).

The exact many-body spin wavefunction $|\varphi\rangle$ is a Gutzwiller projected Slater-determinant

$$|\varphi\rangle = P_G \prod_\alpha c^\dagger_{\alpha,\uparrow} c^\dagger_{\alpha,\downarrow} |0\rangle, \tag{4.11}$$

where the Gutwiller-projector $\prod_i (n_{i,\uparrow} - n_{i,\downarrow})^2$ projects onto the subspace of exactly one electron per site, and $c^\dagger_{\alpha,\sigma}$ correspond to single-particle states obtained from the mean-field Hamiltonian Eq. (4.10). It is known that the resultant exact parton state is a $SU(2)_1$ CSL which is equivalent to the $\nu = 1/2$ bosonic Laughlin state. On a torus, this CSL has a two-fold topological degeneracy where the degenerate states can be constructed by imposing different boundary conditions on the parton wavefunctions [220]. On a cylinder, the CSL hosts chiral gapless edge states predicted by $SU(2)_1$ Wess-Zumino-Witten (WZW) CFT [221].

4.4.2 Construction of Gaussian fPEPS state

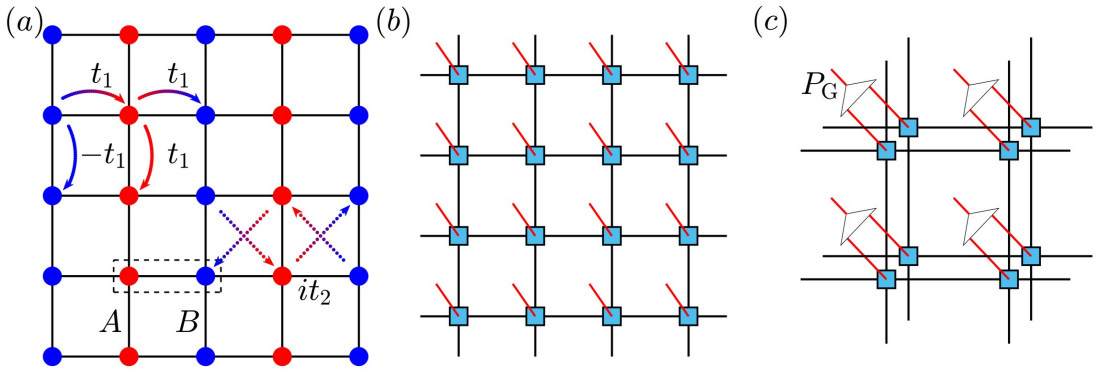

Figure 4.4: Schematic diagrams of (a) the Chern insulator model defined in (4.10) with a two-site A, B unit-cell along x direction marked by the dashed line, (b) the translation invariant GfPEPS ansatz with A, B physical sites included in one tensor and (c) the spin state (4.11) constructed from Gutzwiller projected GfPEPSs. Figure and caption taken from [219].

To construct the Gaussian fPEPS state which is an approximation of the exact ground state of Eq. (4.10), we adopt the method introduced in Refs. [222, 223]. The translation invariant many-body ansatz is parametrized by a single Gaussian tensor with four virtual indices and two physical indices corresponding to the unitcell in the Hofstadter model. In the Gaussian tensor, the virtual space dimension is defined by the number of virtual modes M. Each virtual fermion mode can be occupied or unoccupied, thus the bond dimension becomes $D = 2^M$ for a spinless state and $D = 4^M$ for spinful $SU(2)$ state. The single particle orbitals $\tilde{c}^\dagger_{\alpha,\sigma}$ are completely determined by the real space Gaussian tensor, and the CSL state is constructed as $P_G \prod_\alpha \tilde{c}^\dagger_{\alpha,\uparrow} \tilde{c}^\dagger_{\alpha,\downarrow} |0\rangle$. To obtain the best approximation of this tensor, we use gradient optimization and choose the (free electron) energy of Eq. (4.10) at half-filling as cost function. As the unprojected fPEPS state is gaussian, it can be also written as a Slater-determinant (product state) on any finite torus and all the physical properties can be extracted exactly. In Ref. [219] it has been shown that the gaussian fPEPS becomes chiral from $M \geq 2$, and the correlation functions improve quantitatively with increasing M. However, the general topological properties of the fPEPS remain unclear after Gutzwiller projection, and are not accessible (except for the entanglement spectrum) by conventional PEPS techniques. Therefore, we introduce the following Monte-Carlo method to probe the properties of Gutzwiller projected Gaussian fPEPS.

4.4.3 Monte-Carlo technique

The Gutzwiller projected fPEPS wavefunctions discussed previously are analysed within a standard Markov chain Monte Carlo framework [224], discussed in chapter 2. In particular, overlaps between two projected wavefunctions $|\psi\rangle$ and $|\phi\rangle$ can be computed straightforwardly as

follows,

$$\frac{\langle\psi|\phi\rangle}{\langle\psi|\psi\rangle} = \frac{\sum_x \langle\psi|x\rangle\langle x|\phi\rangle}{\langle\psi|\psi\rangle} = \frac{\sum_x |\langle\psi|x\rangle|^2 \frac{\langle x|\phi\rangle}{\langle x|\psi\rangle}}{\langle\psi|\psi\rangle} \tag{4.12}$$

where $\{|x\rangle\}$ is chosen to be the S_z basis to enforce the one fermion per site constraint exactly. In this paper, we remain in the $S_z = 0$ sector, with equal number of up and down spins. Then, by sampling the normalized probability distribution

$$P(x) = \frac{|\langle\psi|x\rangle|^2}{\langle\psi|\psi\rangle} \tag{4.13}$$

one can estimate the wavefunction overlap as

$$\frac{\langle\psi|\phi\rangle}{\langle\psi|\psi\rangle} \sim \frac{1}{n}\sum_{i=1}^{n} \frac{\langle x_i|\phi\rangle}{\langle x_i|\psi\rangle} \tag{4.14}$$

where n is the number of Monte Carlo runs, and $\{|x_i\rangle\}$ are the spin configurations sampled in the Markov chain. We note that the cost of computing overlaps for the projected fPEPS is *independent* of bond dimension, as the set of single-particle orbitals in real space can be obtained analytically for any M. This enables the calculations in section 4.5, where we quantitatively analyze the fPEPS for $M = 1 \ldots 6$.

4.4.4 Variational iPEPS method

In Section 4.6, we perform a variational study of a chiral Heisenberg antiferromagnetic model, taking the projected fPEPS parton ansatz as the initial state in our optimization. Firstly, we construct the Gutzwiller projected tensor for the parton ansatz following Refs. [219, 223], where a single tensor of bond dimension 4^M contains two physical sites and satisfies $\mathrm{U}(1) \times \mathrm{SU}(2)$ symmetry. Secondly, we choose this tensor as the initial state and variationally optimize the tensor elements with the $\mathrm{U}(1) \times \mathrm{SU}(2)$ virtual symmetry kept. To optimize the tensor, we adopt the automatic differentiation method [225] and choose the energy of the chiral spin model as the cost function. The energy is evaluated using the corner transfer matrix renormalization group (CTMRG) [226, 227] method, where the approximate contraction is controlled by the environment bond dimension χ, and becomes exact in the $\chi \to \infty$ limit.

4.5 Characterizations of projected fPEPS parton ansatz: VMC studies

Several VMC algorithms have been developed to study topological properties of spin liquids, including entanglement entropy, modular matrices, and topological degeneracy [220, 228, 229]. In this section, using VMC calculations on finite tori, we investigate the properties of the fPEPS wavefunctions, and compare them to the exact CSL state constructed from the parton ansatz

(4.11). We demonstrate that the fPEPS at finite bond dimension can capture the correct properties of the CSL. The gaussian fPEPS tensor is determined from optimizing the mean-field Hamitonian (4.10) on a 80×80 torus. Subsequently, we put the optimized tensor on smaller $L \times L$ clusters to construct the many-body wave functions which are input to the Monte Carlo algorithm.

4.5.1 Wavefunction fidelity

We first compute the normalized overlap between the projected exact CSL and the fPEPS states with periodic boundary conditions (PBC-PBC), given by

$$O_M = \frac{|\langle \Psi_{\text{exact}} | \Psi_M \rangle|}{\sqrt{\langle \Psi_{\text{exact}} | \Psi_{\text{exact}} \rangle \langle \Psi_M | \Psi_M \rangle}}. \tag{4.15}$$

By contracting physical indices of the PEPS, the overlap can be mapped to a partition function of a two-dimensional classical statistical model, thus decaying exponentially with system size. We can then define the fidelity per unit area (free energy) $f = (O_M)^{1/L^2}$, which should show weak size dependence and converge to a finite value in the $L \to \infty$ limit. The infidelity $1 - f$ plotted in figure 4.5 confirms these expectations. In addition, the diminishing infidelity with increasing M clearly demonstrates the improving accuracy of the optimized fPEPS states. We note that similar results have been obtained for the other three choices of boundary conditions, i.e., PBC-APBC, APBC-PBC and APBC-APBC.

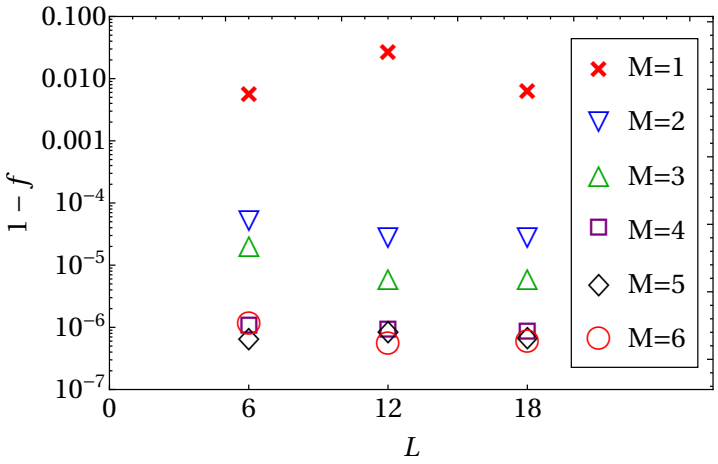

Figure 4.5: Infidelity $1 - f$ plotted in logarithmic scale as a function of the system size L for fPEPS states with $M = 1 \ldots 6$ and periodic boundary conditions. The estimated error bars are smaller than the size of the symbols.

4.5.2 Spin-spin correlations

To further confirm that the projected fPEPS describe the correct physical properties of the CSL, we compute the real space spin-spin correlations for the $L = 18$ system. These are shown in figure 4.6. We observe exponential behaviour at short distances as expected for a gapped state,

with a very short correlation length $\xi \approx 0.57$. Further, the fPEPS states (for all values of M) are essentially indistinguishable from the exact CSL in terms of the correlations. Note that the saturation of the decay of the long-distance correlations for $r > 5$ can be simply attributed to a finite size effect with periodic boundary conditions when $r \sim L/2$. Hence, we cannot definitively establish the presence of the Gossamer tail, discussed in the previous section.

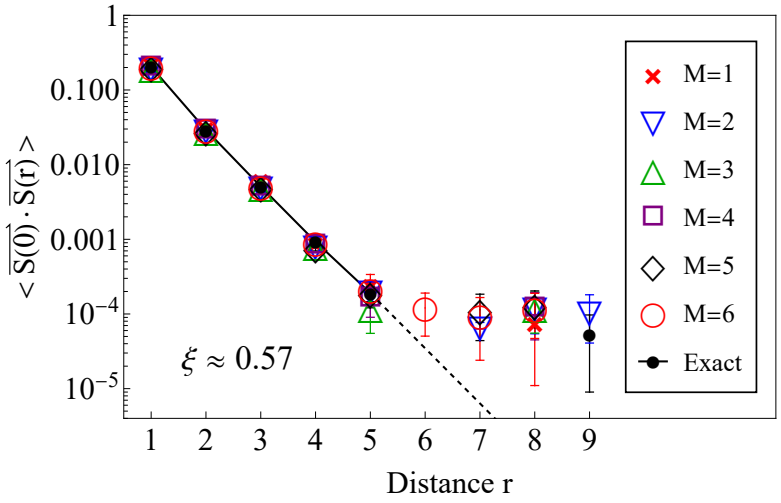

Figure 4.6: Logarithmic plot of the magnitude of spin-spin correlations as a function of distance for the exact and projected fPEPS, for the $L = 18$ cluster with periodic boundary conditions. Symbols are ommited if the obtained value is lesser than one standard deviation of error. The expected correlations of the exact CSL at $r > 5$ (in the thermodynamic limit) are shown as a dotted line, extending the exponential behavior.

4.5.3 Topological properties: ground state degeneracy

A fundamental characteristic of a topological ordered phase is a ground state degeneracy which depends on the topology of space [230]. As mentioned previously, the exact $SU(2)_1$ CSL state (4.11) has a two-fold degeneracy on a torus: imposing different boundary conditions on the parton ansatz before projection yields degenerate states that cannot be distinguished by local observables (like spin-spin correlations) after projection. In the thermodynamic limit, it is known that the four states only span a two dimensional linear space [220].

To investigate this property of the fPEPS and exact states on finite clusters, we compute the 4×4 overlap matrix O with elements

$$O_{\alpha,\beta} = \frac{\langle \Psi_M^\beta | \Psi_M^\alpha \rangle}{\sqrt{\langle \Psi_M^\alpha | \Psi_M^\alpha \rangle \langle \Psi_M^\beta | \Psi_M^\beta \rangle}} \tag{4.16}$$

where α and β denote the four choices of boundary conditions on the torus. The rank of this hermitian matrix (which denotes the number of linearly independent eigenvectors) is the number of non-zero eigenvalues. In the thermodynamic limit, the eigenvalues of the exact state must

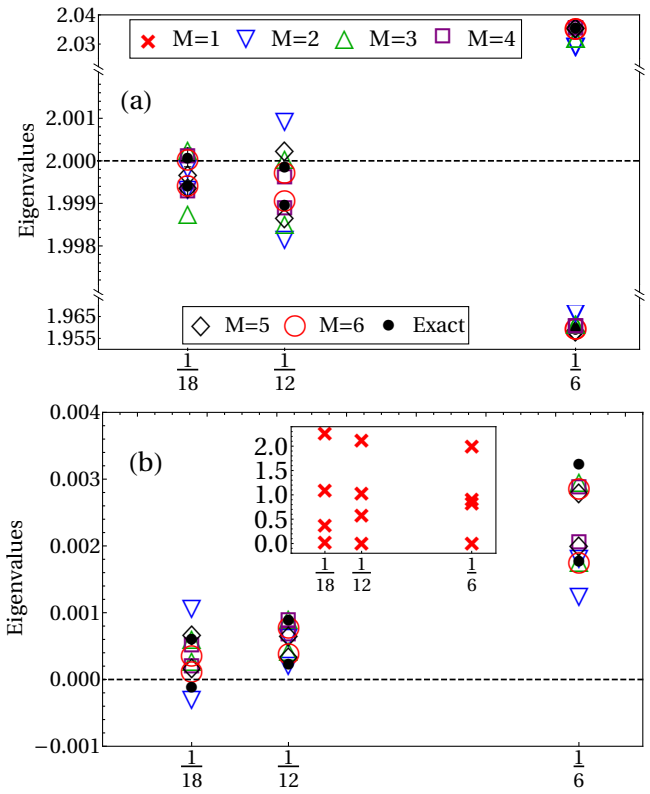

Figure 4.7: Eigenvalues of the overlap matrix as a function of inverse system size $1/L$ for the exact and the fPEPS states. Pairs of eigenvalues converge to +2 and 0 in (a) and (b) respectively. The $M = 1$ data is shown in the inset since it has a much larger deviation than the other fPEPS states. The estimated error bars are roughly the size of the symbols.

converge to $\{+2, +2, 0, 0\}$ (the trace of the matrix being 4). In figure 4.7, we plot the eigenvalues for both the projected fPEPS and the exact states as a function of L. Remarkably, we observe that for *fixed* $M > 1$, the eigenvalues converge to the exact result with increasing system size (already at $L = 18$, the deviation is at most 10^{-3}). In addition, from the analysis of the eigenvectors of the overlap matrix, we have obtained the following relations (up to a gauge degree of freedom)

$$
\begin{aligned}
|\Psi^{\text{PBC-PBC}}\rangle &= \frac{|\Psi^{\text{PBC-APBC}}\rangle + |\Psi^{\text{APBC-PBC}}\rangle}{\sqrt{2}}, \\
|\Psi^{\text{APBC-APBC}}\rangle &= \frac{|\Psi^{\text{PBC-APBC}}\rangle - |\Psi^{\text{APBC-PBC}}\rangle}{\sqrt{2}}
\end{aligned}
\tag{4.17}
$$

with a very good accuracy whenever $L \geq 18$, consistent with the fact that the states on the RHS and the LHS of the above equations belong to the same IRREPs of the C_4 rotation group on clusters with $L_x = L_y$ (respectively even and odd). These results substantiate that fPEPS, even at finite bond dimensions, can accurately capture the correct topological degeneracy of CSL states.

4.6 Simulation of the chiral $J_1 - J_2 - J_\chi$ model

From the VMC analysis in the previous section, we have seen that projected (Gaussian) fPEPS can describe topological properties of CSLs faithfully. However, for the purpose of studying frustrated spin models, the conventional parton ansatz has only a limited number of variational parameters such as hopping coefficients, Jastrow factors, etc. On the contrary, PEPS can represent generic interacting states with the systematic increase of bond dimension. Now we conduct a variational PEPS study on the chiral $J_1 - J_2 - J_\chi$ model using projected GfPEPS (discussed in the previous section) as the initial ansatz. The spin-1/2 hamiltonian is given by

$$\mathscr{H} = J_1 \sum_{\langle i,j\rangle} S_i \cdot S_j + J_2 \sum_{\langle\langle i,k\rangle\rangle} S_i \cdot S_k + J_\chi \sum_{\triangle_{ijk}} \left(S_i \times S_j\right) \cdot S_k. \tag{4.18}$$

This model was initially proposed in [188], where exact diagonalization techniques revealed that the ground state had a very high overlap with the exact Kalmeyer-Laughlin state. The model exhibits a chiral spin liquid (CSL) phase over a large region of its phase diagram, and we select a specific set of parameters also discussed in that work. The Hamiltonian can be undersdood as an effective Hamiltonian of the Fermi-Hubbard model through the Schrieffer–Wolff transformation. Realizing the Fermi-Hubbard model in cold atom experiments remains an active area of research [231–233]. Further, this model has been investigated in Ref. [185], where the sum of four triangular J_χ terms inside a plaquette has been equivalently written as a spin cyclic permutation $i(P_{ijkl} - P_{ijkl}^{-1})$ term. Ref. [185] performed a variational study of this model with bosonic iPEPS, and found a regime of $\mathrm{SU}(2)_1$ CSL in the phase diagram. The optimized bosonic iPEPS provides good variational energy and correct level counting in the entanglement spectrum predicted by $\mathrm{SU}(2)_1$ WZW CFT. However, there exists a redundant chiral branch in the odd (semion) sector [185, 234] which contradicts both the theoretical prediction and recent numerical results obtained from DMRG on finite cylinders [189, 190]. We emphasize that such artificial replication of chiral branches in bosonic iPEPS is quite general and is also found in the cases of SU(N) and non-Abelian CSLs [154, 186, 216, 218].

On the other hand, in Ref. [219] it was shown that the projected fPEPS from parton construction not only has correct level counting, but also has exact branch numbers in each topological sector of the entanglement spectrum. However, it is not clear whether such entanglement spectrum degeneracy of fPEPS is a robust or fine-tuned feature. From the variational study below we would like to show that (i) the parton state provides an energetically good initial guess for variational optimization and (ii) the optimized fPEPS state (which is beyond projected Gaussian states) still gives the correct entanglement spectrum counting and number of chiral modes, implying that our family of fPEPS states are not fine-tuned and provide a faithful description of CSLs.

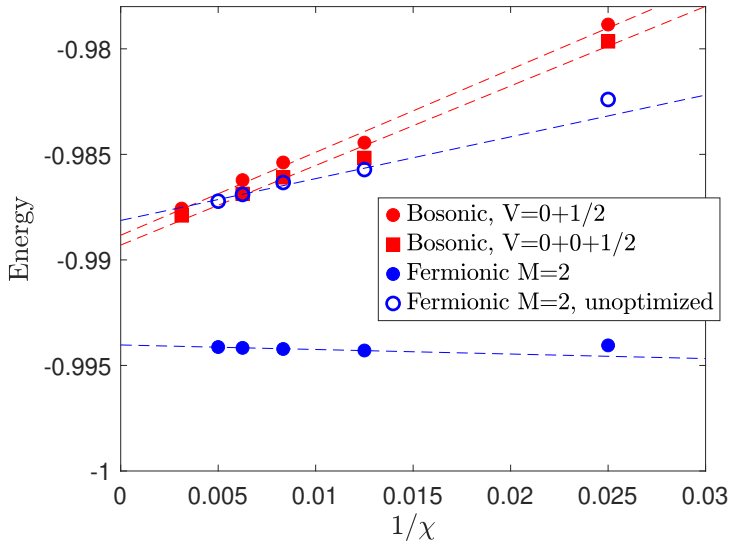

Figure 4.8: Variational energy of optimized bosonic iPEPS (red) and projected fermionic iPEPS (blue) for the spin model. Blue open circles show the energy of the fermionic parton ansatz at $t_1 = 1, t_2 = 0.5$ without variational optimization of tensor elements.

4.6.1 Variational energy

We choose the parameters of the spin model as $J_1 = 2\cos(0.06\pi)\cos(0.14\pi)$, $J_2 = 2\cos(0.06\pi)\sin(0.14\pi)$, $J_\chi = 4\sin(0.06\pi)$ which has been considered in Refs. [185, 188, 212] and is known to be deep inside the CSL phase with the ground state energy being $E \approx -1$. We import the SU(2) bosonic iPEPS method there and compute variational energies as a reference. For the bosonic iPEPS, the tensor has SU(2) symmetry and the unit-cell size is chosen to be one such that each tensor only has one physical leg. The results for virtual spaces $V = 0 \oplus 1/2$ ($D = 3$) and $V = 0 \oplus 0 \oplus 1/2$ ($D = 4$) are given in Fig. 4.8. As we extrapolate to the infinite χ limit the energies are around -0.99.

In our fPEPS treatment, the initial parton state is still chosen at the hopping parameter $t_1 = 2t_2$ which corresponds to the largest band gap. Since the smallest bond dimension $M = 1$ is non-chiral, we take $M = 2$ ($D = 16$) GfPEPS with Gutzwiller projection and compute the energy with respect to the spin model. Due to the gauge choice in the parton construction, the smallest unit-cell size is 2-sites along x direction. As can be seen in Fig. 4.8, the unoptimized parton state already has good energy close to the optimized bosonic iPEPS at $D = 3, 4$. After optimizing the fPEPS tensor elements, the energy further improves to $E \approx -0.995$. When comparing the energies of bosonic and fermionic iPEPS, one should recall that since our fPEPS has two-sites unitcell in y direction, the effective bond dimension in y direction is $D_{\text{eff}} = 4$ per site, while the x direction bond is much larger than that of bosonic iPEPS. This is consistent with the fact that our fermionic iPEPS has better energy.

4.6.2 Entanglement spectrum

The most common measure of entanglement in quantum many body systems is the von Neumann entropy, or more generally, the Renyi entropy [122]. Consider a system in a pure state $|\Psi\rangle$, and partition it into two subsystems A and B. The n^{th} Renyi entropy of the subsystem A is given by

$$S_A^{(n)} = \frac{1}{1-n} \ln \mathrm{Tr} \rho_A^n \tag{4.19}$$

where ρ_A is the reduced density matrix of the subsystem A

$$\rho_A = \mathrm{Tr}_B \left(|\Psi\rangle \langle \Psi| \right) \tag{4.20}$$

The von Neumann entropy $\mathrm{Tr}(\rho_A \ln \rho_A)$ is recovered from the Renyi entropy in the limit $n \to 1$. The 'Entanglement Spectrum' (ES) simply the set of eigenvalues of the reduced density matrix. It is now understood that the entanglement spectrum contains much richer information about the system. This was first realized by Li and Haldane [127] in the context of Fractional Quantum Hall (FQH) states, who observed that the $\nu = 5/2$ Moore-Read state and 'more realistic' Coulomb FQH wavefunction obtained from exact diagonalization had the *same* 'low energy' structure of the ES. Additionally, the counting and structure of these low-lying levels matched exactly with counting of states in the corresponding edge CFT. They hence conjectured that the low lying levels of the ES correspond to the physical edge excitations of the system, and can act as a "footprint" for topological order.

This connection was rigorously proven for non-interacting [235, 236] and more generic systems [237], and was soon identified in magnetic systems as well [238]. Additionally, the degeneracies of the ES levels provide insights into the topological order of the system. For instance, the Haldane chain exhibits a two-fold degenerate entanglement spectrum, with this degeneracy being protected by the system's symmetries [239]. Using the PEPS framework, it has been shown that the entanglement hamiltonian H_E (where $\rho_A = \exp(-H_E)$) only acts on the virtual degrees of freedom of the boundary of the region A [128]. This has been dubbed the 'PEPS bulk-boundary correspondence'.

The ES is now a standard quantity of interest when studying chiral spin liquids. For example, in Ref. [240], a CSL was proposed as the ground state of a Heisenberg model on the Kagome lattice with additional neighbor Ising interactions. Computations of entanglement spectra on a cylinder (figure 4.9) revealed low lying levels with a distinct counting of $1, 1, 2, 3, 5, 7, \ldots$. This sequence reflects the number of states at successive levels in the conformal towers of the $SU(2)_1$ Wess-Zumino-Witten (WZW) CFT, which is the same edge CFT as that of the Kalmeyer-Laughlin state.

Now we discuss our results of the ES. To analyse the level counting of entanglement spectrum, we put our optimized tensor on a finite width cylinder and compute the entanglement spectrum of such translation-invariant state. To compute entanglement spectrum, the boundary

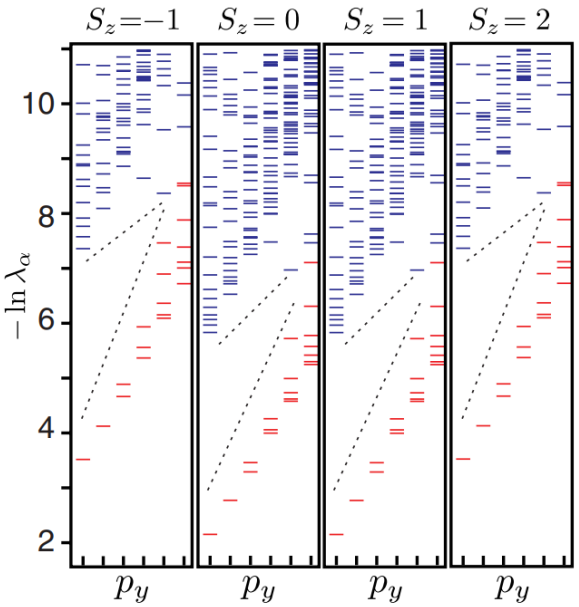

Figure 4.9: Entanglement spectrum from a DMRG simulation of a Kagome Heisenberg model (with additional Ising interactions). Due to $U(1)$ symmetry, the ES can be characterized by the S_z quantum number. Figure taken from [240].

Hamiltonian (transfer matrix fixed points) can be constructed exactly by exact contraction [128] or approximately by grouping CTMRG environment T tensors [184]. In the case of fermionic iPEPS, the tensor has U(1) × SU(2) virtual symmetry and the transfer matrix fixed points are labeled by virtual charge and parity of virtual spin, while in the case of bosonic iPEPS the tensor only has SU(2) virtual symmetry and the transfer matrix fixed points are labeled only by parity of virtual spin. Fig. 4.10 (a)-(b) show the entanglement spectrum of optimized $M = 2$ fermionic iPEPS computed from CTMRG with the environment bond dimension $\chi = 110$. The low energy spectrum shows SU(2) multiplets with counting $0, 1, 0+1, 0+1+1, ...$, in the integer spin sector and $1/2, 1/2, 1/2+3/2, ...$, in the half-integer spin sector, satisfying predictions from $SU(2)_1$ WZW CFT. Note that in both even and odd sectors there is only one low energy chiral branch, which matches with recent DMRG results on finite cylinders [189, 190]. On the contrary, Fig. 4.10 (c)-(d) show entanglement spectrum of $D = 3$ bosonic iPEPS. Here the level counting is correct, but an anomalous identical branch appears in the odd sector with a π-momentum shift. We also confirmed that the redundant branch can not be eliminated or shifted by increasing the bond dimension of the bosonic iPEPS.

4.7 Conclusion and outlook

Tensor Network methods have been widely applied to study frustrated spin models hosting possible spin liquid phases. However, due to a no-go theorem [210], doubts have arisen regarding

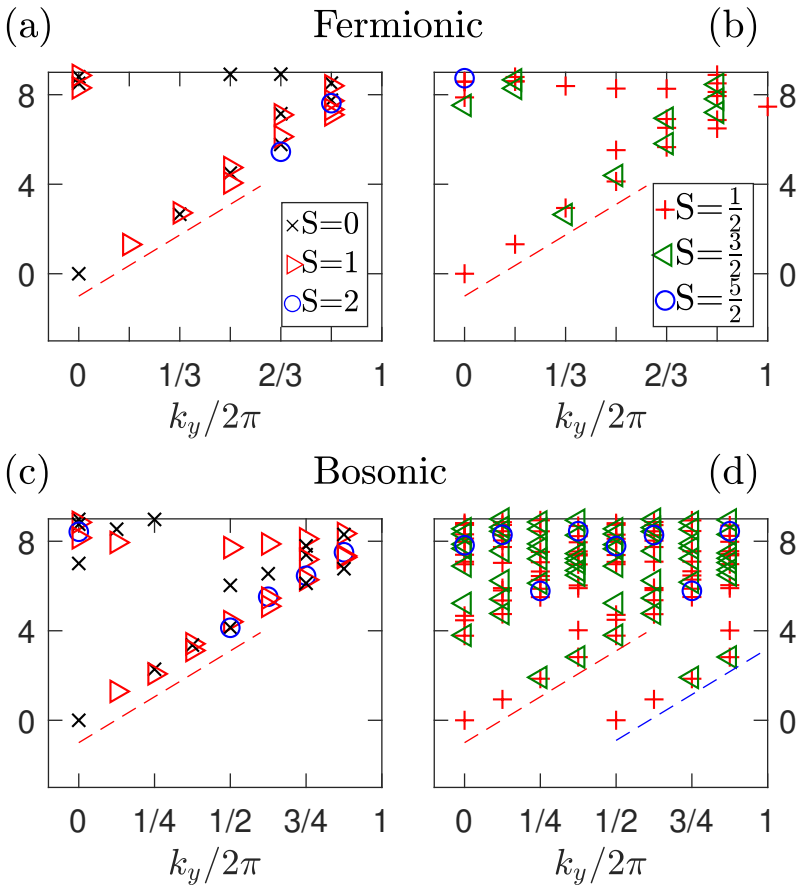

Figure 4.10: Entanglement spectrum of optimized $M = 2$ projected fermionic iPEPS (top) and $D = 3$ bosonic iPEPS (bottom) for the spin model on cylinders of finite width 6 and 8, respectively. Left and right columns correspond to even (integer spin) and odd (half-integer spin) sectors. The red dashed lines denote the theoretically predicted linear dispersions of the tower of states, while the blue dashed line denotes the redundant branch in the odd sector of bosonic iPEPS.

their ability to describe chiral states. In this chapter, we investigated the topological properties of projected fermionic PEPS ansatz for a CSL state. By performing a VMC analysis on the initial (Gutzwiller-projected) parton state, we demonstrated that fPEPS at finite bond dimension can accurately capture the topological ground state degeneracy of CSLs on a torus. This achievement has been challenging with conventional bosonic PEPS due to the high computational cost involved [183]. Additionally, our results show that the fPEPS ansatz effectively captures the spin-spin correlation functions of the CSL. Given the high quality of overlap fidelity, we anticipate that fPEPS will also accurately reproduce the modular S and T matrices.

Further, non-Gaussian fPEPS ansatze were optimised variationally for the $J_1 - J_2 - J_\chi$ Heisenberg model and were found to have competitive energy compared to their bosonic counterparts. Additionally, the optimized fermionic iPEPS retained the correct level counting of the entanglement spectrum as opposed to bosonic iPEPS which have a duplicate branch in the odd

topological (semion) sector. In future works, it would be interesting to see whether such artifact of bosonic iPEPS can be eliminated by further imposing virtual U(1) symmetry and/or increasing the unit-cell size like in the fPEPS case.

Our work provides further supporting evidence for using PEPS methods in describing chiral topologically ordered states, supplementing previous studies in this direction [185–187, 211, 217, 219]. As a future direction, our fPEPS ansatz can further be used to study the fermionic Hofstadter-Hubbard model [241] where both the Chern insulating phase and CSLs can be tuned by strength of Hubbard interaction (e.g. Ref. [59]). In that case, our Gaussian fPEPS ansatze with partially projected doublons are expected to be good initial variational ansatze at finite Hubbard interaction.

CHAPTER 5

MONOPOLES IN DIRAC SPIN LIQUIDS

In this chapter, we discuss the main results of this thesis involving the study of low energy excitations of Dirac Spin Liquids (DSLs) on the triangular and Kagome lattices. The DSL has been proposed to be a ground state candidate for both the nearest neighbor Kagome Heisenberg model [74, 242] and the $J_1 - J_2$ model on the triangular lattice with J_2 roughly in the region $0.06 \leq J_2 \leq 0.16$ [243, 244].

$$\begin{aligned} \mathcal{H}_{\text{Kagome}} &= J \sum_{\langle i,j \rangle} \mathbf{S}_i \cdot \mathbf{S}_j \\ \mathcal{H}_{\text{Triangular}} &= J_1 \sum_{\langle ij \rangle} \mathbf{S}_i \cdot \mathbf{S}_j + J_2 \sum_{\langle\langle ik \rangle\rangle} \mathbf{S}_i \cdot \mathbf{S}_k \end{aligned} \tag{5.1}$$

Both these models have been heavily studied over the past two decades, and there also exist alternate proposals for the nature of the ground state (and the region of the spin liquid phase for the triangular) [74, 242–258]. A complete consensus has not yet been reached. However, probing the low energy excitations of these systems can be extremely illuminating in understanding the physics of the ground state. As discussed in the first chapter, spin liquids can be gapped or gapless. Topological gapped spin liquids are understood to have well defined quasiparticles. For example, the toric code, a $\mathbb{Z}_2$ lattice gauge theory, is exactly solvable and has a gapped QSL ground state. Its low energy excitations are anyons which obey mutual fractional statistics.

In constrast, gapless spin liquids are less well understood, especially in two dimensions. No exactly solvable model exists, and the spinons are not deconfined. Specifically for Dirac spin liquids, the low energy theory is QED_3 whose physics involves spinons (massless Dirac fermions) coupled to a $U(1)$ gauge field. The low energy theory hosts monopoles and photons as gauge excitations. Understanding these excitations is crucial in addressing key issues about the DSL, such as its stability as a phase, and its experimental signatures. Monopoles correspond

to instanton events, that allow tunnelling between different vacua of the theory by inserting (multiples of) 2π flux of the $U(1)$ gauge field. On the lattice, they are constructed by inserting a unit 2π flux quantum and spreading the flux uniformly through all plaquettes. The scaling dimensions of the monopole operators, and their transformation under lattice symmetries are crucuial in understanding the stability of the DSL phase. If the monopole operator is relevant, monopole proliferation is allowed, which could destablize the spin liquid into an ordered phase. In the limit of large number of fermion flavors (N_f), monopoles have been proven to be irrelevant and the Dirac spin liquid is believed to be stable [259]. For realisitic systems with spin-1/2 magnetic moments, $N_f = 4$ and the monopoles are believed to be highly relevant in this regime. However, significant theoretical progress has been made in the last few years [260, 261] regarding the symmetries of monopoles on various two dimensional lattices at the mean field level (and in the large N_f limit). It has been shown that for bipartite lattices, there is always a trivial $SU(4)$ singlet monopole (which transforms trivially under all lattice symmetries) which condenses and destroys the DSL phase. However, for non-bipartite Kagome and triangular lattices, this trivial singlet monopole is disallowed for symmetry reasons, and the Dirac spin liquid can be indeed stable [260].

In this thesis, we study this problem numerically, using the VMC and exact diagonalization techniques. We explicitly construct variational wave functions corresponding to monopole excitations, and study their properties in the context of the models in (5.1). Crucially, we compute the monopole momenta and energetics after Gutzwiller projection, going beyond the mean field approximation. By doing so, we can also comment on the energetic stability of the DSL state to (one kind of) perturbation that breaks time reversal symmetry (leading to a chiral spin liquid). Additionally, we consider monopole excitations of a higher charge Q (corresponding to insertions of $2\pi Q$ flux), and compare the energetics with field theory predictions (for large N_f).

This chapter is organized as follows: in sections 5.1 and 5.2 we discuss the construction and properties of the Dirac spin liquid and its monopole excitations. In section 5.3, we discuss the momentum quantum numbers of the monopoles before and after projection. In section 5.4, we discuss the energetics of the monopole and localized excitations, and conclude in section 5.5.

5.1 Dirac Spin Liquid ansatz

The variational wave functions for the Dirac state are defined by

$$|\Psi\rangle = \mathscr{P}_G |\Phi_0\rangle, \tag{5.2}$$

where $|\Phi_0\rangle$ is the ground state of the auxiliary (non-interacting) Hamiltonian:

$$\mathscr{H}_0 = \sum_{\langle i,j\rangle,\sigma} \chi^0_{i,j} c^\dagger_{i,\sigma} c_{j,\sigma} + \text{h.c.}, \tag{5.3}$$

where $c^\dagger_{i,\sigma}$ ($c^\dagger_{i,\sigma}$) creates (destroys) a fermion on site i with spin $\sigma = \uparrow, \downarrow$; $\chi^0_{i,j}$ defines the hopping amplitude for nearest-neighbor sites (i,j). For the Dirac state, it takes values $\chi^0_{i,j} = \pm 1$ and the distribution of these bonds in the lattice is shown in figure 5.1. Note that $\chi^0_{i,j}$ is independent of spin flavor, implying that the wavefunction is a spin singlet i.e. has SU(2) symmetry. Let us first discuss properties of the state at mean field level, before Gutzwiller projection. Because of the periodic modulation of the hoppings, translational symmetry is still present, albeit with an enlarged 2×1 magnetic unit cell.

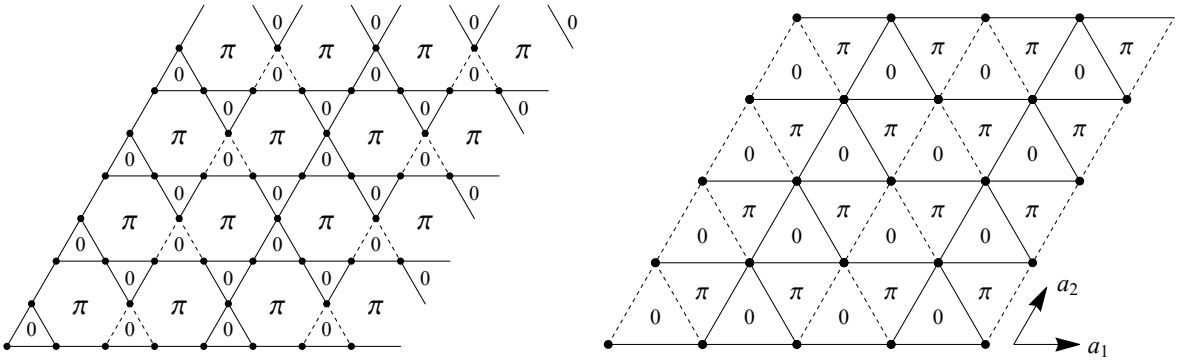

Figure 5.1: Hopping structure for the Dirac ansatz on the Kagome and Triangular lattices. We show one of several possible gauges to construct the hoppings. The solid and dashed lines refer to $\chi_{i,j} = 1$ and -1 respectively. The fluxes through the various polygons that make up the lattice are displayed on both lattices.

The mean field spectrum of the Dirac state hosts two Dirac cones per spin flavor. To see this, we must diagonalize the hamiltonian in fourier space. Below, we detail this calculation for the spinless tightbinding model on the Kagome lattice with periodic boundary conditions and $3 \times L \times L$ sites. The three site unit cell is enlarged to six sites upon adding the π fluxes, as shown in figure 5.2 (for the triangular lattice, the magnetic unit cell has instead two sites).

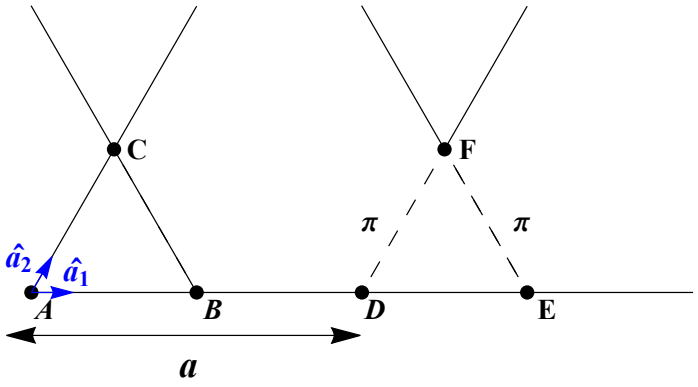

Figure 5.2: Magnetic unit cell for the Kagome Dirac state, comprising of 6 sites (A-F). The lattice translational vectors $\vec{a}_1, \vec{a}_2$ and lattice spacing a are also shown.

Let us start by defining the real space lattice vectors

$$\vec{a}_1 = a\hat{x} \qquad \vec{a}_2 = a/2\left(\hat{x} + \sqrt{3}\hat{y}\right) \tag{5.4}$$

If the origin is supposed at the A site, then we can define the coordinates of all other sites relative to this origin

$$\begin{gathered} \vec{r}_B = \frac{1}{2}\vec{a}_1 \qquad \vec{r}_D = \vec{a}_1 \qquad \vec{r}_E = \frac{3}{2}\vec{a}_1\hat{x} \\ \vec{r}_C = \frac{1}{2}\vec{a}_2 \qquad \vec{r}_F = \vec{a}_1 + \frac{1}{2}\vec{a}_2 \end{gathered} \tag{5.5}$$

Then, given a generic unit cell (m,n) whose A site is located at $\vec{R}_{m,n} = m(2\vec{a}_1) + n\vec{a}_2$, the position of all other sites is given by $\vec{X}_{m,n} = \vec{R}_{m,n} + \vec{r}_X$, where $X = A \ldots F$. Next, we define the creation (annhilation) operator $X^\dagger_{m,n}(X_{m,n})$ which creates (destroys) a fermion at the the location $\vec{X}_{m,n}$. Now we are in position to write down our tight-binding hamiltonian

$$\begin{aligned} H_{\text{mf}} = \sum_{m=1}^{L/2}\sum_{n=1}^{L}\Big[\left(A^\dagger_{m,n}B_{m,n} + B^\dagger_{m,n}C_{m,n} + C^\dagger_{m,n}A_{m,n}\right) + \left(D^\dagger_{m,n}E_{m,n} - E^\dagger_{m,n}F_{m,n} - F^\dagger_{m,n}D_{m,n}\right) + \\ \left(B^\dagger_{m,n}D_{m,n} + E^\dagger_{m,n}A_{m+1,n} + F^\dagger_{m,n}B_{m,n+1} + F^\dagger_{m,n}D_{m,n+1} + C^\dagger_{m,n}A_{m,n+1} + C^\dagger_{m,n}E_{m-1,n+1}\right)\Big] + \text{h.c} \end{aligned} \tag{5.6}$$

Note that the m index only sums till $L/2$ due to the doubling of the unit cell. The above complex looking expression can be easily dealt with by transferring to momentum space, by defining the following fourier transformed operators (X=$A \ldots F$)

$$\begin{aligned} X^\dagger_{\vec{k}} &= \frac{1}{\sqrt{N}}\sum_{m,n}\exp\left\{i\vec{k}\cdot\vec{X}_{m,n}\right\}X^\dagger_{m,n} \\ \implies X^\dagger_{m,n} &= \frac{1}{\sqrt{N}}\sum_{\vec{k}}\exp\left\{-i\vec{k}\cdot\vec{X}_{m,n}\right\}X^\dagger_{\vec{k}} \end{aligned} \tag{5.7}$$

where N is the number of unit cells, $N = L \times L/2$. Inserting (5.7) into (5.6) and simplifying using the identity

$$\sum_{m,n}\exp\left\{i\left(\vec{k}_1 - \vec{k}_2\right)\cdot\vec{R}_{m,n}\right\} = N\delta(\vec{k}_1 - \vec{k}_2) \tag{5.8}$$

we end up with the following matrix equation

$$\hat{H} = \sum_{\vec{k}} \left(A^\dagger_{\vec{k}} \; B^\dagger_{\vec{k}} \; C^\dagger_{\vec{k}} \; D^\dagger_{\vec{k}} \; E^\dagger_{\vec{k}} \; F^\dagger_{\vec{k}} \right) \mathscr{H}_{\vec{k}} \left(A_{\vec{k}} \; B_{\vec{k}} \; C_{\vec{k}} \; D_{\vec{k}} \; E_{\vec{k}} \; F_{\vec{k}} \right)^T$$

$$\mathscr{H}_{\vec{k}} = \begin{bmatrix}
0 & \exp\left(\frac{i\vec{k}\cdot\vec{a}_1}{2}\right) & 2\cos\left(\frac{\vec{k}\cdot\vec{a}_2}{2}\right) & 0 & \exp\left(\frac{-i\vec{k}\cdot\vec{a}_1}{2}\right) & 0 \\
\exp\left(\frac{-i\vec{k}\cdot\vec{a}_1}{2}\right) & 0 & \exp\left(\frac{i\vec{k}\cdot(\vec{a}_2-\vec{a}_1)}{2}\right) & \exp\left(\frac{i\vec{k}\cdot\vec{a}_1}{2}\right) & 0 & \exp\left(\frac{-i\vec{k}\cdot(\vec{a}_2-\vec{a}_1)}{2}\right) \\
2\cos\left(\frac{\vec{k}\cdot\vec{a}_2}{2}\right) & \exp\left(\frac{-i\vec{k}\cdot(\vec{a}_2-\vec{a}_1)}{2}\right) & 0 & 0 & \exp\left(\frac{i\vec{k}\cdot(\vec{a}_2-\vec{a}_1)}{2}\right) & 0 \\
0 & \exp\left(\frac{-i\vec{k}\cdot\vec{a}_1}{2}\right) & 0 & 0 & \exp\left(\frac{i\vec{k}\cdot\vec{a}_1}{2}\right) & -2i\sin\left(\frac{\vec{k}\cdot\vec{a}_2}{2}\right) \\
\exp\left(\frac{i\vec{k}\cdot\vec{a}_1}{2}\right) & 0 & \exp\left(\frac{-i\vec{k}\cdot(\vec{a}_2-\vec{a}_1)}{2}\right) & \exp\left(\frac{-i\vec{k}\cdot\vec{a}_1}{2}\right) & 0 & -\exp\left(\frac{i\vec{k}\cdot(\vec{a}_2-\vec{a}_1)}{2}\right) \\
0 & \exp\left(\frac{i\vec{k}\cdot(\vec{a}_2-\vec{a}_1)}{2}\right) & 0 & 2i\sin\left(\frac{\vec{k}\cdot\vec{a}_2}{2}\right) & -\exp\left(\frac{-i\vec{k}\cdot(\vec{a}_2-\vec{a}_1)}{2}\right) & 0
\end{bmatrix} \tag{5.9}$$

This matrix can be diagonalized to obtain the band structure of the model, as shown in Figure 5.3. Notably, two of the bands are flat with energy -2. The remaining four bands touch at specific $\vec{k}$ points, exhibiting linear Dirac dispersions around these points. The Dirac state on the triangular lattice features a two-site unit cell, resulting in only two bands. Both the triangular and Kagome lattices have hexagonal Brillouin Zones (BZ). However, due to the doubling of the unit cell in the Dirac state, the BZ is folded along the $\vec{b}_1$ direction, forming a rectangular 'reduced' BZ. The locations of the Dirac nodes, along with the reduced BZ, are illustrated in Figure 5.4.

It is important to note that the location of the Dirac cones in the BZ is gauge-dependent; however, the separation between them remains invariant [74]. With the specific gauge choices shown in Figure 5.1, the Dirac cones appear at the same $\vec{k}$ points for both systems. Additionally, Dirac-like dispersions also arise in the π flux state on the square lattice and in the simple uniform nearest-neighbor tight-binding model on the honeycomb lattice (graphene).

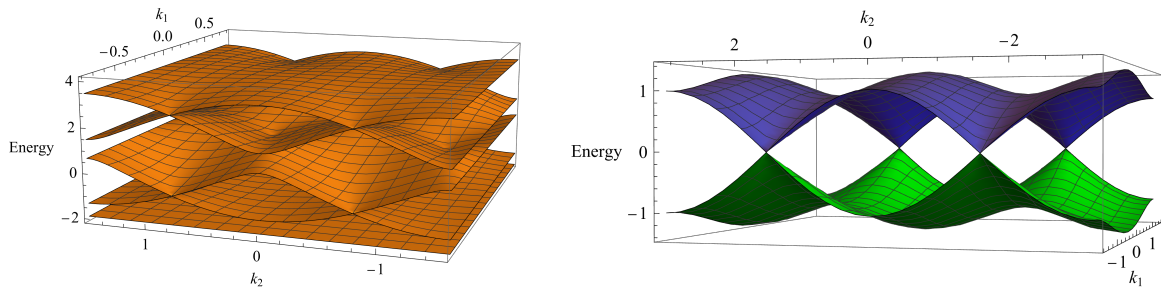

Figure 5.3: Energy bands for the Dirac states on the Kagome and triangular lattices. The Kagome system hosts two flat bands, and four dispersive ones, whereas the triangular lattice has only two bands which meet at 0 energy.

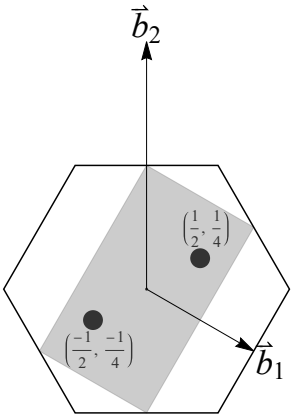

Figure 5.4: Positions of the Dirac nodes in the reduced BZ (shaded in gray) for both the Triangular and Kagome lattice Dirac states, with the gauge choice of figure 5.1. The coordinates (m,n) represent the vector $m\vec{b}_1 + n\vec{b}_2$. The reciprocal lattice vectors for the reduced BZ are also shown.

5.2 Monopole ansatz

Monopole excitations on the lattice can be constructed by inserting a single flux quantum (2π flux), and spreading it uniformly through all plaquettes. For doing this, we must generalize our auxiliary hamiltonian as follows

$$\mathscr{H}_0 = \sum_{\langle i,j\rangle,\sigma} \chi^0_{i,j} e^{i\alpha_{i,j}} c^\dagger_{i,\sigma} c_{j,\sigma} + \text{h.c.}, \tag{5.10}$$

Here, the additional phases $\alpha_{i,j}$ take into account the fluxes due to the monopole, and are chosen such that an uniform flux of $2\pi/L^2$ pierces every parallelogram of the lattice (comprising of two triangles and a hexagon for the Kagome lattice, and just two oppositely pointing triangles for the triangular lattice). We note that $\chi^0_{i,j}$ is unchanged from figure 5.1, thus the monopole excitation is constructed on top of a background of π fluxes on both lattices.

At this stage we emphasize a distinction between the Kagome and triangular lattices. In the former, one has an additional degree of freedom in deciding how the flux within a parallelogram is divided into the triangles and the hexagon (we assume that both triangles have the same flux). Therefore, we consider a parameter space of two variables (ϕ,θ) where ϕ denotes the amount of added flux per parallelogram in the lattice, and θ controls its distribution within the unit cell (see figure 5.5). In our convention, the fluxes through the hexagon (F_H) and each triangle (F_T) are given by

$$\begin{aligned} F_H &= \pi - 2\theta + 3\phi/4 \\ F_T &= \phi/8 + \theta \end{aligned} \tag{5.11}$$

In the above, π in F_H is the contribution from the Dirac background. Therefore, $\theta = 0$ corresponds to the choice where the added flux is divided within the hexagon and triangles in terms of area

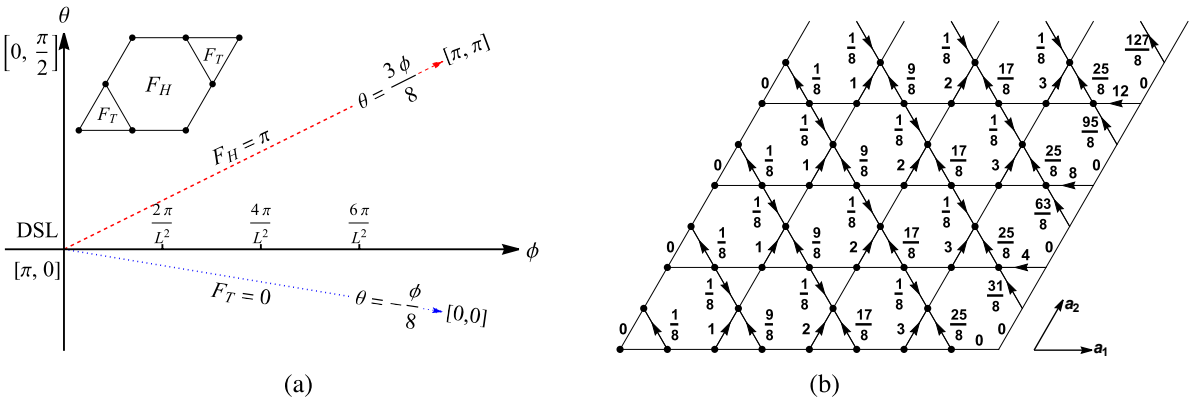

(a) (b)

Figure 5.5: (a) The plane (ϕ,θ) that defines the flux distribution in the unit cell considered in this work, shown in the inset. The hexagonal plaquette has a $F_H = \pi - 2\theta + 3\phi/4$ and two triangular ones have flux $F_T = \phi/8 + \theta$. The $[\pi,0]$ Dirac state lies at the origin, the uniform state $[0,0]$ is obtained with $\theta = -\phi/8$ for $\phi = \pm\pi$, and the $[\pi,\pi]$ state with $\theta = 3\phi/8$ and $\phi = 2\pi$. The quantized values of ϕ, obtained for a few monopoles are marked on the x-axis. (b) The complex argument $\alpha_{i,j}$, in units of $2\pi/L^2 = 2\pi/16$, of the hopping parameters $e^{i\alpha_{i,j}}$ (for $i \to j$) and $e^{-i\alpha_{i,j}}$ (for $j \to i$) of the fermionic Hamiltonian (5.10) that defines a single-monopole configuration (with $\theta = 0$) on the $L = 4$ cluster.

i.e, the added flux through the hexagon is six times that of each triangle. The situation for the triangular lattice is simpler; we only vary the external flux ϕ inserted in the lattice, and distribute this flux evenly within the two triangles of a parallelogram, preserving C_2 symmetry. Even after the fluxes through the elementary plaquettes of the lattice are determined, there are infinite possible choices for $\alpha_{i,j}$ due of $U(1)$ gauge freedom of the theory. However, the ground states of all these different auxiliary hamiltonians become identical after Gutzwiller projection. In the figures 5.5 and 5.6, we show one choice of hoppings to insert a monopole for both the Kagome and triangular lattices. Note that the hoppings on the last columns break translational symmetry along the $\vec{a}_2$ direction.

Several comments are in order. Firstly, note that because of the non-trivial fluxes through odd plaquettes on both lattices, the resultant spin wavefunction breaks time reversal and reflection symmetry, but preserves the product of the two. Therefore, this state represents a Chiral Spin Liquid (CSL). Then, by monitoring the energetics of the monopole states with respect to the DSL, we can also comment on the energetic stability of the DSL in comparison to (one family of) CSLs. Secondly, since each plaquette has a flux $2\pi/L^2$ piercing it, the total flux through a cylindrical strip of the lattice containing L sites is $2\pi/L$ (in contrast to the Hofstadter problem where it would have been a multiple of 2π). This necessarily implies non-trivial fluxes through the incontractible loops (marked in blue in figure 5.6) of the torus. In general, for a $L \times L$ lattice, the fluxes through these loops are $0, 2\pi/L, 4\pi/L, \ldots$. (a natural consequence of these non-trivial fluxes is that the boundary conditions ϕ_x, ϕ_y can be chosen modulo $2\pi/L$). Thus, translational symmetries are broken along both lattice directions, and the magnetic unit cell is as large as the

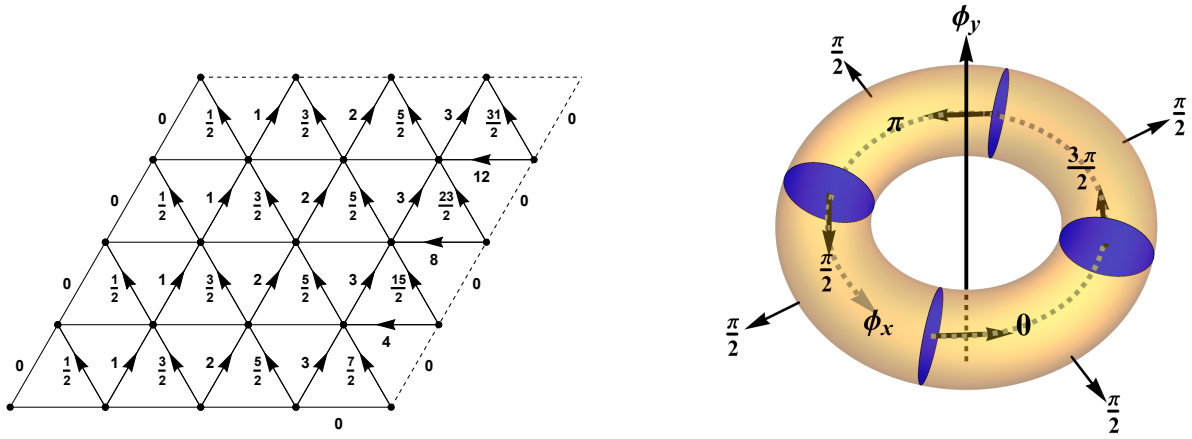

Figure 5.6: (a) Complex phases of hoppings $\alpha_{i,j}$ for the uniform monopole ansatz on $L = 4$ triangular lattice with periodic boundary conditions, in units of $2\pi/L^2$. Solid lines without arrows denote real uniform hopping. Each plaquette has a flux of $2\pi/L^2$ modulo 2π. (b) Fluxes through (one set of) incontractible loops of the $L = 4$ torus for the monopole state. Also shown schematically are the angles ϕ_x and ϕ_y, which control boundary conditions.

lattice itself. Despite this fact, it turns out that the state still has a well defined momentum in the thermodynamic limit. We will discuss this in more detail in the subsequent sections.

Inserting a monopole on top of the Dirac state results in a two fold degeneracy (for each spin) at the Fermi level (figure 5.7). This degeneracy is of topological origin, and is present for both the lattices and remarkably cannot be removed by modifying boundary conditions. [1] This is a consequence of the Atiyah-Singer Index theorem.

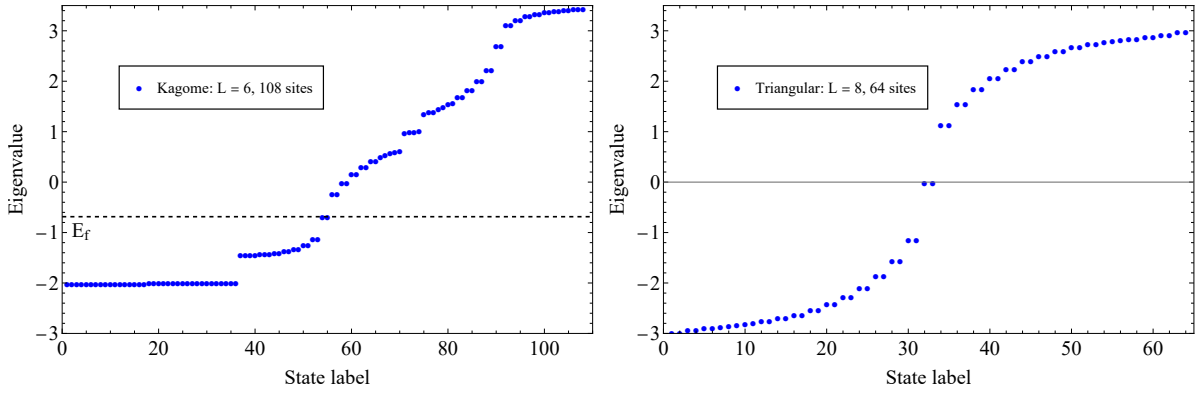

Figure 5.7: Two-fold degeneracy at the Fermi level in the single particle spectrum of the monopole state on the Kagome and triangular lattices. For the Kagome monopole ansatz, we take $\theta = 0$, and the fermi level is indicated by E_f (it is at 0 for the triangular).

This unremovable degeneracy at the Fermi level implies that there are several possibilities

[1] The spectrum in general is modified, but the levels close to the Fermi energy (and the two fold degeneracy) remain intact. For the Kagome lattice, the spectrum obviously varies with changing θ, but the degeneracy at the Fermi level remains robust.

to occupy the orbitals when constructing the many body monopole state. In particular, singlet and triplet monopoles can be constructed, which have different symmetry properties, as will be discussed in the next section.

5.3 Monopole momenta

In this section, we discuss the momentum quantum numbers of the monopole excitations. Recently, Song *et. al* have demonstrated using field theory techniques the symmetry quantum numbers of the monopole operators at the mean field level [260]. Here, we additionally report calculations on the Gutzwiller projected monopole states, both using exact diagonalization and VMC calculations. We focus on the triangular lattice in this section.

To evaluate the momentum quantum numbers on finite clusters, we compute the following expectation values for the mean field ($|\Phi\rangle$) and Gutzwiller projected ($|\Psi\rangle$) wavefunctions [260]

$$\begin{aligned} \frac{\langle\Phi|\mathcal{G}^m_{T_j}T_j|\Phi\rangle}{\langle\Phi|\Phi\rangle} &= Ae^{ik_j} \\ \frac{\langle\Psi|T_j|\Psi\rangle}{\langle\Psi|\Psi\rangle} &= A'e^{ik'_j} \end{aligned} \tag{5.12}$$

where $\mathcal{G}^m_{T_i}$ represents the gauge transformation at the which approximately compensates for the translation along the $\vec{a}_i$ direction. In figure 5.8, we show the gauge transformation for translations along $\vec{a}_1$. When calculating the momenta for the projected wavefunctions, this gauge transformation is omitted since mean-field wavefunctions connected by a $U(1)$ gauge transformation become identical after projection. In this case, the overlaps $\langle\Psi|\hat{T}_i|\Psi\rangle$ cannot be computed exactly and are estimated using Monte Carlo sampling.

As previously noted, the momentum of the monopole states is precisely defined only in the thermodynamic limit, when the amplitude $A = 1$. Monopole insertion results in a two fold degeneracy at the Fermi energy (per spin), and different occupations of these two levels yield three singlet and one triplet monopoles. Filling both these orbitals with the same spin species ($\uparrow$ or $\downarrow$) leads to the $S_z = +1, -1$ component of the triplet respectively. The $S_z = 0$ sector can be occupied in four ways, illustrated below

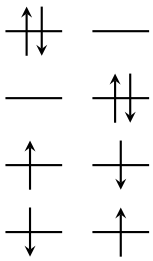

(5.13)

We call the above mean field states as $|\Phi_i\rangle$, $i = 1\ldots4$. From the above four states, we can construct three singlets and the $S_z = 0$ component of the triplet. While the unique triplet monopole is

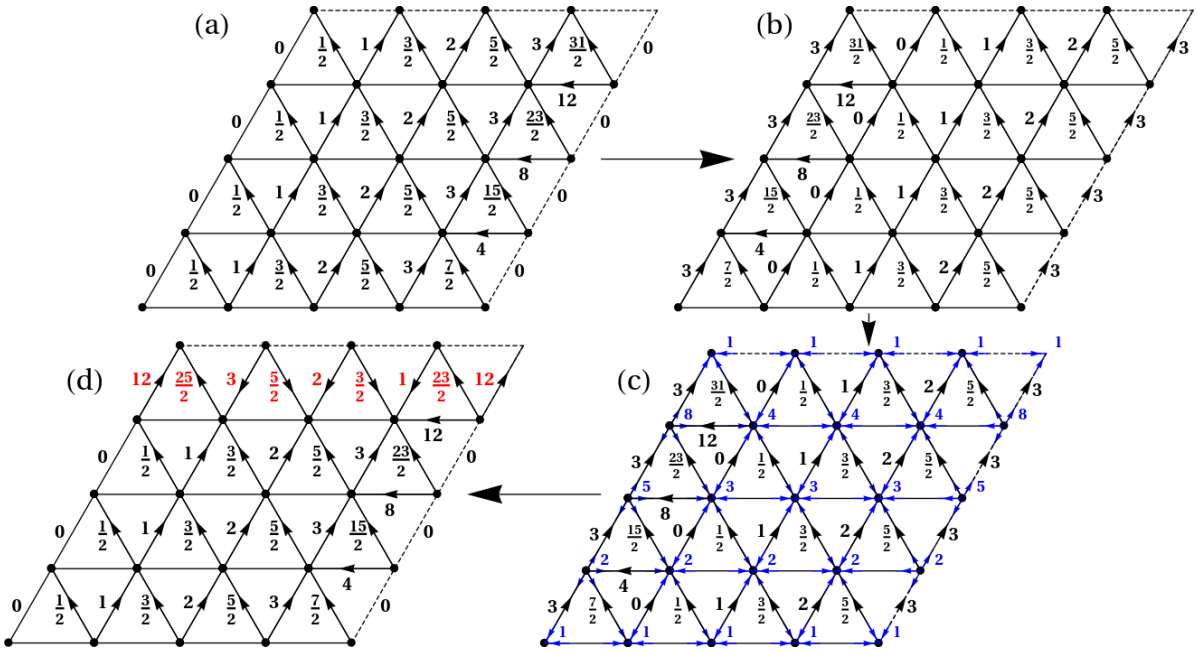

Figure 5.8: Gauge transformation to partially undo the effect of translations along the horizontal $\vec{a}_1$ direction for the monopole state on the 4×4 triangular lattice on a torus. The phases of all hoppings are in units of $2\pi/L^2$ with $L = 4$. (a) Hopping structure for the monopole state, reproduced from figure 5.6. (b) All hoppings translated along the horizontal direction by one lattice spacing. (c) The site dependent gauge transformation applied in shown in blue. (d) The resultant hoppings only differ from the initial monopole ansatz in $O(L)$ plaquettes (shown in red).

bound to have definite momentum in the thermodynamic limit, the singlet monopoles with definite momenta are expected to be superpositions of the above singlet states. To calculate the approximate eigenstates of translations on finite clusters for the singlet monopoles, we construct and co-diagonalize a pair of 4×4 matrices with elements $\langle \Phi_m | \mathcal{G}^m_{T_i} \hat{T}_i | \Phi_n \rangle$ (and $\langle \Psi_m | \hat{T}_i | \Psi_n \rangle$) ($i = 1,2$, and $m,n = 1 \ldots 4$) for the mean field (and projected) monopole states. The eigenstates of these matrices separate into two blocks of dimensions 3×3 and 1×1, corresponding to the singlet and triplet ($S_z = 0$ component) sector respectively.

Let us first mention the results of Lanczos diagonalization on a 6×6 cluster. We construct the exact projections of the Gutzwiller projected monopole variational states on the 36 momentum subspaces. The unique triplet state (shown in blue in Fig.5.9) is observed to have a sizable weight only at one of the two K nonequivalent points of the Brillouin Zone. The antimonopole state (not shown) will be centered at the K' point. The three singlet monopole states, have significant weight only at three of the X points in the Brillouin Zone, the remaining three points being described by the complex conjugate wavefunction. Fig. 5.9 displays in red the weights of one of these singlet states on different momenta subspaces.

We now discuss the behavior of the absolute value (A) and phase (k_i) of the eigenvalues of the overlap matrix as a function of system size. Figure 5.10 compares these quantities for mean-field

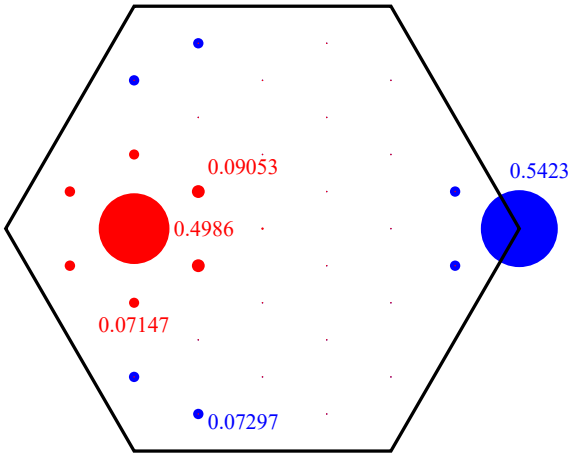

Figure 5.9: Projection of the Gutzwiller projected monopoles onto different momenta in the Brillouin zone for the 6×6 triangular lattice. The radius of the circles are proportional to the modulus squared of the projection, some numbers are listed for scale. All the weights add-up to one for normalization. The blue color refers to the triplet monopole, while the red color pertains to one out of the three singlet monopoles.

and projected monopole states, for the $S_Z = +1$ triplet and one of the three singlets. Obviously, since the Gutzwiller projector commutes with the translations, the thermodynamic values of the momenta of the projected states coincide with the ones obtained within the unprojected calculations. However, we observe a much faster convergence for the projected wavefunctions. For instance, the amplitude of the projected triplet monopole at $L = 16$ already exceeds the mean-field amplitude at $L = 80$.

The triplet monopole lies at one of the corners K of the Brillouin zone, and the momenta of the singlets converge to the three X points (connected by C_3 rotations) given by $(\vec{k}\cdot\vec{a}_1, \vec{k}\cdot\vec{a}_2) = (-2\pi/3, -\pi/3)$, $(\pi/3, -\pi/3)$ and $(\pi/3, 2\pi/3)$. Inserting a -2π (instead of $+2\pi$) flux would lead to the K' point for the triplet, and three other inversion-connected points $(\vec{a}\cdot\vec{b}_1, \vec{k}\cdot\vec{a}_2) = (2\pi/3, \pi/3)$, $(-\pi/3, \pi/3)$ and $(-\pi/3, -2\pi/3)$ for the singlets.

In summary, our investigation of the Gutzwiller-projected variational monopole states aligns with the expected behavior of the low-energy sector of QED in $2+1$ dimensions [254, 260], with the projected wavefunctions demonstrating significantly faster convergence towards exact eigenstates of translation operators. We note that we have also obtained similar results on the Kagome lattice.

Interestingly, the monopole excitations have a large overlap with particle-hole spinon excitations, obtained by starting from the Dirac state and allowing a different occupation of the fermionic levels. This approach, has been recently considered to assess the dynamical structure factor [102]. For the 6×6 cluster, we can improve this construction, by including states with three different boundary conditions. For the triplet case, starting from the Dirac unprojected state, we build all the possible particle-hole spinon excitations at $\mathbf{k} = (-2\pi/3, 2\pi/\sqrt{3})$ after projection. Then,

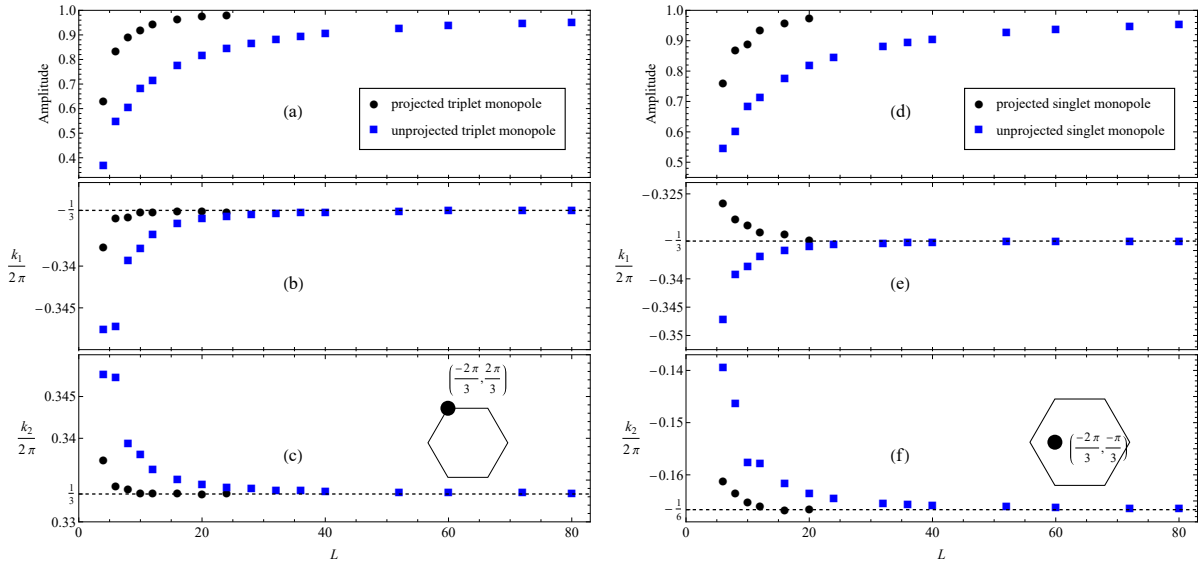

Figure 5.10: Triangular lattice: amplitude and phase of overlap in equation (5.12) for the triplet ((a)-(c)) and one of the three singlet monopoles ((d)-(f)) as a function of linear system size L. Results are shown both for the mean field overlaps (computed exactly as slater determinants) and the Gutzwiller projected wavefunctions (computed by monte carlo sampling). The mean field results coincide with those in [260]. The insets show the points $(\vec{k}.\vec{a}_1, \vec{k}.\vec{a}_2) = (k_1, k_2)$ on the Brillouin zone corresponding to the plots. The amplitude plot corresponds to k_1, and identical behavior is observed for k_2. The errorbars for the monte carlo data are smaller than the size of the symbols, and are estimated by a statistical sampling of the eigenvalues of the overlap matrices.

in the 27-dimensional subspace (corresponding to 9 linearly independent states for each boundary condition) spanned by these spinon states, we finds the optimal linear combination minimizing the energy (after projection). The spinon variational energy at $\mathbf{k} = (-2\pi/3, 0)$ is $E_{sp}/J_1 = -17.762$, while the monopole variational energy is $E_1/J_1 = -17.817$. Remarkably, the overlap between the monopole and the spinon states is 0.67 (or 0.92 for the normalized monopole state). Similarly, for the singlet monopole, the spinon variational energy is $E_{sp}/J_1 = -17.776$, to be compared with the monopole one $E_1/J_1 = -17.694$. The overlap between these two states is 0.64 (or 0.90). These results suggest that bare spinons and monopoles do not exist as free particles and cannot be disentangled in the exact eigenfunctions of the frustrated Heisenberg model.

5.4 Energetics

5.4.1 Monopole excitations

In this section, we study the variational energies of the monopole ansatzes for the Heisenberg models defined in equation (5.1). We will take $J_2 = J_1/8$ in $\mathscr{H}_{\text{Triangular}}$. The main questions we address are the following: (a) Is the DSL energetically stable or unstable to forming chiral states

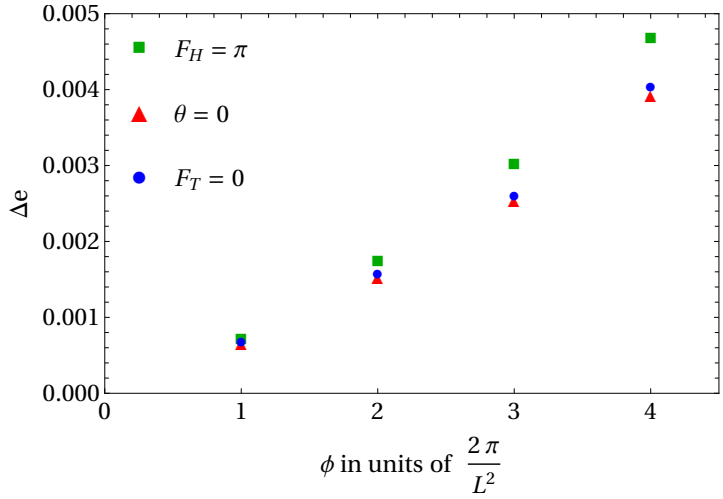

Figure 5.11: Energy (per site) difference between chiral and Dirac states as a function of ϕ for three cuts in the plane of Fig. 5.5. Variational Monte Carlo calculations are performed on a cluster with $L = 8$ (192 sites). The values of ϕ correspond to $N_m = 1,\ldots,4$ monopoles in the torus.

(with monopoles of generic charge Q)? (b) What is the energy gap of the monopole excitations in the thermodynamic limit after projection? (c) How do energetics of the monopoles compare with field theory calculations in the large N_f limit?

To answer these questions, we first construct the variational ansatzes for the singlet and triplet monopoles $|\Phi_{\text{mono}}\rangle$ by diagonalizing the tight binding hamiltonian (5.10). At the mean field level, the expectation value $\langle\Phi_{\text{mono}}|\mathscr{H}|\Phi_{\text{mono}}\rangle/\langle\Phi_{\text{mono}}|\Phi_{\text{mono}}\rangle$ can be computed exactly using Wick's theorem. This calculation is detailed in appendix A (in the more generic case of SU(N) permutation hamiltonian). However, the more interesting quantity is the expectation value for the projected wavefunction $|\Psi_{\text{mono}}\rangle = \mathscr{P}_G|\Phi_{\text{mono}}\rangle$ where $\mathscr{P}_G$ is the Gutzwiller projector onto the configuration space with one particle per site. The expectation values $\langle\Psi_{\text{mono}}|\mathscr{H}|\Psi_{\text{mono}}\rangle/\langle\Psi_{\text{mono}}|\Psi_{\text{mono}}\rangle$ are estimated using standard variational monte carlo techniques, which have been discussed in chapter 2.

Let us first discuss the Kagome system. In figure 5.11, the variational energies (per site) for three different cuts in the (ϕ,θ) plane are reported for $L = 8$: along $\theta = 3\phi/8$ (i.e., $F_H = \pi$, which connects the Dirac state to the $[\pi,\pi]$ one), along $\theta = -\phi/8$ (i.e., $F_T = 0$, which connects the Dirac state to the $[0,0]$ one), and $\theta = 0$. In all cases, the energy increases monotonously with ϕ. Since the ansatz with $\theta = 0$ has a lower energy than the other cuts, we will choose this flux distribution within the hexagon and the triangles of the unit cell. We note that the monopole momenta in the thermodynamic limit do not depend on the choice of the choice of θ.

Let us now move to the energetics of monopole excitations. The results for triplet and singlet monopole gaps (for the $Q = 1$ monopole corresponding to an insertion of 2π flux) are shown in Fig. 5.12 as a function of inverse system size $1/L$. In order to avoid complicated Monte Carlo calculations with multi-determinant states, the singlet state is constructed by occupying with two

fermions (with opposite spins) the same zero-energy level (not by the diagonalization of the 4×4 matrix, as discussed before); we verified that, on small clusters, this simple approach yields the same energy (within error-bars) as the calculation involving a linear superposition of different occupations of the zero-energy levels. We observe that the monopole excitations are gapless in the thermodynamic limit for both lattices, with an energy scaling inversely with linear system size. Thus, the Gutzwiller projection does not change the gapless nature of these excitations. Further, we observe that the singlet and triplet monopoles become degenerate for sufficiently large system sizes. These findings support the existence of a $U(1)$ Dirac spin liquid in the models in (5.1). We also construct particle-hole excitations of the Hamiltonian (5.3), by changing the fermion occupation in the unprojected state (i.e., by emptying one of the highest-energy single-particle orbital and filling one of the lowest-energy ones). Given the shape of the cluster, there are several ways to do this, since both these shells are four-fold degenerate (for each spin value). In particular, we construct particle-hole excitations on the same/opposite Dirac cone, and observe them to also be gapless in the thermodynamic limit.

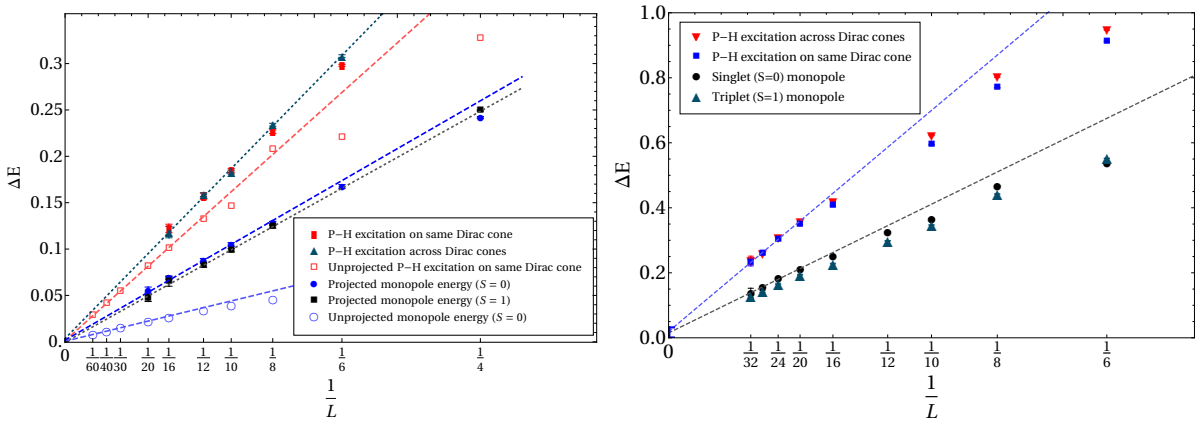

Figure 5.12: Size scaling of the single-monopole gap (with respect to the Dirac state) for both the singlet and triplet monopoles for the Kagome and triangular lattices respectively. The unprojected case (no Gutzwiller projection) is reported for the Kagome lattice for comparison. Particle-hole (P-H) spinon excitations of the Dirac wave function are also shown, either within the same Dirac cone or across the Dirac cones.

In addition, we consider higher values of the monopole charge Q, i.e., including a magnetic flux of $2\pi Q$. On finite clusters, for $Q \ll N$, there are $2Q$ zero-energy levels per spin (in some cases, the energies are not exacly zero, but still separated by the other ones). These states must be filled with $2Q$ fermions (with up or down spin), thus increasing the complexity for constructing many-body wave functions with a definite spin value. Then, we take a simplified approach and construct states with fermions occupying (with opposite spins) the same zero-energy level, thus leading to a singlet. We remark that no differences in the energy of Gutzwiller-projected states are detected by occupying different single-particle levels. The energy of charge-Q monopoles is expected to scale with a non-trivial behavior, as reported in the field-theoretical calculations of

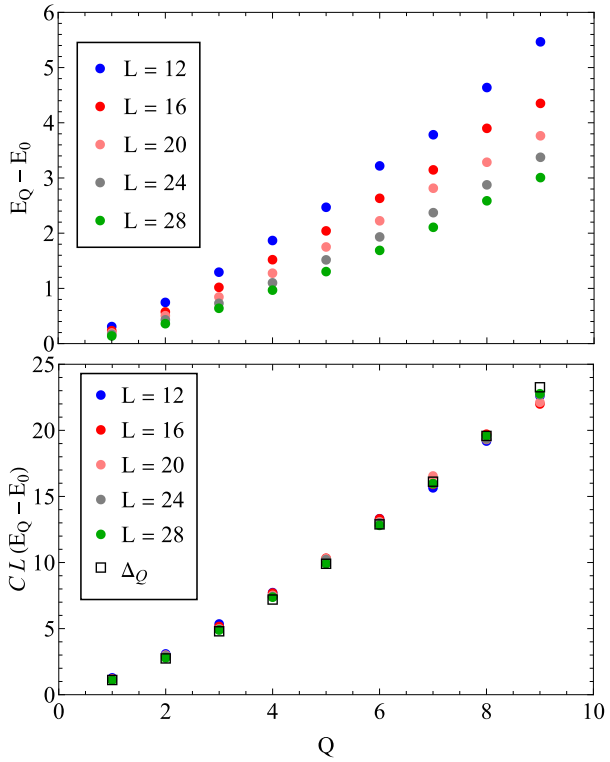

Figure 5.13: Upper panel: Variational energy of charge-Q (singlet) monopole excitations $E_Q - E_0$, as a function of Q for different sizes of the cluster L. Lower panel: the excitations energies multiplied by $C \times L$ (where $C \approx 0.28$, see text) and compared with the scaling dimensions Δ_Q (including the factor $N_f = 4$) obtained by field-theoretical calculations in the limit of a large number of Dirac points in the fermionic spectrum [262].

Ref. [262] for the leading-order term in the $1/N_f$ expansion. Our results for $E_Q - E_0$ are reported Fig. 8.17 for a few values of Q and different cluster sizes L. In addition, we also report the direct comparison between our variational results multiplied by L and the scaling dimensions (including N_f, taken to be equal to 4) obtained by field-theoretical calculations performed within the large-N_f expansion [262]. Given the different geometries considered in these two calculations (the torus and the conformal sphere in the variational and analytical approaches, respectively), and the different energy scales ($J_1 = 1$ and $\hbar = c = 1$, in the variational and analytical approaches, respectively), we allow for having a "renormalization" in our results, which are multiplied by $C \approx 0.28$. Remarkably, there is a nice agreement, even if the analytical calculations pertains to the $N_f \to \infty$ limit, while our numerical simulations apply to the $N_f = 4$ case. This outcome gives further support for the stability of the Dirac spin liquid in the $J_1 - J_2$ Heisenberg model on the triangular lattice and the fact that the corresponding quantum spin liquid is described by quantum electrodynamics in $2+1$ dimensions. We note that similar calculations were performed for monopole excitations on the Kagome Heisenberg model with a very good collapse to field theory predictions.

5.4.2 Localized flux excitations

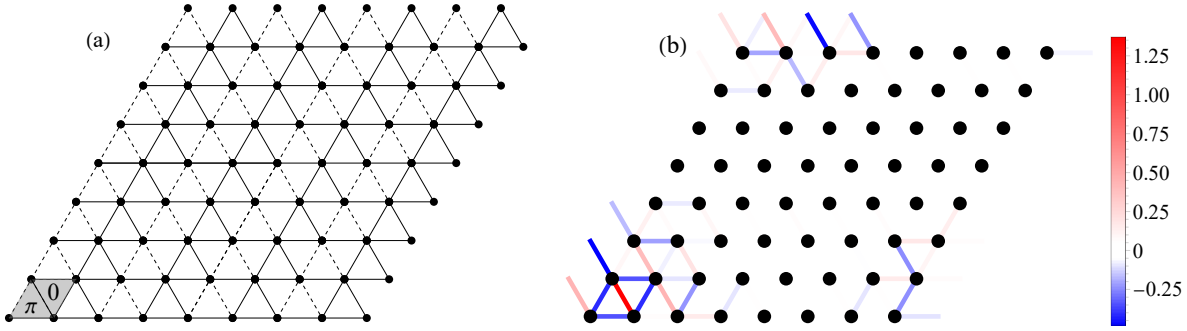

Figure 5.14: Localized flux excitations on the triangular lattice. (a) The hopping amplitudes χ_{ij} of the Dirac *Ansatz* with the insertion of two localized gauge fluctuations in the rhomboid (shaded) plaquettes on the cluster with $L = 8$. Solid and dashed lines denote the hoppings $\chi_{ij} = 1$ and -1, respectively. (b) Rescaled nearest-neighbor energies $\mathscr{S}(i,j)$ of Eq. (5.14) for the Gutzwiller-projected wave function on the same cluster.

In this section, we discuss the construction and energetics of localized flux excitations on the triangular lattice $J_1 - J_2$ model. Within the monopole construction the total gauge flux $2\pi Q$ is spread uniformly, implying an entire reorganization of the fermionic hoppings in the whole cluster; here, instead, we want to consider local modifications of the flux, similarly to vison excitations in $\mathbb{Z}_2$ spin liquids [20]. Of course, this kind of an *Ansatz* is not expected to be part of the exact spectrum of in the thermodynamic limit, as well as in the quantum field theory for its low-energy behavior; indeed, we observe that creating a local perturbation on top of the Dirac *Ansatz* results in a state that has a large overlap with the unperturbed wave function, being thus in striking difference with $\mathbb{Z}_2$ spin liquids.

The prototypical example of such localized gauge excitations is shown in Fig. 5.14, where a single rhomboidal plaquette (e.g., two triangles) carries 2π flux (on top of the flux given by the Dirac *Ansatz*, i.e., the two triangles reverse their flux $0 \leftrightarrow \pi$). This configuration would correspond (in a $\mathbb{Z}_2$ spin liquid) to the creation of a couple of nearest-neighbor visons. The actual location of the defect in the pattern of fluxes may be detected by considering spin-spin correlations at nearest neighbors:

$$\mathscr{S}(i,j) = \frac{\langle \Psi_{\rm loc} | \mathbf{S}_i \cdot \mathbf{S}_j | \Psi_{\rm loc} \rangle - \langle \Psi_0 | \mathbf{S}_i \cdot \mathbf{S}_j | \Psi_0 \rangle}{\left| \langle \Psi_0 | \mathbf{S}_i \cdot \mathbf{S}_j | \Psi_0 \rangle \right|}, \tag{5.14}$$

where $|\Psi_{\rm loc}\rangle$ is the state containing two localized fluxes and $|\Psi_0\rangle$ is the Dirac *Ansatz*. Notably the spin-spin correlations of $|\Psi_{\rm loc}\rangle$ differ from the ones of the Dirac state $|\Psi_0\rangle$ only in the vicinity of the perturbation, see Fig. 5.14.

Remarkably, the variational energy of the state with the "vison excitation" is particularly low (e.g., $E_{\rm loc} - E_0 \approx 0.13$). However, this result is due to the fact that $\langle \Psi_0 | \Psi_{\rm loc} \rangle \approx 0.92$ (approximately constant from $L = 8$ to 12). This result gives an additional evidence in favor of a gapless $U(1)$ spin

liquid described by the Gutzwiller-projected fermionic *Ansatz*.

5.5 Conclusion

Dirac spin liquids are exotic quantum states characterized by low-energy excitations involving spinons and monopoles. Investigating these excitations is essential for identifying experimental signatures and guiding the discovery and characterization of spin liquid candidates. In this study, we thoroughly examined monopole excitations in the nearest neighbor Kagome Heisenberg model and the triangular lattice $J_1 - J_2$ ($J_2 = J_1/8$) model, employing exact diagonalization and variational Monte Carlo (VMC) techniques. Our key findings in this study are:

1. Monopole and spinon excitations are gapless in the thermodynamic limit, on both lattices.
2. The variational energy of monopole states with generic charge Q agree remarkably well with field theory predictions for QED_{2+1} in the presence of a large number of fermion flavors N_f.
3. The projected monopole wavefunctions converge more rapidly (than the mean field slater determinants) to exact eigenstates of the translation operators, exhibiting momenta consistent with field theory predictions.
4. Flux excitations localized on pairs of individual triangular plaquettes are gapped in the thermodynamic limit due to having a very large overlap with the ground state.

Our results illuminate the intricate physics of frustrated Heisenberg models on the Kagome and the triangular lattice, and provide supporting evidence for a Dirac spin liquid ground state in these systems.

CHAPTER 6

CONCLUSION

Quantum spin liquids (QSL) are exotic phases of matter where the magnetic moments (spins) of electrons remain disordered even at absolute zero temperature, defying conventional magnetic order. They states do not have local order parameters, and lie beyond the Landau-Ginsburg paradigm. They are also characterized by many-body quantum entanglement, that give rise to fascinating phenomena such as fractionalization of excitations and topological order, as discussed in chapter 1.

In this thesis, we studied two questions about QSLs in two dimensions, one about the representability of Chiral spin liquids using fermionic Projected Entangled Pair States (fPEPS), and the other about the nature of low energy excitations of Dirac spin liquids (DSL) (focusing on monopole excitations).

The first question was discussed in chapter 4. We provided robust evidence that PEPS can effectively represent chiral spin liquid (CSL) phases. This was achieved by constructing fPEPS approximations of Gutzwiller-projected Chern insulators and demonstrating that Gutzwiller-projected fermionic PEPS (with finite bond dimension) can accurately capture the correct topological ground-state degeneracy of the CSL. Furthermore, we extended our analysis beyond Gaussian fPEPS, exploring general fPEPS without constraints on the number of variational parameters, to test whether fPEPS can represent generic CSL phases arising in spin systems. By optimizing a fPEPS to describe the CSL phase in a frustrated Heisenberg antiferromagnet, we confirmed that the chiral edge modes in the entanglement spectrum align with predictions from conformal field theory. Notably, we found that fermionic PEPS exhibit a single chiral branch in the odd sector of the entanglement spectrum, in contrast to conventional bosonic PEPS, which display a redundant second branch. These findings underscore the potential of fermionic PEPS as a powerful tool for

studying chiral spin liquid phases and faithfully capturing their topological properties.

Additionally, we studied the low energy excitations of gapless Dirac Spin Liquids (DSL), which are good variational ansatzes for the ground state of Heisenberg models on the triangular (J_1-J_2) and Kagome lattices. We constructed variational ansatzes for monopole, spinon and localized flux excitations, and studied their energetics. We demonstrated that these models host monopole and spinon excitations that remain gapless even after applying Gutzwiller projection. Further, we computed the momenta of the monopoles (which are well defined in the thermodynamic limit), and found that the projected monopole wavefunctions converge much faster than the mean field wavefunctions to the field theory predictions. We also observed remarkable agreement between the energetics of general charge Q monopole excitations, and field theory computations of monopole scaling dimensions performed on the conformal sphere. We believe that our findings provide further evidence for the stable $U(1)$ spin liquid ground state in these models.

In this thesis, we have made a modest contribution towards the study of Dirac and Chiral spin liquids in two-dimensional systems. However, several questions and avenues for further research remain open. One promising direction is to investigate whether a variational Monte Carlo approach can be applied to study the edge states of topological chiral spin liquids on cylindrical geometries, starting from a Gaussian fermionic PEPS ansatz. Regarding Dirac spin liquids, the low-energy behavior of monopoles and spinons is highly intricate, and much remains to be understood about their dynamics in a lattice setting. An intriguing possibility for future research is to numerically explore a phase transition out of the $U(1)$ spin liquid phase via monopole proliferation. Additionally, the construction of the photon excitation of QED on a lattice is also an open problem. We leave these questions for future investigation.

CHAPTER 7

LIST OF PUBLICATIONS

1. Piercing the Dirac spin liquid: From a single monopole to chiral states.
   Sasank Budaraju, Yasir Iqbal, Federico Becca, and Didier Poilblanc, Phys. Rev. B 108, L201116 (2023).

2. Simulating chiral spin liquids with fermionic projected entangled pair states.
   Sasank Budaraju, Didier Poilblanc, and Sen Niu, Phys. Rev. B 110, 064402 (2024).

3. Monopole excitations in the $U(1)$ Dirac spin liquid on the triangular lattice.
   Sasank Budaraju, Alberto Parola, Yasir Iqbal, Federico Becca, and Didier Poilblanc, arXiv:2410.18747 (2024).

CHAPTER 8

RÉSUMÉ EN FRANÇAIS

Cette thèse porte sur les liquides de spin quantiques (QSL), des phases exotiques de la matière qui ont pris de l'importance au cours des dernières décennies [1]. Les liquides de spin quantiques sont le plus souvent caractérisés par leur manque d'ordre magnétique même à température nulle, mais ils présentent plusieurs autres propriétés exotiques. Ce sont des états intriqués à plusieurs corps, qui peuvent héberger des excitations fractionnées (appelées "spinons "). En effet, dans le célèbre modèle de "code torique" proposé par Kitaev [20], l'état fondamental est un QSL, et héberge des excitations fractionnées qui sont des anyons. Ainsi, les QSL sont intimement liés à l'informatique quantique, ainsi qu'à la supraconductivité à haute température [1]. Un énorme travail théorique a contribué à façonner notre compréhension de ce sujet (théories de jauge, QFT, topologie). Il est désormais entendu que les théories de jauge sont un langage très important pour comprendre la physique à basse énergie des QSL. En effet, différents liquides de spin peuvent être caractérisés par leur structure de jauge à basse énergie, comme proposé par Wen. De plus, des méthodes numériques ont également été conçues pour représenter les états de liquides de spin quantiques et les rechercher dans des modèles de spin. Ce dernier est crucial car ces états sont généralement hors de portée des solutions analytiques exactes (sauf dans de rares cas). Des techniques numériques robustes peuvent parfois être la seule ligne d'attaque pour comprendre la physique des systèmes de spin du monde réel.

Enfin, des efforts expérimentaux importants ont été réalisés pour identifier les liquides de spin quantiques dans la nature, mais un consensus universel sur un matériau présentant toutes les caractéristiques prédites des QSL n'a pas encore été atteint. En effet, le comportement à basse énergie des QSL est très subtil, caractérisé par de nouvelles particules émergentes et l'intrication à plusieurs corps - deux phénomènes extrêmement difficiles à établir expérimentalement. Néanmoins, la recherche reste une frontière en physique de la matière condensée, et le nombre de

candidats QSL a augmenté de façon spectaculaire au cours de la dernière décennie. La découverte d'un véritable matériau QSL constituera certainement une grande avancée de la physique de la matière condensée et aura de profondes implications pour les applications pratiques. Dans cette thèse, nous utiliserons une technique numérique connue sous le nom de Monte Carlo quantique variationnel pour mieux comprendre les propriétés de certains QSL. Plus précisément, nous progressons dans la compréhension des deux sujets suivants:

1. **Représentations de réseaux tensoriels de liquides de spin chiraux *avec gap* et leurs propriétés topologiques.**

2. **Excitation à basse énergie de liquides de spin de Dirac *sans gap* et leur stabilité dans les modèles de spin.**

Dans ce qui suit, nous décrirons plus en détail le contexte des problèmes auxquels nous nous attaquons, leur importance, nos résultats et leurs implications. Dans les sections suivantes, nous donnerons un aperçu détaillé des problèmes abordés dans cette thèse, de leur importance, des résultats obtenus et de leurs implications plus larges. Nous commencerons par décrire les méthodes numériques employées, en particulier la méthode VMC (section 8.1) et la méthode des réseaux tensoriels (section 8.2). Nous présenterons et discuterons ensuite les résultats de cette thèse dans les sections 8.3 et 8.4.

8.1 Monte Carlo Variationnel (VMC)

La VMC est une méthode puissante pour étudier les diagrammes de phase à température nulle, les états fondamentaux et les excitations à basse énergie des systèmes quantiques à plusieurs corps.

Introduite pour la première fois dans les années 1960, la VMC a d'abord été développée pour étudier l'état fondamental de l'hélium liquide [75–77]. Elle est depuis devenue une technique standard dans de nombreux domaines, notamment la physique nucléaire [78], la chimie quantique [79] et les systèmes fortement corrélés [80]. Des schémas d'optimisation sélectionnés (par exemple la reconfiguration stochastique [81, 82]) ont permis l'étude de fonctions d'onde variationnelles avec un grand nombre de paramètres.

Le VMC est particulièrement bien adapté à l'étude des liquides de spin, car à partir de modèles spinon/parton étroitement liés, la projection de Gutzwiller peut être implémentée exactement pour construire des fonctions d'onde variationnelles qui vivent dans l'espace de Hilbert du spin. Différents états de liquide de spin avec les symétries de réseau et de jauge requises peuvent être construits selon la classification des groupes de symétrie projective (PSG) discutée dans le chapitre précédent. Comme nous travaillons directement à température nulle, la technique VMC ne souffre pas du fameux « problème de signe » et n'impose donc aucune restriction sur les termes

de l'hamiltonien. La frustration étant un facteur clé dans la stabilisation des phases liquides de spin, le VMC s'avère être un outil puissant pour l'étude de ces systèmes.

Dans cette section, nous discuterons de la méthode VMC, en soulignant ses principes de base et sa mise en œuvre pratique. Le traitement ici est emprunté à [80], et est limité aux ansatzes avec une symétrie rotationnelle de spin $SU(2)$.

8.1.1 Idée principale

Le VMC commence par une famille de fonctions d'onde d'essai $|\Psi(\{\alpha_i\})\rangle$ paramétrées par un ensemble de paramètres variationnels $\{\alpha_i\}$ proposés pour décrire l'état fondamental d'un système $\hat{H}$ de particules interagissant entre elles. L'échantillonnage de Monte Carlo est ensuite utilisé pour calculer l'énergie variationnelle de ces fonctions d'onde

$$E_{\text{var}} = \frac{\langle\Psi|\hat{H}|\Psi\rangle}{\langle\Psi|\Psi\rangle} \tag{8.1}$$

Le principe variationnel de la mécanique quantique garantit que E_{var} est limité par le bas par la véritable énergie de l'état fondamental E_{gs} du système. Par conséquent, en optimisant les paramètres variationnels $\{\alpha_i\}$, la technique cherche à minimiser l'énergie, réalisant ainsi la meilleure approximation de l'état fondamental dans la famille de fonctions d'onde choisie.

Considérons un système de N particules de spin 1/2 sur un réseau. L'espace de Hilbert décrivant les états de ce système est de dimension 2^N. Par conséquent, pour les systèmes de taille même modérée, la mémoire de l'ordinateur nécessaire pour stocker l'hamiltonien à plusieurs corps et la fonction d'onde explose. Il est clair que la valeur espérée ci-dessus ne peut pas être évaluée exactement.
Pour surmonter cette difficulté, nous reformulons la valeur espérée en introduisant une identité $\mathbb{I} = \sum_x |x\rangle\langle x|$

$$\begin{aligned}\frac{\langle\Psi|H|\Psi\rangle}{\langle\Psi|\Psi\rangle} &= \sum_x \frac{|\langle x|\Psi\rangle|^2}{\langle\Psi|\Psi\rangle}\frac{\langle x|H|\Psi\rangle}{\langle x|\Psi\rangle} \\ &\equiv \sum_x p(x)\, e_L(x)\end{aligned} \tag{8.2}$$

où $p(x)$ est une distribution de probabilité normalisée

$$p(x) = \frac{|\langle x|\Psi\rangle|^2}{\langle\Psi|\Psi\rangle} \tag{8.3}$$

et $e_L(x)$ est appelé estimateur local de $\hat{H}$

$$e_L(x) = \frac{\langle x|H|\Psi\rangle}{\langle x|\Psi\rangle} \tag{8.4}$$

L'équation ci-dessus (8.2) est exacte si nous faisons la somme de tous les états de base $|x\rangle$

dans l'espace de Hilbert, ce qui est clairement irréalisable. Cependant, nous ne choisissons qu'un minuscule sous-ensemble de l'espace entier, et ce choix est effectué par *échantillonnage* de la distribution de probabilité à l'aide de procédures Monte Carlo standard, par exemple les algorithmes de Metropolis. Ainsi, si l'échantillonnage peut être effectué, l'estimation de l'énergie variationnelle est donnée par

$$\langle E \rangle = \frac{1}{M} \sum_{\{x_i\}}^{M} e_L(x_i) \tag{8.5}$$

où $\{x_i\}$ est l'ensemble des M états auxquels accède la chaîne de Markov. L'énergie locale est généralement évaluée en introduisant un autre ensemble complet d'états, comme suit

$$\frac{\langle x|H|\Psi\rangle}{\langle x|\Psi\rangle} = \sum_{x'} \langle x|H|x'\rangle \frac{\langle x'|\Psi\rangle}{\langle x|\Psi\rangle} \tag{8.6}$$

Si l'hamiltonien implique des interactions locales (comme ce sera le cas dans les systèmes de spin que nous étudions), alors la quantité $\langle x|H|x'\rangle$ sera non nulle pour très peu de $|x'\rangle$, et est facile à évaluer. La quantité principale au cœur de toutes les simulations VMC est alors le taux de recouvrement

$$\boxed{O(x',x) = \frac{\langle x'|\Psi\rangle}{\langle x|\Psi\rangle}} \tag{8.7}$$

Cette quantité est également au cœur de l'algorithme de Metropolis, où la probabilité d'acceptation du mouvement $|x\rangle \rightarrow |x'\rangle$ dépend du rapport

$$\frac{p(x')}{p(x)} = \left| \frac{\langle x'|\Psi\rangle}{\langle x|\Psi\rangle} \right|^2 \tag{8.8}$$

L'intuition sous-jacente est que les principales contributions à la moyenne de (8.2) proviennent des états $|x\rangle$ qui sont proches des maxima de $p(x)$. Par conséquent, l'algorithme de Metropolis augmente la probabilité d'échantillonner les configurations qui ont un chevauchement significatif avec $|\Psi\rangle$, améliorant ainsi la précision de l'approximation.

Nous notons également qu'une autre observable cruciale à suivre est la variance, donnée par

$$\sigma^2 = \frac{\langle \Psi|\hat{H}^2|\Psi\rangle}{\langle \Psi|\Psi\rangle} - E^2 = \frac{\langle \Psi|\left(\hat{H}-E\right)^2|\Psi\rangle}{\langle \Psi|\Psi\rangle} \tag{8.9}$$

Cette quantité disparaît si $|\Psi\rangle$ est un état propre exact de $\hat{H}$. Par conséquent, la variance est une mesure utile car elle a une limite inférieure claire de zéro. Au cours d'une optimisation VMC typique, l'énergie et la variance sont suivies, et elles diminuent au fur et à mesure que l'optimisation progresse.

Comment calculons-nous les chevauchements dans l'équation (8.7)?

Pour cela, nous devons parler de la manière dont les fonctions d'onde variationnelles sont construites. Tout au long de cette thèse, les fonctions d'onde variationnelles sont construites par

Gutzwiller en projetant l'état fondamental d'un hamiltonien à sauts de liaisons fortes.

Considérons un exemple simple d'hamiltonien de champ moyen:

$$\hat{H}_{\mathrm{MF}} = \sum_{i,j,\sigma} \chi_{ij}\, c^{\dagger}_{i,\sigma} c_{j,\sigma} + \mathrm{h.c.} \tag{8.10}$$

où i, j désigne les spins sur un réseau à N sites, et $\sigma = \{\uparrow, \downarrow\}$ est l'indice de spin. Nous choisissons les sauts χ_{ij} indépendants de σ pour plus de simplicité, garantissant une symétrie de rotation du spin. Cet hamiltonien peut être facilement diagonalisé, pour obtenir les orbitales $\phi^{\dagger}_{\alpha,\sigma}$

$$\phi^{\dagger}_{\alpha,\sigma} = \sum_{R=1}^{N} U_{R\alpha} c^{\dagger}_{R\sigma} \tag{8.11}$$

La matrice U est la matrice des vecteurs propres $N \times N$ obtenue en diagonalisant $\hat{H}_{\mathrm{MF}}$ (elle est diagonale par blocs dans le secteur de spin). Nous construisons ensuite l'état fondamental du champ moyen en remplissant les états propres de plus basse énergie jusqu'au niveau de Fermi.

$$|\Phi\rangle = \left[\prod_{\alpha=1}^{N/2} \phi^{\dagger}_{\alpha,\uparrow}\right]\left[\prod_{\alpha=1}^{N/2} \phi^{\dagger}_{\alpha,\downarrow}\right]|0\rangle \tag{8.12}$$

C'est le point de départ d'une simulation VMC. De manière générale, cette fonction d'onde contiendra des termes avec deux (ou zéro) particules sur un site. Pour obtenir une fonction d'onde de spin valide, nous devons appliquer le projecteur de Gutzwiller, $|\Psi\rangle = \hat{P}_G |\Phi\rangle$. Dans la simulation, nous calculons les chevauchements de la fonction d'onde $|\Psi\rangle$ avec une configuration générique $|x\rangle$

$$|x\rangle = \left[c^{\dagger}_{r_1\uparrow} c^{\dagger}_{r_2\uparrow} \ldots\right]\left[c^{\dagger}_{r'_1\downarrow} c^{\dagger}_{r'_2\downarrow} \ldots\right]|0\rangle \tag{8.13}$$

où $\{r_i\}$ ($\{r'_i\}$) est une liste des emplacements des spins up (down). Tous les éléments des deux listes doivent être distincts selon l'exclusion de Pauli. Dans le cas où $|x\rangle$ n'a pas de sites vacants ou doublement occupés, il est facile de voir que les recouvrements $\langle x|\Phi\rangle$ et $\langle x|\Psi\rangle$ coïncident. Dans les modèles considérés dans cette thèse, cette condition est toujours satisfaite. Ainsi, en échantillonnant uniquement les $|x\rangle$ qui se trouvent dans le sous-espace contenant une particule par site, la projection de Gutzwiller est implicitement prise en compte dans l'algorithme VMC.

Au niveau du champ moyen, on peut facilement calculer $\langle x|\Phi\rangle$. Évidemment, on peut le décomposer en calculs séparés pour chaque secteur de spin. Il s'avère que chacun de ces chevauchements est donné par le déterminant d'une matrice plus petite construite à partir de U (déterminants de Slater).

De manière générale, pour N particules, nous pouvons écrire le chevauchement comme

$$\boxed{\langle x|\Phi\rangle = \det U_{\{R^{\uparrow}\alpha\}} \det U_{\{R^{\downarrow}\alpha\}}} \tag{8.14}$$

où $R^{\uparrow}$ ($R^{\downarrow}$) désigne les positions de tous les spins $\uparrow$ ($\downarrow$) , α désigne les orbitales occupées et $U_{\{R^{\uparrow}\alpha\}}$

est la notation que nous utilisons pour la sous-matrice de U.

Nous terminons par un dernier commentaire. Nous avons vu que les recouvrements $\langle x|\Phi\rangle$ sont centraux pour une simulation VMC. Cependant, ils sont assez coûteux à calculer : l'évaluation du déterminant d'une matrice $N \times N$ implique $O(N^3)$ opérations. Nous notons que la simulation ne nécessite que des ratios de recouvrements : $\frac{\langle x'|\Phi\rangle}{\langle x|\Phi\rangle}$. Par conséquent, si les configurations $|x'\rangle$ et $|x\rangle$ ne sont que légèrement différentes (par exemple connectées par un retournement de spin), alors il existe en fait une autre méthode pour calculer les ratios de déterminants, en utilisant les matrices dites W. Cela réduit le coût de calcul de $O(N^3)$ à $O(N^2)$. Nous renvoyons le lecteur à [80] pour plus de détails.

8.1.2 Simulation VMC typique, considérations pratiques

Dans cette section, nous décrirons la structure de base d'une simulation VMC et les principaux calculs impliqués.

0. Initialiser les objets prérequis suivants:
    - Matrice des vecteurs propres U qui définit l'ansatz, $\Psi(\{\alpha\})$. Elle est généralement obtenue par diagonalisation d'un hamiltonien auxiliaire à liaison étroite.
    - Un état de base initial $|x_0\rangle = |\uparrow\downarrow\downarrow\uparrow\uparrow\ldots\rangle$, et un vecteur qui suit l'ordre des opérateurs fermion dans $|x\rangle$.
    - Tableaux des voisins les plus proches (et plus éloignés si nécessaire) pour chaque site.
    - Les matrices $W^{\uparrow}, W^{\downarrow}$ correspondant à la configuration $|x\rangle$.
1. Créer deux boucles, l'une imbriquée dans l'autre. Après chaque itération de la boucle extérieure, les observables du modèle de spin seront calculées.
2. La boucle interne est typiquement de $O(N)$ étapes (pour créer des échantillons non corrélés). À chaque itération, proposer une nouvelle configuration $|x'\rangle$ (généralement reliée à $|x\rangle$ par un retournement de spin). Calculer $p(x',x) = \left|\frac{\langle x'|\Psi\rangle}{\langle x|\Psi\rangle}\right|^2$ et comparer à un nombre aléatoire $r \in [0,1]$.
    - Si $p(x',x) > r$, l'inversion de spin proposée doit être acceptée. Modifier $ketx \rightarrow |x'\rangle$.
    - Si $p(x',x) \leq r$, n'acceptez pas le mouvement.
3. À la fin de la boucle interne, calculez les observables d'intérêt et écrivez-les dans un fichier de sortie.

Ce qui précède décrit les principales étapes d'une simulation VMC. L'analyse d'erreur des observables locaux est effectuée à la fin de la simulation. Par exemple, la figure 8.1 montre une

exécution de Monte Carlo typique sur le réseau triangulaire, affichant l'énergie par site et les barres d'erreur en fonction du nombre d'étapes de Monte Carlo N_{MC}. Comme le montre l'encadré, l'erreur diminue comme $1/\sqrt{N_{MC}}$.

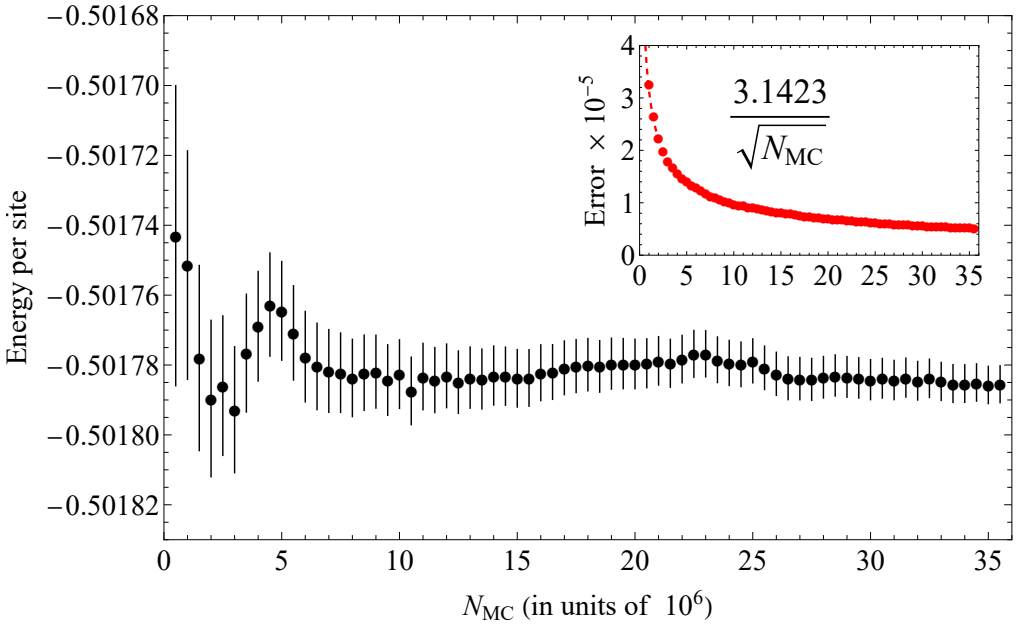

Figure 8.1: Energie par site pour le liquide de spin de Dirac à réseau triangulaire 6×6 (défini plus loin dans la section 8.4) en fonction du nombre de pas de Monte Carlo N_{MC}. Dans l'encadré, nous montrons la tendance de l'écart-type (avec le même axe x), qui affiche clairement un comportement de $1\sqrt{N_{MC}}$.

Quelques remarques supplémentaires sont énumérées ci-dessous :

- Le projecteur de Gutzwiller est respecté en n'échantillonnant que les $|x\rangle$ ayant un spin sur chaque site. Les inversions de spin proposées sur la chaîne de Markov ne nous font manifestement pas sortir de ce secteur.

- Les simulations VMC sont "embarrassingly parallelizable". Pour calculer les observables, plusieurs chaînes de Markov peuvent être exécutées en parallèle sur différents ordinateurs, chacun avec une graine de nombres aléatoires différente, sans qu'il soit nécessaire de communiquer entre eux.

Ceci termine notre discussion sur la méthode VMC. Dans la section 8.3, nous utilisons cette méthode pour calculer les chevauchements de fonctions d'onde et la dégénérescence topologique d'un liquide de spin chiral sur un tore. Dans la section 8.4, nous construisons diverses excitations à basse énergie de liquides de spin de Dirac et étudions leur énergie variationnelle.

8.2 Réseaux de tenseurs

Dans cette section, nous donnerons une brève introduction aux idées centrales des réseaux de tenseurs (TN) en une et deux dimensions. Les réseaux de tenseurs sont un cadre mathématique puissant utilisé pour représenter efficacement une certaine classe d'états quantiques à plusieurs corps et étudier leurs propriétés. Alors que les méthodes TN sont devenues des outils précieux en physique de la matière condensée, elles ont également trouvé des applications profondes dans divers domaines comme les réseaux neuronaux [105], les théories de jauge sur réseau [106] et la gravité quantique [107]. L'une des caractéristiques les plus convaincantes des réseaux de tenseurs est leur capacité à afficher explicitement et intuitivement la structure d'intrication des états quantiques. Bien qu'ils soient limités par la quantité d'intrication qu'ils peuvent capturer, ces limitations ne nous empêchent pas d'étudier les états qui nous intéressent le plus : les états fondamentaux et les excitations à basse énergie des hamiltoniens locaux.

Les réseaux tensoriels unidimensionnels, connus sous le nom d'États de produits matriciels (MPS), sont étroitement liés à la technique du groupe de renormalisation de matrice de densité (DMRG) [108, 109] qui est devenue la référence absolue pour l'étude des systèmes quantiques 1D en raison de son efficacité et de sa large applicabilité.

Les États de paires intriquées projetées (PEPS) étendent le formalisme MPS à deux dimensions et au-delà [110, 111]. Bien que le calcul des observables soit beaucoup plus difficile qu'en une dimension, les PEPS ont néanmoins été très efficaces dans l'étude des systèmes quantiques 2D.

Dans cette section, nous discuterons de certaines idées principales des MPS et des PEPS, et de la manière dont elles sont utilisées pour étudier les modèles en treillis. La discussion ici est fortement inspirée des sources [116–118], et nous dirigeons le lecteur vers celles-ci pour plus de détails.

Dans les réseaux de tenseurs, les états quantiques (et les opérateurs) sont représentés à l'aide de diagrammes tensoriels. Le nombre de branches (lignes attachées au tenseur) indique le nombre d'indices libres. Quelques exemples sont présentés dans la figure 8.2.

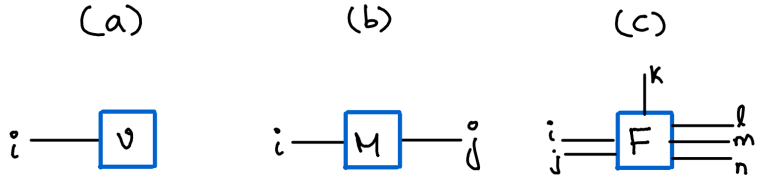

Figure 8.2: Représentation picturale de (a) un vecteur $\vec{v}$, (b) une matrice M et (c) un tenseur F_{ijklmn}.

Lorsque deux tenseurs sont combinés, les branches qui les relient sont additionnées. De cette manière, des opérations mathématiques complexes impliquant de nombreux tenseurs peuvent

être facilement visualisées à l'aide de diagrammes TN (figure 8.3).

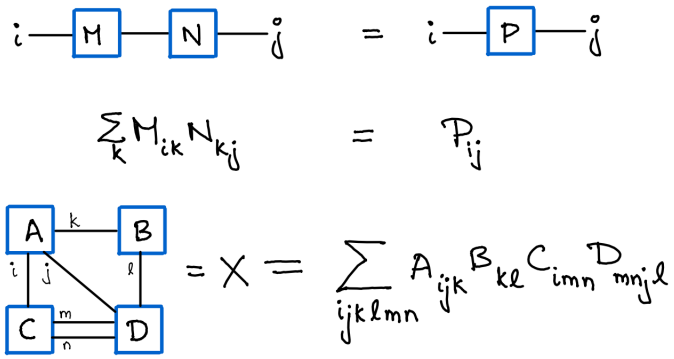

Figure 8.3: Exemples de contraction tensorielle

8.2.1 États de produits matriciels (MPS) et États de paires intriquées projetées (PEPS)

Considérons un système en treillis de N sites, où chaque site possède un espace de Hilbert local de dimension p, $\mathscr{H} = \mathbb{C}^p$ avec les états $|0\rangle, |1\rangle, \ldots |p-1\rangle$. Alors, un état quantique générique dans l'espace de Hilbert à plusieurs corps de N particules peut s'écrire comme

$$|\Psi\rangle = \sum C_{i_1,i_2,\ldots i_N} |i_1\rangle \otimes |i_2\rangle \otimes \ldots \otimes |i_N\rangle \tag{8.15}$$

Ainsi, le nombre de paramètres (coefficients C) requis pour spécifier l'état est p^N, exponentiel en nombre de sites. Pour les grands systèmes, on ne peut même pas stocker tous ces coefficients. De plus, la nature de l'intrication dans l'état $|\Psi\rangle$ n'est pas du tout apparente à partir des coefficients.

Cependant, les TN ont une structure différente (voir les figures 8.4 et 8.5). Dans les TN, chaque site du réseau est associé à un tenseur, et ces tenseurs sont interconnectés par des degrés de liberté « virtuels ». Le nombre total de paramètres nécessaires pour décrire l'état évolue linéairement avec le nombre de sites, en particulier $O(NpD^2)$ pour les États de Produits de Matrices (MPS) et $O(NpD^4)$ pour les États de Paires Intriquées Projetées (PEPS) sur un réseau carré [1]. Le paramètre supplémentaire D est une constante connue sous le nom de dimension de liaison, et il caractérise le réseau tensoriel (p est généralement appelé la dimension physique, et D la dimension virtuelle). Si $D = 1$, le TN est simplement un produit de pièces déconnectées pour chaque site, et représente donc un état produit. On voit que les liaisons virtuelles sont porteuses d'intrication ; plus la dimension de la liaison est grande, plus l'intrication qui peut être capturée par l'état est grande.

[1] Si nous considérons un TN avec invariance translationnelle, alors le nombre de paramètres n'évolue pas du tout avec la taille du système.

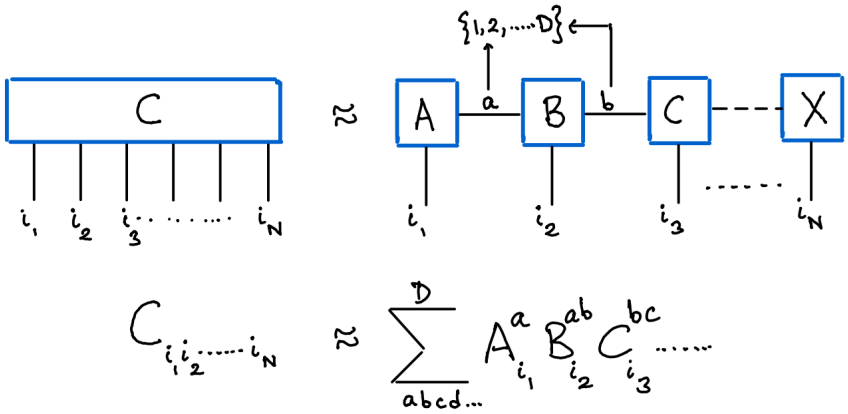

Figure 8.4: Exprimer la fonction d'onde à plusieurs corps sous forme de MPS.

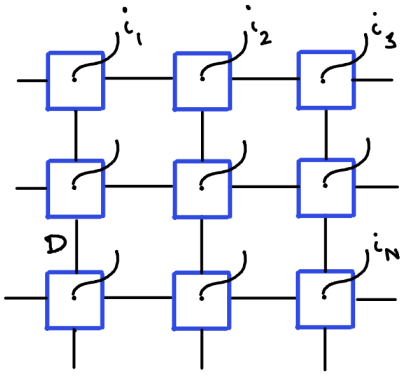

Figure 8.5: Une ansatz générale du PEPS. Les lignes courbes représentent les indices physiques sortant du plan.

À première vue, cette approximation de réduction exponentielle du nombre de paramètres semble très sévère, et ne devrait pas être valide/assez bonne pour représenter le $|\Psi\rangle$ général [2]. Le hic cependant, c'est que les états fondamentaux des hamiltoniens locaux sont *très* différents des états quantiques génériques dans l'espace de Hilbert à plusieurs corps. Les premiers satisfont la loi dite de l'aire d'intrication, qui stipule que l'entropie d'intrication de la matrice de densité réduite d'une région R du réseau évolue comme la frontière de la région ; $S(R) \sim \partial R$. Les états généraux se comporteraient plutôt selon une loi de volume $S(R) \sim R$, l'intrication d'une région évoluerait comme le volume de la région. Cette loi d'aire a été rigoureusement prouvée pour les systèmes 1D gapped [121] (où elle est une constante asymtotiquement), et on pense qu'elle est également valable pour les dimensions supérieures (voir [122] pour plus de détails). En fait, non seulement l'état fondamental, mais la plupart des états *physiques* obtenus grâce à l'évolution temporelle des hamiltoniens locaux pour le temps polynomial obéissent à la loi d'aire. En ce sens, la physique essentielle au monde réel des systèmes quantiques à plusieurs corps se déroule dans un coin exponentiellement petit de l'espace de Hilbert [123]. Heureusement, il s'avère que

[2] À moins que D lui-même ne soit exponentiel dans N.

c'est précisément ce coin de l'espace de Hilbert que MPS et PEPS ciblent et peuvent représenter efficacement.

Similairement à la méthode VMC, les réseaux de tenseurs peuvent également être utilisés pour représenter des fonctions d'onde variationnelles qui se rapprochent des états fondamentaux des hamiltoniens à plusieurs corps. Les paramètres des tenseurs peuvent être optimisés de manière variationnelle pour se rapprocher de l'état fondamental du système.

Dans la section suivante, nous allons explorer comment les observables, telles que l'énergie variationnelle, peuvent être calculées dans ce cadre. Notons au passage que des états hautement non triviaux peuvent être capturés dans le formalisme du réseau tensoriel en utilisant déjà de faibles valeurs de D. Par exemple, l'état fondamental du code torique peut être exactement écrit comme un PEPS 2D avec $D = 2$ [124], et l'état liquide de spin RVB peut être exactement représenté avec $D = 3$ [125].

8.2.2 Calcul des observables

Pour calculer la valeur attendue d'un opérateur local $\langle\Psi|\hat{O}|\Psi\rangle$ (par exemple, un opérateur agissant sur un seul site comme la magnétisation), nous prenons l'opérateur en sandwich entre l'état et sa version réfléchie (qui représente le conjugué), puis nous contractons le réseau des vecteurs de limite gauche et droite vers le site de l'opérateur.

Dans le cas 1D, de tels calculs peuvent être effectués efficacement, c'est-à-dire avec une mise à l'échelle polynomiale du nombre de sites. De plus, il existe une liberté de jauge dans la façon dont nous définissons nos tenseurs; on peut multiplier une identité XX^{-1} entre deux tenseurs et cela ne change pas l'état. Par conséquent, une infinité de réseaux de tenseurs décrivent le même état physique. Cette liberté de jauge peut être exploitée en 1 dimension pour calculer des observables de manière extrêmement efficace et élégante. On choisit une jauge dite de forme canonique, où les tenseurs MPS sont orthonormalisés dans le sens où les tenseurs à gauche et à droite d'un site spécifique satisfont certaines conditions d'orthogonalité. En deux dimensions, le calcul des observables ne peut pas être effectué efficacement et le coût de calcul augmente de manière exponentielle avec la taille du système. De plus, la forme canonique mentionnée ci-dessus n'existe pas en général pour PEPS. Par conséquent, différents schémas d'approximation sont utilisés pour calculer les observables. La méthode utilisée dans cette thèse est connue sous le nom de Corner Transfer Matrix Renormalization Group (CTMRG), et elle est brièvement décrite ci-dessous.

Supposons que nous souhaitons calculer une valeur d'espérance mathématique d'un observable local $\hat{O}$ sur un site. Nous définissons d'abord les tenseurs C_i, T_i, $i = 1 \ldots 4$ qui décrivent l'environnement autour du site d'intérêt (voir figure 8.6). Comme ces tenseurs d'environnement ne peuvent pas être contractés exactement en raison du coût exponentiel, nous introduisons un paramètre connu sous le nom de dimension de liaison d'environnement χ, qui dicte le rang maximal des tenseurs d'environnement. Il est clair que χ contrôle l'intrication du site central avec l'environnement. Prendre la limite $\chi \to \infty$ donnerait le résultat exact.

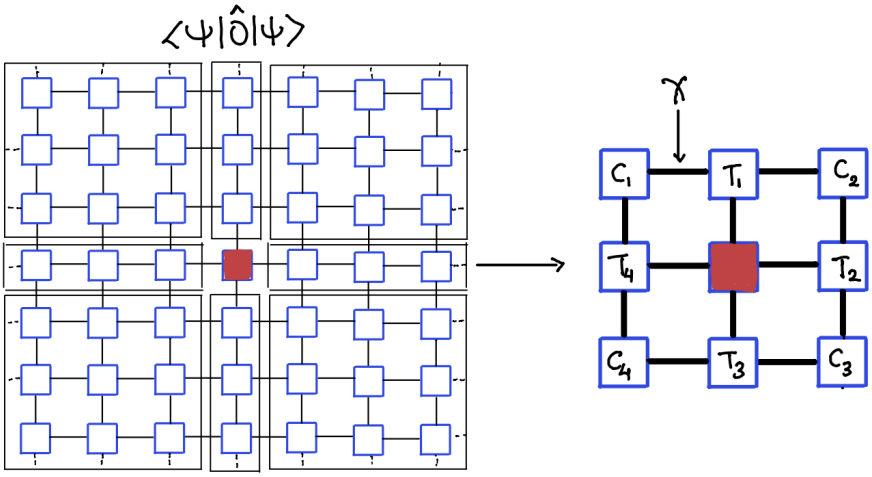

Figure 8.6: Définition des tenseurs d'environnement C et T pour la contraction d'un réseau tensoriel 2D infini. La contraction est approximée par la dimension de liaison d'environnement χ.

La méthode CTMRG consiste à affiner de manière itérative les tenseurs d'environnement $\{C, T\}$ en laissant le système croître dans toutes les directions et en les renormalisant. Dans la figure 8.7, nous décrivons un "déplacement vers la gauche", où le système est agrandi en dupliquant une colonne de tenseurs C et T à gauche du site d'intérêt. Ensuite, ceux-ci sont absorbés dans les tenseurs existants, ce qui augmente la dimension de liaison. Enfin, nous effectuons une décomposition en valeurs singulières (SVD) et tronquons la dimension de liaison à χ. Des déplacements identiques dans les quatre directions sont effectués, et cette procédure est répétée plusieurs fois, jusqu'à ce que la convergence soit atteinte ; on vérifie généralement que les spectres des tenseurs d'environnement ne changent plus sensiblement. Enfin, une analyse d'échelle systématique des observables est effectuée en fonction à la fois de χ et de D.

8.3 VMC pour PEPS fermionique

8.3.1 Motivation et contexte

Les CSL sont des états exotiques de la matière caractérisés par l'absence d'ordre magnétique tout en brisant les symétries de renversement temporel (T) et de parité (P) [144]. Ils présentent également un ordre topologique à longue portée [145]. Des efforts expérimentaux pour identifier les composés avec des états fondamentaux CSL sont en cours, avec une attention particulière accordée aux matériaux couplés spin-orbite avec une interaction de type Kitaev sous des champs magnétiques externes [2, 56, 57]. Ils ont également été proposés dans des plates-formes à atomes froids en utilisant la commande Floquet [65] (voir aussi [66]) ou des réseaux Rydberg [67–70] où la chiralité des modes de bord peut être détectée expérimentalement. Les CSL émergent généralement dans des systèmes fortement corrélés, des outils numériques permettant de déterminer les diagrammes de phase des hamiltoniens génériques et de caractériser les

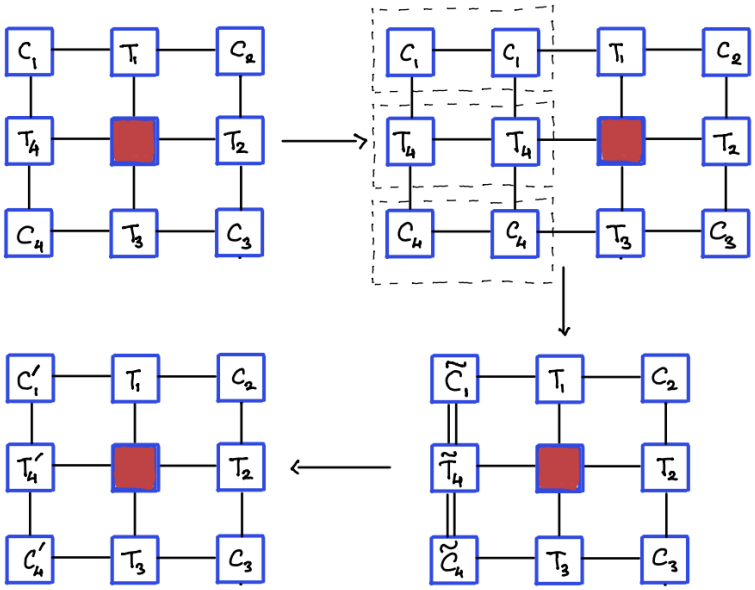

Figure 8.7: Réalisation d'un "déplacement vers la gauche" pour renormaliser les tenseurs C et T à gauche du site central. Tout d'abord, une colonne supplémentaire est insérée, suivie d'une absorption de la colonne à gauche, et enfin d'une renormalisation où les dimensions de liaison de l'environnement sont ramenées à leur valeur d'origine χ.

CSL sont souhaités. Les réseaux tensoriels tels que les états de paires enchevêtrées projetées (PEPS) [110] sont bien adaptés à l'étude des liquides de spin. De plus, les formes chirales de PEPS peuvent décrire les CSL [183, 184] et être utilisées comme un schéma variationnel efficace pour attaquer les modèles de spin quantiques frustrés hébergeant des phases CSL [185, 186]. Malgré les succès et les points forts mentionnés ci-dessus du cadre PEPS, il est resté difficile de déterminer complètement si les PEPS bosoniques classiques peuvent vraiment décrire les CSL. En particulier, il n'est toujours pas clair si l'obstruction topologique affecte les propriétés topologiques globales comme la dégénérescence topologique GS ou le comptage correct de la théorie conforme des champs (CFT) dans le spectre d'intrication (ES). Pour le cas non chiral, PEPS est considéré comme un bon ansatz conceptuellement, l'ordre topologique étant codé par la symétrie de jauge [115, 263]. En revanche, la question de savoir si les PEPS chiraux donnent la dégénérescence topologique correcte du CSL n'est pas encore tranchée en général en raison du coût de calcul élevé [183].

Dans notre travail, basé sur l'ansatz PEPS fermionique projeté (fPEPS) récemment proposé, nous montrons, en utilisant des techniques VMC, que PEPS peut représenter des CSL avec une dégénérescence topologique correcte. En utilisant cet ansatz fPEPS comme état initial, nous effectuons en outre une optimisation variationnelle pour attaquer un modèle de réseau carré $J_1 - J_2 - J_\chi$ frustré [188] dans le régime du liquide de spin chiral [185, 189, 190]. L'approche fPEPS a une énergie compétitive par rapport au PEPS bosonique conventionnel et montre de manière cruciale une dégénérescence correcte du spectre d'intrication.

Afin de construire un CSL simple, nous considérons d'abord un état isolant de Chern avec $C = 1$, obtenu en diagonalisant l'hamiltonien de Hofstadter (électron libre) suivant sur le réseau carré

$$H = \sum_{\langle ij\rangle,\sigma} t_1 \chi_{ij} c^\dagger_{i\sigma} c_{j\sigma} + \sum_{\langle\langle ik\rangle\rangle,\sigma} t_2 c^\dagger_{i\sigma} c_{k\sigma} e^{i\theta_{ik}} + \text{h.c.} \tag{8.16}$$

où $\langle ij\rangle$ ($\langle\langle ik\rangle\rangle$) désigne les liaisons voisines les plus proches (prochaines plus proches) et σ est l'indice de spin, $\sigma = \{\uparrow, \downarrow\}$. Les sauts sont identiques pour les deux espèces de spin. Nous fixons $t_2 = 0{,}5t_1$, $\chi_{ij} = \pm 1$ pour assurer un flux π à travers chaque plaquette carrée et choisissons les phases complexes θ_{ik} pour obtenir un flux $\pi/2$ dans tous les triangles. Nous choisissons la jauge (utilisée dans la réf. [219]) telle que la maille unitaire contienne deux sites voisins les plus proches le long de la direction x. La fonction d'onde de spin à plusieurs corps exacte $|\varphi\rangle$ est un déterminant de Slater projeté de Gutzwiller

$$|\varphi\rangle = P_G \prod_\alpha c^\dagger_{\alpha,\uparrow} c^\dagger_{\alpha,\downarrow} |0\rangle, \tag{8.17}$$

où le projecteur de Gutwiller $\prod_i (n_{i,\uparrow} - n_{i,\downarrow})^2$ se projette sur le sous-espace d'exactement un électron par site, et $c^\dagger_{\alpha,\sigma}$ correspond aux états de particules individuelles obtenus à partir de l'équation hamiltonienne de champ moyen (8.16). Pour les fPEPS gaussiennes, l'ensemble des orbitales $c^\dagger_{\alpha,\sigma}$ n'est représenté qu'approximativement en raison de la troncature de la dimension de liaison finie.

Il est connu que l'état de parton exact résultant est un CSL $SU(2)_1$ qui est équivalent à l'état bosonique de Laughlin $\nu = 1/2$. Sur un tore, ce CSL présente une dégénérescence topologique double où les états dégénérés peuvent être construits en imposant différentes conditions aux limites sur les fonctions d'onde des partons [220]. Sur un cylindre, le CSL héberge des états de bord sans gap chiraux prédits par la CFT $SU(2)_1$ de Wess-Zumino-Witten (WZW).

Français Pour construire l'état fPEPS gaussien qui est une approximation de l'état fondamental exact de l'équation (8.16), nous adoptons la méthode introduite dans les références [222, 223]. L'ansatz à plusieurs corps invariant par translation est paramétré par un seul tenseur gaussien avec quatre indices virtuels et deux indices physiques correspondant à la cellule unitaire dans le modèle de Hofstadter. Dans le tenseur gaussien, la dimension de l'espace virtuel est définie par le nombre de modes virtuels M. Chaque mode de fermion virtuel peut être occupé ou inoccupé, ainsi la dimension de liaison devient $D = 2^M$ pour un état sans spin et $D = 4^M$ pour un état $SU(2)$ spineux. Pour obtenir la meilleure approximation du tenseur fPEPS gaussien, nous utilisons l'optimisation du gradient et choisissons l'énergie (électron libre) de l'équation. (8.16) à mi-remplissage comme fonction de coût.

Comme l'état fPEPS non projeté est gaussien, il peut également être écrit comme un déterminant de Slater (état produit) sur tout tore fini et toutes les propriétés physiques peuvent être extraites exactement. Dans la réf. [219], il a été montré que le fPEPS non projeté devient chiral à partir de $M \geq 2$, et les fonctions de corrélation s'améliorent quantitativement avec

l'augmentation de M. Cependant, les propriétés topologiques générales du fPEPS restent floues après la projection de Gutzwiller, et ne sont pas accessibles (à l'exception du spectre d'intrication) par les techniques PEPS conventionnelles. Par conséquent, nous utilisons VMC pour calculer la dégénérescence topologique et la fidélité des états fPEPS.

8.3.2 Résultats

Nous calculons d'abord le chevauchement normalisé entre le CSL exact projeté et les états fPEPS avec conditions aux limites périodiques (PBC-PBC), donné par

$$O_M = \frac{|\langle \Psi_{\text{exact}} | \Psi_M \rangle|}{\sqrt{\langle \Psi_{\text{exact}} | \Psi_{\text{exact}} \rangle \langle \Psi_M | \Psi_M \rangle}}. \tag{8.18}$$

Nous pouvons ensuite définir la fidélité par unité de surface (énergie libre) $f = (O_M)^{1/L^2}$, qui devrait montrer une faible dépendance de taille et converger vers une valeur finie dans la limite $L \to \infty$. L'infidélité $1-f$ tracée dans la figure 8.8 confirme ces attentes. De plus, la diminution de l'infidélité avec l'augmentation de M démontre clairement l'amélioration de la précision des états fPEPS optimisés. Nous notons que des résultats similaires ont été obtenus pour les trois autres choix de conditions limites, c'est-à-dire PBC-APBC, APBC-PBC et APBC-APBC.

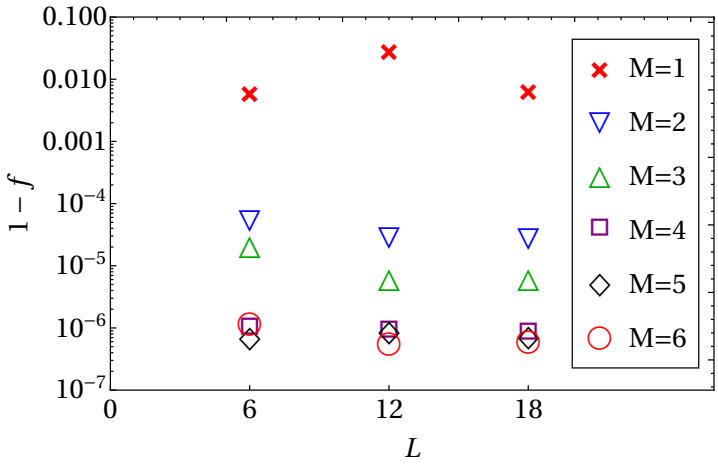

Figure 8.8: Infidélité $1-f$ représentée en échelle logarithmique en fonction de la taille du système L pour les états fPEPS avec $M = 1 \ldots 6$ et des conditions limites périodiques. Les barres d'erreur estimées sont plus petites que la taille des symboles.

Pour confirmer que les fPEPS projetés décrivent les propriétés physiques correctes du CSL, nous calculons les corrélations spin-spin dans l'espace réel pour le système $L = 18$. Celles-ci sont présentées dans la figure 8.9. Nous observons un comportement exponentiel à courte distance comme prévu pour un état gappé, avec une longueur de corrélation très courte $\xi \approx 0,57$. De plus, les états fPEPS (pour toutes les valeurs de M) sont essentiellement indiscernables du CSL exact en termes de corrélations.

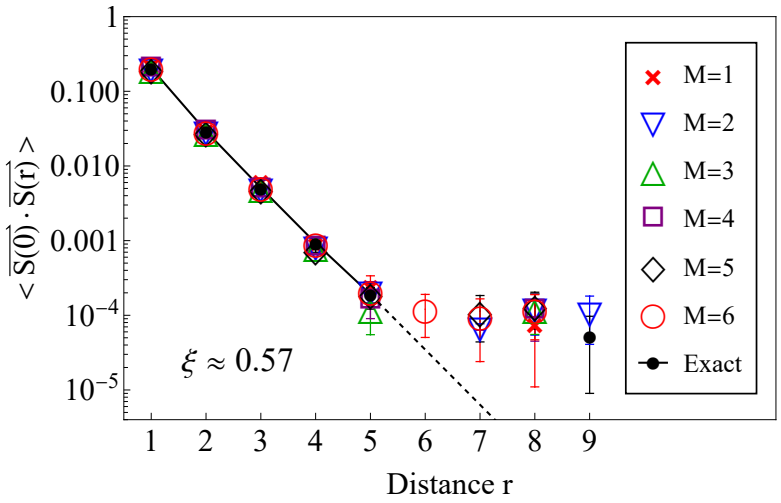

Figure 8.9: Graphique logarithmique de la grandeur des corrélations spin-spin en fonction de la distance pour les fPEPS exactes et projetées, pour le cluster $L = 18$ avec des conditions aux limites périodiques. Les symboles sont omis si la valeur obtenue est inférieure à un écart type d'erreur. Les corrélations attendues du CSL exact à $r > 5$ (dans la limite thermodynamique) sont représentées par une ligne pointillée, prolongeant le comportement exponentiel.

Nous arrivons maintenant au résultat principal de notre travail, qui est la dégénérescence topologique des états fPEPS sur un tore. Une caractéristique fondamentale d'une phase ordonnée topologique est une dégénérescence de l'état fondamental qui dépend de la topologie de l'espace [230]. Comme mentionné précédemment, l'état exact $SU(2)_1$ CSL (8.17) a une double dégénérescence sur un tore : l'imposition de conditions limites différentes sur l'ansatz parton avant la projection produit des états dégénérés qui ne peuvent pas être distingués par des observables locaux (comme les corrélations spin-spin) après projection. Dans la limite thermodynamique, on sait que les quatre états ne couvrent qu'un espace linéaire bidimensionnel [220].

Pour étudier cette propriété des fPEPS et des états exacts sur des amas finis, nous calculons la matrice de recouvrement 4×4 O avec les éléments

$$O_{\alpha,\beta} = \frac{\langle \Psi_M^\beta | \Psi_M^\alpha \rangle}{\sqrt{\langle \Psi_M^\alpha | \Psi_M^\alpha \rangle \langle \Psi_M^\beta | \Psi_M^\beta \rangle}} \tag{8.19}$$

où α et β désignent les quatre choix de conditions aux limites sur le tore. Le rang de cette matrice hermitienne (qui désigne le nombre de vecteurs propres linéairement indépendants) est le nombre de valeurs propres non nulles. Dans la limite thermodynamique, les valeurs propres de l'état exact doivent converger vers $\{+2, +2, 0, 0\}$ (la trace de la matrice étant 4). Dans la figure 8.10, nous traçons les valeurs propres pour les états fPEPS projetés et exacts en fonction de L. De manière remarquable, nous observons que pour *fixe* $M > 1$, les valeurs propres convergent vers le résultat exact avec l'augmentation de la taille du système (déjà à $L = 18$, l'écart est au plus de 10^{-3}).

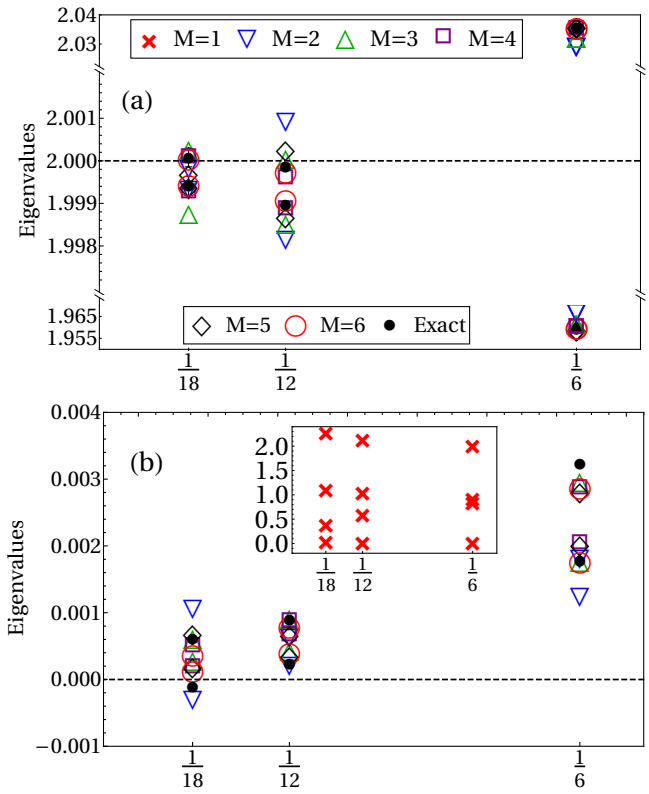

Figure 8.10: Valeurs propres de la matrice de recouvrement en fonction de la taille inverse du système $1/L$ pour les états exact et fPEPS. Les paires de valeurs propres convergent vers +2 et 0 dans (a) et (b), respectivement. Les données $M = 1$ sont présentées dans l'encart car elles présentent un écart beaucoup plus grand que les autres états fPEPS. Les barres d'erreur estimées ont approximativement la taille des symboles.

Ces résultats confirment que le fPEPS, même à des dimensions de liaison finies, peut capturer avec précision la dégénérescence topologique correcte des états CSL. Cependant, dans le but d'étudier les modèles de spin frustrés, l'ansatz partonique conventionnel n'a qu'un nombre limité de paramètres variationnels tels que les coefficients de saut, les facteurs de Jastrow, etc. Au contraire, le PEPS peut représenter des états d'interaction génériques avec l'augmentation systématique de la dimension de liaison. On peut se poser la question : notre ansatz fPEPS peut-il être utilisé pour étudier les modèles de spin avec les états fondamentaux CSL ? Et si les propriétés topologiques du fPEPS restent robustes après optimisation variationnelle ?

Pour répondre à ces questions, nous effectuons une étude PEPS variationnelle sur le modèle chiral $J_1 - J_2 - J_\chi$ en utilisant le projet GfPEPS (discuté dans la section précédente) comme ansatz initial. L'hamiltonien spin-1/2 est donné par

$$\mathscr{H} = J_1 \sum_{\langle i,j\rangle} S_i \cdot S_j + J_2 \sum_{\langle\langle i,k\rangle\rangle} S_i \cdot S_k + J_\chi \sum_{\triangle_{ijk}} \left(S_i \times S_j\right) \cdot S_k. \tag{8.20}$$

Nous choisissons les paramètres du modèle de spin comme $J_1 = 2\cos(0.06\pi)\cos(0.14\pi)$, $J_2 =$

$2\cos(0.06\pi)\sin(0.14\pi)$, $J_\chi = 4\sin(0.06\pi)$ qui a été considéré dans les références. [185, 188, 212] et est connu pour être profondément à l'intérieur de la phase CSL avec l'énergie de l'état fondamental étant $E \approx -1$. Nous importons la méthode iPEPS bosonique $SU(2)$ dans celle-ci et calculons les énergies variationnelles comme référence. Pour l'iPEPS bosonique, le tenseur a une symétrie $SU(2)$ et la taille de la cellule unitaire est choisie de telle sorte que chaque tenseur n'ait qu'une seule branche physique. Les résultats pour les espaces virtuels $V = 0 \oplus 1/2$ ($D = 3$) et $V = 0 \oplus 0 \oplus 1/2$ ($D = 4$) sont donnés dans la Fig. 8.11. En extrapolant à la limite infinie χ, les énergies sont d'environ $-0,99$.

Dans notre traitement fPEPS, l'état partonique initial est toujours choisi au paramètre de saut $t_1 = 2t_2$ qui correspond à la plus grande bande interdite. Nous prenons $M = 2$ ($D = 16$) GfPEPS avec projection de Gutzwiller et calculons l'énergie par rapport au modèle de spin. Comme on peut le voir dans la Fig. 8.11, l'état partonique non optimisé a déjà une bonne énergie proche de l'iPEPS bosonique optimisé à $D = 3,4$. Après optimisation des éléments tensoriels fPEPS, l'énergie s'améliore encore jusqu'à $E \approx -0,995$.

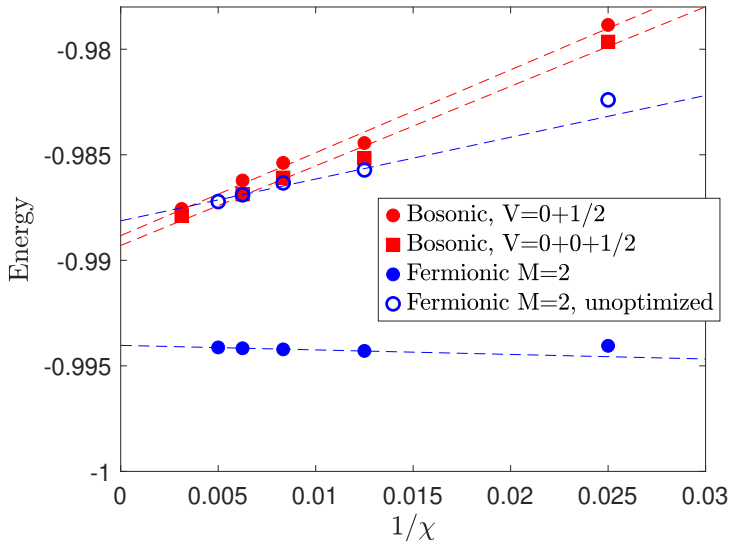

Figure 8.11: Énergie variationnelle des iPEPS bosoniques optimisés (rouge) et des iPEPS fermioniques projetés (bleu) pour le modèle de spin. Les cercles ouverts bleus montrent l'énergie de l'ansatz partonique fermionique à $t_1 = 1, t_2 = 0,5$ sans optimisation variationnelle des éléments tensoriels.

Nous étudions ensuite le spectre d'intrication des tenseurs optimisés. Pour analyser le comptage de niveaux du spectre d'intrication, nous plaçons notre tenseur optimisé sur un cylindre de largeur finie et calculons le spectre d'intrication d'un tel état invariant en translation. Pour calculer le spectre d'intrication, l'Hamiltonien de bord (points fixes de la matrice de transfert) peut être construit exactement par contraction exacte [128] ou approximativement en regroupant les tenseurs T de l'environnement CTMRG [184]. Les figures 8.12 (a)-(b) montrent le spectre

d'intrication des iPEPS fermioniques $M = 2$ optimisés calculés à partir de CTMRG avec une dimension de liaison environnementale $\chi = 110$. Le spectre de basse énergie montre des multiplets SU(2) avec comptage $0, 1, 0+1, 0+1+1, \ldots$, dans le secteur de spin entier et $1/2, 1/2, 1/2+3/2, \ldots$, dans le secteur de spin demi-entier, satisfaisant les prédictions de $SU(2)_1$ WZW CFT. Notez que dans les secteurs pair et impair, il n'y a qu'une seule branche chirale de basse énergie, cohérente avec les résultats récents de DMRG sur les cylindres finis [189, 190]. En revanche, les figures 8.12 (c)-(d) montrent le spectre d'intrication des iPEPS bosoniques $D = 3$. Ici, le comptage de niveaux est correct, mais une branche identique apparaît anormalement dans le secteur impair avec un décalage d'impulsion π. Nous avons également confirmé que la branche redondante ne peut pas être éliminée ou décalée en modifiant la dimension de liaison de l'iPEPS bosonique.

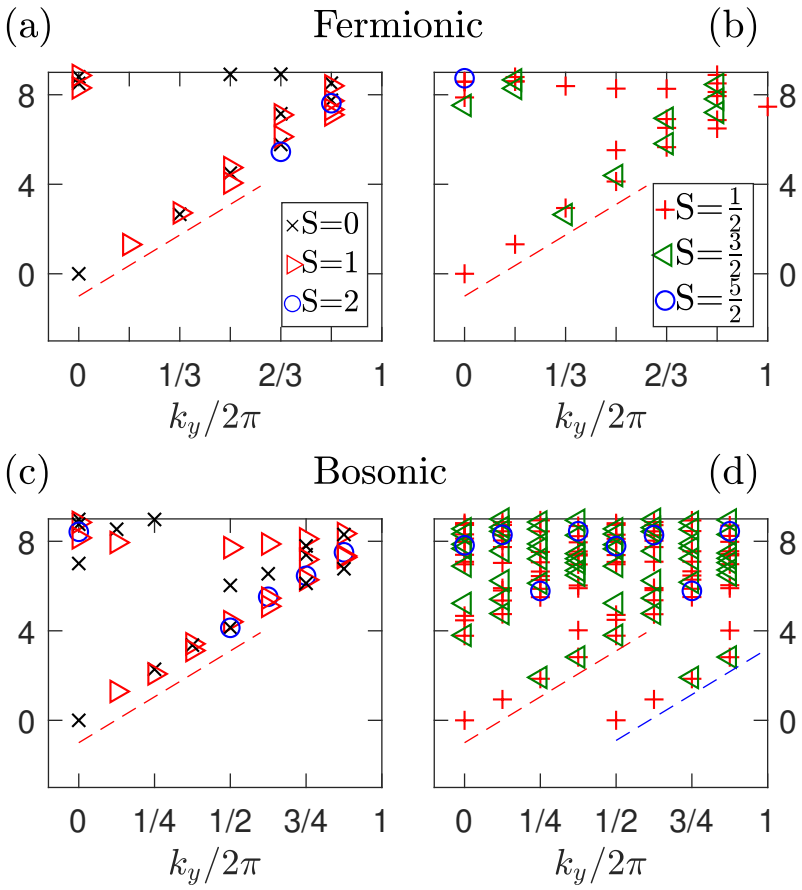

Figure 8.12: Spectre d'intrication des iPEPS fermioniques projetés $M = 2$ optimisés (en haut) et des iPEPS bosoniques $D = 3$ (en bas) pour le modèle de spin sur des cylindres de largeur finie 6 et 8, respectivement. Les colonnes de gauche et de droite correspondent aux secteurs pairs (spin entier) et impairs (spin demi-entier). Les lignes pointillées rouges indiquent les dispersions linéaires théoriquement prédites de la tour d'états, tandis que la ligne pointillée bleue indique la branche redondante dans le secteur impair des iPEPS bosoniques.

8.3.3 Conclusion

Les méthodes de réseaux de tenseurs ont été largement appliquées pour étudier les modèles de spin frustrés hébergeant d'éventuelles phases liquides de spin. Cependant, en raison d'un théorème de "no-go" [210], des doutes ont surgi quant à leur capacité à décrire les états chiraux. Dans ce chapitre, nous avons étudié les propriétés topologiques de l'ansatz PEPS fermionique projeté pour un état CSL. En effectuant une analyse VMC sur l'état parton initial (projeté par Gutzwiller), nous avons démontré que le fPEPS à liaison finie peut capturer avec précision la dégénérescence topologique de l'état fondamental CSL sur un tore. Cette réalisation a été difficile avec le PEPS bosonique classique en raison du coût de calcul élevé impliqué [183]. De plus, nos résultats montrent que l'ansatz fPEPS capture efficacement les fonctions de corrélation spin-spin du CSL. De plus, les ansatze fPEPS non gaussiens ont été optimisés variationnellement pour le modèle de Heisenberg $J_1 - J_2 - J_\chi$ et se sont avérés avoir une énergie compétitive par rapport à leurs homologues bosoniques. De plus, les iPEPS fermioniques optimisés ont conservé le comptage de niveau correct du spectre d'intrication contrairement aux iPEPS bosoniques qui ont une branche dupliquée dans le secteur topologique impair (sémion).

Notre travail fournit des preuves supplémentaires soutenant l'utilisation des méthodes PEPS pour décrire les états topologiquement ordonnés chiraux, complétant les études précédentes dans cette direction [185–187, 211, 217, 219].

8.4 Monopôles dans les liquides de spin de Dirac

Dans cette section, nous discutons de l'autre projet de cette thèse, où nous essayons de comprendre les excitations à basse énergie des liquides de spin de Dirac sans gap.

Les liquides de spin peuvent être avec gap ou sans gap. Les liquides de spin avec gap sont comparativement mieux compris et hébergent généralement des excitations fractionnaires déconfinées. Par exemple, le code torique, une théorie de jauge sur réseau $\mathbb{Z}_2$, est exactement soluble et possède un état fondamental QSL avec gap. Ses excitations à basse énergie sont des anyons qui obéissent à des statistiques fractionnaires mutuelles.

En revanche, les liquides de spin sans gap sont moins bien compris, en particulier en deux dimensions. Il n'existe pas de modèle exactement soluble pour ces états, et il n'est pas clair si les traitements de champ moyen survivent aux fluctuations de jauge. Spécifiquement pour les liquides de spin de Dirac, la théorie à basse énergie est QED_3 dont la physique implique des spinons (fermions de Dirac sans masse) couplés à un champ de jauge $U(1)$. La théorie des basses énergies héberge des monopôles et des photons comme excitations de jauge. La compréhension de cette physique des basses énergies est essentielle pour répondre aux questions clés de la DSL, telles que sa stabilité en tant que phase et ses signatures expérimentales.

Dans notre travail, nous construisons explicitement des fonctions d'onde variationnelles correspondant aux excitations des monopôles et étudions leurs propriétés dans le contexte des

modèles de Heisenberg sur les réseaux triangulaire et Kagome. De manière cruciale, nous calculons les moments et l'énergétique des monopôles après la projection de Gutzwiller, allant au-delà de l'approximation du champ moyen. Ce faisant, nous pouvons également commenter la stabilité énergétique de l'état DSL par rapport à (un type de) perturbation qui brise la symétrie de renversement du temps (conduisant à un liquide de spin chiral).

Nos résultats fournissent des preuves supplémentaires de l'état fondamental DSL des modèles (8.25), et confirment également que les prédictions de la théorie des champs pour les nombres quantiques des monopôles sont valables après la projection de Gutzwiller.

Dans les sections suivantes, nous définissons les états liquide de spin de Dirac et monopôle, et résumons nos résultats sur leur énergétique et leurs impulsions.

8.4.1 Fonctions d'onde variationnelles

Les fonctions d'onde variationnelles pour l'état de Dirac sont données par

$$|\Psi\rangle = \mathscr{P}_G|\Phi_0\rangle, \tag{8.21}$$

où $|\Phi_0\rangle$ est l'état fondamental de l'hamiltonien auxiliaire (sans interaction) :

$$\mathscr{H}_0 = \sum_{\langle i,j\rangle,\sigma} \chi^0_{i,j} c^\dagger_{i,\sigma} c_{j,\sigma} + \text{h.c.}, \tag{8.22}$$

où $c^\dagger_{i,\sigma}$ ($c^\dagger_{i,\sigma}$) crée (détruit) un fermion sur le site i de spin $\sigma = \uparrow, \downarrow$; $\chi^0_{i,j}$ définit l'amplitude de saut pour les sites les plus proches voisins (i,j). Pour l'état de Dirac, il prend les valeurs $\chi^0_{i,j} = \pm 1$ et la distribution de ces liaisons dans le réseau est montrée dans la figure 8.13.

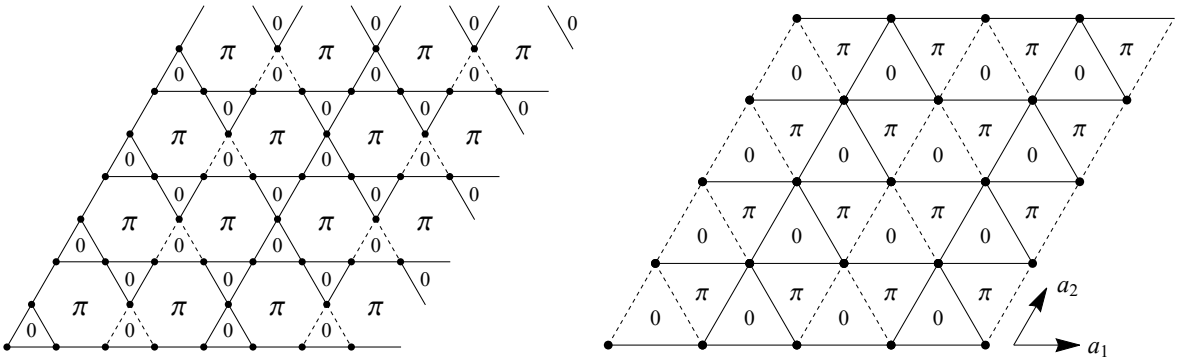

Figure 8.13: Structure de hopping pour l'ansatz de Dirac sur les réseaux Kagome et Triangulaire. Nous montrons l'une des nombreuses jauges possibles pour construire les sauts. Les lignes pleines et pointillées font référence à $\chi_{i,j} = 1$ et -1 respectivement. Les flux à travers les différents polygones qui composent le réseau sont affichés sur les deux réseaux.

Le spectre de champ moyen de l'état de Dirac héberge deux cônes de Dirac par saveur de spin. Nous discutons ensuite de la construction d'excitations monopôles au-dessus de l'état de Dirac.

Les opérateurs monopôles dans les théories de jauge compactes (comme QED_{2+1}) correspondent à des événements tunnel entre différents états fondamentaux de la théorie. Sur le réseau, ils peuvent être construits en insérant un seul quantum de flux (flux 2π) et en le distribuant uniformément sur l'ensemble du réseau. Pour ce faire, nous devons généraliser notre hamiltonien auxiliaire comme suit

$$\mathscr{H}_0 = \sum_{\langle i,j\rangle,\sigma} \chi^0_{i,j} e^{\mathrm{i}\alpha_{i,j}} c^\dagger_{i,\sigma} c_{j,\sigma} + \mathrm{h.c.}, \tag{8.23}$$

Ici, les phases additionnelles $\alpha_{i,j}$ prennent en compte les flux dus au monopôle, et sont choisies de telle sorte qu'un flux uniforme de $2\pi/L^2$ perce chaque parallélogramme du réseau (comprenant deux triangles et un hexagone pour le réseau de Kagome, et seulement deux triangles à pointes opposées pour le réseau triangulaire). On remarque que $\chi^0_{i,j}$ est le même que dans la figure 8.13, donc l'excitation du monopôle est construite sur un fond de flux π sur les deux réseaux. Un choix de sauts sur le réseau triangulaire est montré dans la figure 8.14.

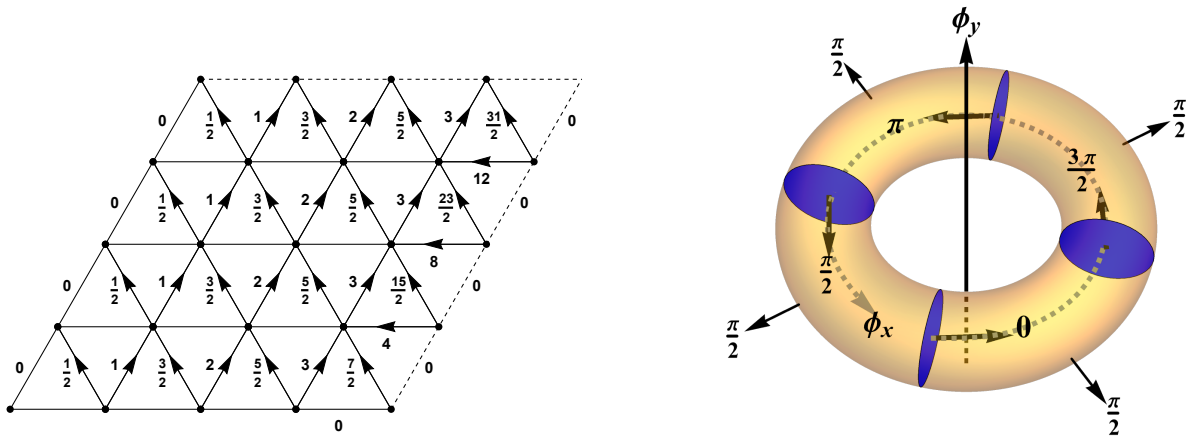

Figure 8.14: (a) Phases complexes de sauts $\alpha_{i,j}$ pour l'ansatz monopôle uniforme sur le réseau triangulaire $L = 4$ avec des conditions aux limites périodiques, en unités de $2\pi/L^2$. Les lignes continues sans flèches indiquent un véritable saut uniforme. Chaque plaquette a un flux de $2\pi/L^2$ modulo 2π. (b) Flux à travers (un ensemble de) boucles incontractibles du tore $L = 4$ pour l'état monopôle. Sont également représentés schématiquement les angles ϕ_x et ϕ_y, qui contrôlent les conditions aux limites.

En raison de l'insertion de ces flux non triviaux, la symétrie translationnelle est brisée sur les amas finis, mais est restaurée dans la limite thermodynamique. Nous notons également qu'en raison des flux non triviaux à travers les plaquettes sur les deux réseaux, la fonction d'onde de spin résultante brise la symétrie de renversement temporel et de réflexion, mais préserve le produit des deux. Par conséquent, cet état représente un liquide de spin chiral (CSL). Ensuite, en surveillant l'énergétique des états monopoles par rapport au DSL, nous pouvons également commenter la stabilité énergétique du DSL par rapport à (une famille de) CSL.

Dans les deux sections suivantes, nous discutons des principaux résultats de notre travail, concernant les impulsions et l'énergétique des excitations monopôles.

8.4.2 Moments monopôles

L'insertion d'un monopôle entraîne une dégénérescence double à l'énergie de Fermi (par spin), et différentes occupations de ces deux niveaux donnent trois monopôles singulets et un triplet. Le remplissage de ces deux orbitales avec la même espèce de spin (↑ ou ↓) conduit respectivement à la composante $S_z = +1, -1$ du triplet. Le secteur $S_z = 0$ peut être occupé de quatre manières, illustrées ci-dessous

$$
\begin{aligned}
|\Phi_1\rangle &= \\
|\Phi_2\rangle &= \\
|\Phi_3\rangle &= \\
|\Phi_4\rangle &=
\end{aligned}
\tag{8.24}
$$

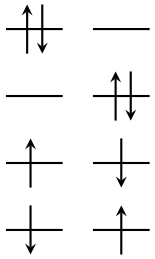

À partir des quatre états ci-dessus, nous pouvons construire trois singulets et la composante $S_z = 0$ du triplet. Alors que le monopôle triplet simple est voué à avoir une impulsion définie dans la limite thermodynamique, les monopôles singulets avec des impulsions définies sont censés être des superpositions des états singulets ci-dessus. Pour calculer les états propres approximatifs des traductions sur des amas finis pour les monopôles singulets, nous construisons et codiagonalisons une paire de matrices 4×4 avec les éléments $\langle \Phi_m | \hat{G}_{T_i} \hat{T}_i | \Phi_n \rangle$ (et $\langle \Psi_m | \hat{T}_i | \Psi_n \rangle$) ($i = 1, 2$, et $m, n = 1 \ldots 4$) pour les états de monopôle en champ moyen (et projeté). Ici, $\hat{G}_{T_i}$ est la transformation de jauge $U(1)$ qui annule partiellement l'effet des traductions selon la direction $\vec{a}_i$. Les états propres de ces matrices sont divisés en deux blocs de dimensions 3×3 et 1×1, correspondant respectivement aux secteurs singulet et triplet (composante $S_z = 0$). Soient les valeurs propres de la forme Ae^{ik_i}. Lorsque les états se rapprochent des états propres exacts des translations, l'amplitude A doit tendre vers 1, ce que l'on observe sur la figure 8.15.

Il est intéressant de noter que nous observons que les fonctions d'onde projetées (qui prennent en compte les fluctuations temporelles de jauge) convergent beaucoup plus rapidement vers le résultat de la limite thermodynamique que les fonctions d'onde du champ moyen.

Les moments des monopôles que nous observons sont parfaitement conformes aux prédictions récentes de la théorie des champs [260, 261].

8.4.3 Energétique monopole

Le DSL a été proposé comme candidat à l'état fondamental à la fois pour le modèle de Kagome Heisenberg du voisin le plus proche [74, 242] et pour le modèle $J_1 - J_2$ sur le réseau triangulaire avec J_2 à peu près dans la région $0,06 \leq J_2 \leq 0,16$ [243, 244]. Ces deux modèles ont été largement étudiés au cours des deux dernières décennies, et il existe également des propositions alternatives pour la nature de l'état fondamental et la région de la phase liquide de spin, et un consensus

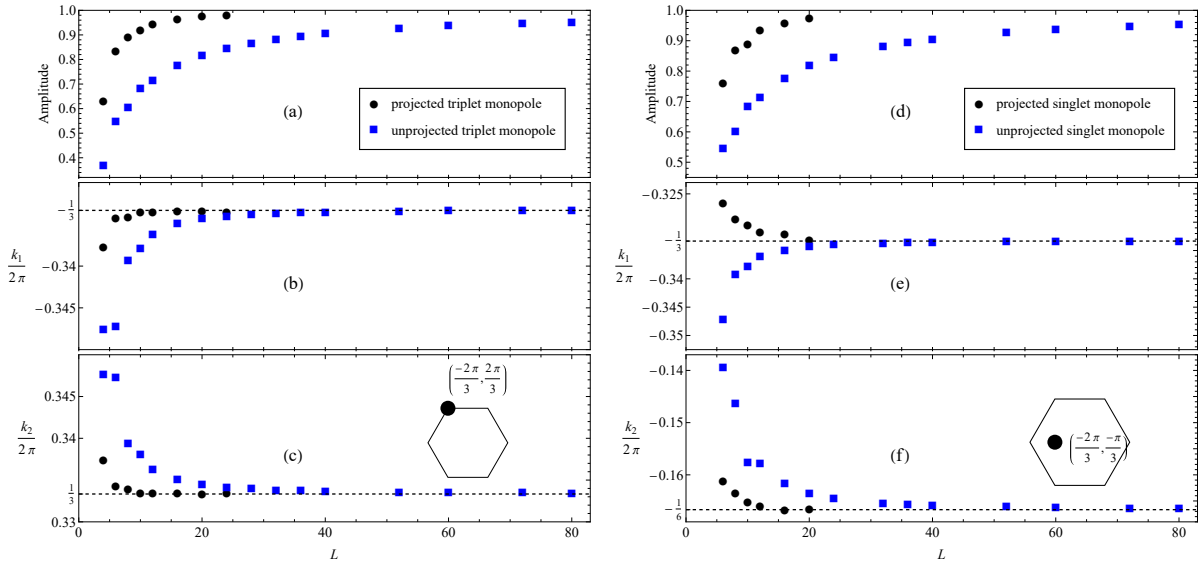

Figure 8.15: Réseau triangulaire : amplitude et phase de recouvrement dans l'équation (**??**) pour le triplet ((a)-(c)) et l'un des trois monopôles singulets ((d)-(f)) en fonction de la taille du système linéaire L. Les résultats sont présentés à la fois pour les recouvrements de champ moyen (calculés exactement comme les déterminants de Slater) et les fonctions d'onde projetées de Gutzwiller (calculées par échantillonnage de Monte Carlo). Les résultats de champ moyen coïncident avec ceux de [260]. Les encarts montrent les points $(\vec{k}.\vec{a}_1, \vec{k}.\vec{a}_2) = (k_1, k_2)$ sur la zone de Brillouin correspondant aux tracés. Le tracé d'amplitude correspond à k_1, et un comportement identique est observé pour k_2. Les barres d'erreur des données de Monte Carlo sont plus petites que la taille des symboles et sont estimées par un échantillonnage statistique des valeurs propres des matrices de chevauchement.

complet n'a pas encore été atteint.

$$\begin{aligned} \mathcal{H}_{\text{Kagome}} &= J \sum_{\langle i,j \rangle} \mathbf{S}_i \cdot \mathbf{S}_j \\ \mathcal{H}_{\text{Triangulaire}} &= J_1 \sum_{\langle ij \rangle} \mathbf{S}_i \cdot \mathbf{S}_j + J_2 \sum_{\langle\langle ik \rangle\rangle} \mathbf{S}_i \cdot \mathbf{S}_k \end{aligned} \tag{8.25}$$

Dans cette section, nous étudions les énergies variationnelles des ansatzes monopôles pour ces modèles. Nous choisissons $J_2 = J_1/8$ dans $\mathcal{H}_{\text{Triangulaire}}$, qui est considéré comme étant en phase QSL.Les principales questions que nous abordons sont les suivantes : (a) Le DSL est-il énergétiquement stable ou instable pour former des états chiraux (avec des monopôles de charge générique Q) ? (b) Quel est l'écart énergétique des excitations des monopôles dans la limite thermodynamique après projection ? (c) Comment l'énergétique des monopôles se compare-t-elle aux calculs de la théorie des champs dans la grande limite N_f ?

Tout d'abord, dans la figure 8.16, nous calculons l'énergie pour différentes excitations monopôles sur les deux réseaux. Nous pouvons clairement voir que les excitations sont ininterrompues dans la limite thermodynamique, avec une mise à l'échelle linéaire inverse du

système.

Nous observons également que les excitations des trous de particules construites au-dessus des cônes de Dirac sont également sans interruption après projection.

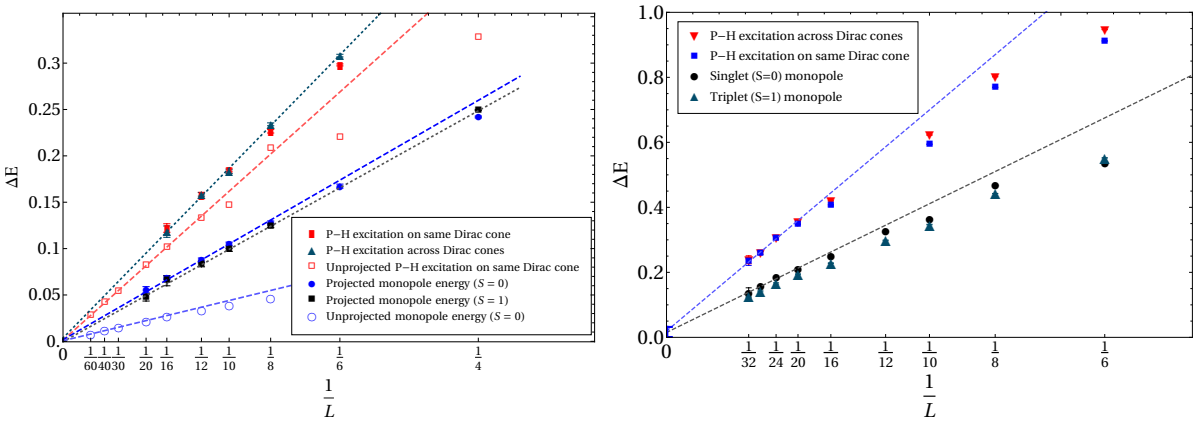

Figure 8.16: Mise à l'échelle de la taille de l'intervalle monopole simple (par rapport à l'état de Dirac) pour les monopoles singulet et triplet pour les réseaux Kagome et triangulaire respectivement. Le cas non projeté (pas de projection de Gutzwiller) est rapporté pour le réseau Kagome à des fins de comparaison. Les excitations de spinon particule-trou (P-H) de la fonction d'onde de Dirac sont également présentées, soit dans le même cône de Dirac, soit à travers les cônes de Dirac.

De plus, nous considérons des valeurs plus élevées de la charge du monopôle Q, c'est-à-dire incluant un flux magnétique de $2\pi Q$. L'énergie des monopôles de charge Q devrait évoluer avec un comportement non trivial, comme indiqué dans les calculs théoriques de champ de Ref. [262] pour le terme d'ordre dominant dans le développement $1/N_f$. Nos résultats pour $E_Q - E_0$ sont rapportés Fig. 8.17 pour quelques valeurs de Q et différentes tailles de cluster L. De plus, nous rapportons également la comparaison directe entre nos résultats variationnels multipliés par L et les dimensions d'échelle (y compris N_f, pris égal à 4) obtenues par des calculs théoriques de champ effectués dans le développement à grand N_f [262].

Étant donné les différentes géométries considérées dans ces deux calculs (le tore et la sphère conforme dans les approches variationnelle et analytique, respectivement), et les différentes échelles d'énergie ($J_1 = 1$ et $\hbar = c = 1$, dans les approches variationnelle et analytique, respectivement), nous admettons une « renormalisation » dans nos résultats, qui sont multipliés par $C \approx 0,28$. Il est remarquable de constater qu'il existe une bonne concordance, même si les calculs analytiques concernent la limite $N_f \to \infty$, alors que nos simulations numériques s'appliquent au cas $N_f = 4$. Ce résultat apporte un soutien supplémentaire à la stabilité du liquide de spin de Dirac dans le modèle de Heisenberg $J_1 - J_2$ sur le réseau triangulaire et au fait que le liquide de spin quantique correspondant est décrit par l'électrodynamique quantique en $2+1$ dimensions. Nous notons que des calculs similaires ont été effectués pour les excitations monopôles sur le modèle Kagome Heisenberg avec un très bon effondrement des prédictions de la théorie des

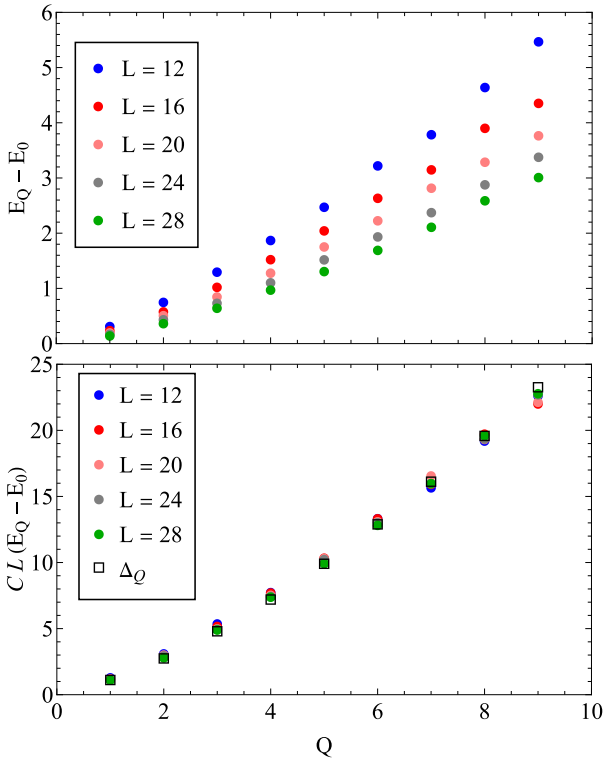

Figure 8.17: Panneau supérieur: Énergie variationnelle des excitations monopolaires $E_Q - E_0$ de charge-Q (singulet), en fonction de Q pour différentes tailles de cluster L. Panneau inférieur: les énergies d'excitation multipliées par $C \times L$ (où $C \approx 0,28$, voir texte) et comparées aux dimensions d'échelle Δ_Q (incluant le facteur $N_f = 4$) obtenues par des calculs théoriques de champ dans la limite d'un grand nombre de points de Dirac dans le spectre fermionique [262].

champs.

8.4.4 Conclusion

Les liquides de spin de Dirac sont des états quantiques exotiques caractérisés par des excitations à basse énergie impliquant des spinons et des monopôles. L'étude de ces excitations est essentielle pour identifier les signatures expérimentales et guider la découverte et la caractérisation des liquides de spin candidats. Dans cette étude, nous avons examiné en profondeur les excitations monopôles dans le modèle de Kagome Heisenberg du voisin le plus proche et le modèle de réseau triangulaire $J_1 - J_2$ ($J_2 = J_1/8$), en utilisant des techniques de diagonalisation exacte et de Monte Carlo variationnelle (VMC). Nos principales conclusions dans cette étude sont les suivantes:

1. Les excitations monopôles et spinoniques sont sans trou dans la limite thermodynamique, sur les deux réseaux.

2. L'énergie variationnelle des états monopôles avec charge générique Q concorde remarquablement bien avec les prédictions de la théorie des champs pour QED_{2+1} en présence

d'un grand nombre de saveurs de fermions N_f.

3. Les fonctions d'onde monopôles projetées convergent plus rapidement (que les déterminants de champ moyen de Slater) vers les états propres exacts des opérateurs de translation, présentant des moments cohérents avec les prédictions de la théorie des champs.

4. Les excitations de flux localisées sur des paires de plaquettes triangulaires individuelles sont sans trou dans la limite thermodynamique en raison d'un très grand chevauchement avec l'état fondamental.

Nos résultats éclairent la physique complexe des modèles frustrés de Heisenberg sur le réseau Kagome et le réseau triangulaire, et fournissent des preuves à l'appui d'un état fondamental liquide de spin de Dirac dans ces systèmes.

APPENDIX A

$SU(N)$ MONOPOLE ENERGY

Consider the following SU(N) permutation hamiltonian

$$H = \sum_{\langle i,j\rangle} \sum_{\alpha\beta} c^{\dagger}_{i\alpha} c_{i\beta}\, c^{\dagger}_{j\beta}\, c_{j\alpha} \tag{A.1}$$

Here, α, β are spin indices that take the values $\alpha, \beta = 1, 2, \ldots N$, and $c^{\dagger}_{i,\alpha}$ ($c_{i,\alpha}$) creates (destroys) a fermion with spin α on site i. For the SU(2) case, the above hamiltonian can be recast as

$$\frac{1}{2} \sum_{\langle i,j\rangle} \sum_{\alpha\beta}^{2} c^{\dagger}_{i\alpha} c_{i\beta}\, c^{\dagger}_{j\beta}\, c_{j\alpha} = \sum_{\langle i,j\rangle} \vec{S}_i \cdot \vec{S}_j + \frac{1}{4} \sum_{\langle i,j\rangle} \hat{n}_i \hat{n}_j \tag{A.2}$$

where $\hat{n}_i$ is the number operator

$$\hat{n}_i = c^{\dagger}_{i\uparrow} c_{i\uparrow} + c^{\dagger}_{i\downarrow} c_{i\downarrow} \tag{A.3}$$

and $\vec{S}_i$ are the usual spin 1/2 Pauli operators. So, in the subspace of the Hilbert space with one particle per site, the model (A.1) is just the Heisenberg hamiltonian upto a constant. In this appendix, our task is to compute the mean field expectation value of the hamiltonian (A.1) for a generic many body wavefunction $|\Phi_0\rangle$

$$E_{MF} = \frac{\langle \Phi_0 | H | \Phi_0 \rangle}{\langle \Phi_0 | | \Phi_0 \rangle} \tag{A.4}$$

We assume a lattice of L sites with N/2 fermions per site. Let $|\Phi_0\rangle$ be constructed as a product of $L/2$ orbitals for each spin:

$$|\Phi_0\rangle = \prod_{\alpha=1}^{N} \left(\prod_{x=1}^{L/2} \phi^{\dagger}_{x\alpha} \right) |0\rangle \tag{A.5}$$

The orbitals $\phi^\dagger_{x\alpha}$ are constructed by diagonalizing the tightbinding model for the monopole ansatz: (in our specific case, the orbitals are the same for all flavors, so U doesn't depend on α)

$$\begin{aligned} \phi^\dagger_{x\alpha} &= \sum_{j=1}^{L} U_{jx}\, c^\dagger_{j\alpha} \\ \implies c^\dagger_{i\alpha} &= \sum_{x=1}^{L} U^*_{ix}\, \phi^\dagger_{x\alpha} \end{aligned} \tag{A.6}$$

These orbitals are orthonormal:

$$\langle 0|\, \phi_{y\beta}\, \phi^\dagger_{x\alpha}\, |0\rangle = \delta_{\alpha\beta}\delta_{xy} \tag{A.7}$$

Using the second line of (A.6), we can expand the mean field energy as

$$\begin{aligned} E_{MF} &= -\sum_{\langle i,j\rangle}\sum_{\alpha\beta} \langle\Phi_0|\, c^\dagger_{i\alpha}\, c^\dagger_{j\beta}\, c_{i\beta}\, c_{j\alpha}\, |\Phi_0\rangle \\ &= -\sum_{\langle i,j\rangle}\sum_{\alpha\beta} \langle\Phi_0| \left(\sum_x U^*_{ix}\, \phi^\dagger_{x\alpha}\right)\left(\sum_y U^*_{jy}\, \phi^\dagger_{y\beta}\right)\left(\sum_z U_{iz}\, \phi_{z\beta}\right)\left(\sum_w U_{jw}\, \phi_{w\alpha}\right) |\Phi_0\rangle \\ &= -\sum_{\langle i,j\rangle}\sum_{\alpha\beta}\sum_{xyzw}^{L} U^*_{ix} U^*_{jy} U_{iz} U_{jw}\, \langle\Phi_0|\, \phi^\dagger_{x\alpha}\, \phi^\dagger_{y\beta}\, \phi_{z\beta}\, \phi_{w\alpha}\, |\Phi_0\rangle \end{aligned} \tag{A.8}$$

In the state $|\Phi_0\rangle$, only operators of flavor α, β are relevant for the overlap. Further, the overlap is non-zero only if $x, y, z, w \in [1, L/2]$. The calculation can be separated into two parts, $\alpha \neq \beta$ and $\alpha = \beta$. Let us first look at $\alpha \neq \beta$:

$$\begin{aligned} &-\sum_{\alpha\neq\beta}\sum_{xyzw}^{L/2} U^*_{ix} U^*_{jy} U_{iz} U_{jw}\, \langle\Phi_0|\, \phi^\dagger_{x\alpha}\, \phi^\dagger_{y\beta}\, \phi_{z\beta}\, \phi_{w\alpha}\, |\Phi_0\rangle \\ &= -\sum_{\alpha\neq\beta}\sum_{xyzw}^{L/2} U^*_{ix} U^*_{jy} U_{iz} U_{jw}\, \delta_{xw}\, \delta_{yz} \\ &= -\sum_{\alpha\neq\beta}\sum_{xy}^{L/2} U^*_{ix} U^*_{jy} U_{iy} U_{jx} = -\left(N^2 - N\right) |A_{ij}|^2 \end{aligned} \tag{A.9}$$

where we define A_{ij} to be (note: the summation is only till $L/2$)

$$A_{ij} = \sum_{x=1}^{L/2} U_{jx} U^*_{ix} \tag{A.10}$$

For the $\alpha = \beta$ case, we have

$$\begin{aligned} &-\sum_{\alpha}^{N}\sum_{xyzw}^{L/2} U_{ix}^{*}U_{jy}^{*}U_{iz}U_{jw}(1-\delta_{zw})\left(\delta_{xw}\delta_{yz}-\delta_{xz}\delta_{yw}\right) \\ &\quad = -N\sum_{xy}^{L/2}\left(U_{ix}^{*}U_{jy}^{*}U_{iy}U_{jx}-U_{ix}^{*}U_{jy}^{*}U_{ix}U_{jy}\right) \\ &\quad = -N|A_{ij}|^{2}+NA_{ii}A_{jj} \end{aligned} \tag{A.11}$$

So, the modified final result is

$$E_{MF} = -\sum_{\langle i,j\rangle}\left[N^{2}|A_{ij}|^{2}+NA_{ii}A_{jj}\right] \tag{A.12}$$

Note however, that $A_{ii} = A_{jj} = 1/2$, since we are at half filling. Consider the expectation value

$$\begin{aligned} &\langle\Phi_0|\, c_{i\alpha}^{\dagger}\, c_{i\alpha}\,|\Phi_0\rangle = \frac{1}{2} \\ &= \sum_{x=1}^{L}\sum_{y=1}^{L} U_{ix}^{*}U_{iy}\,\langle\Phi_0|\,\phi_{x\alpha}^{\dagger}\phi_{y\alpha}\,|\Phi_0\rangle \\ &= \sum_{x,y=1}^{L/2} U_{ix}^{*}U_{iy}\,\delta_{xy} = \sum_{x=1}^{L/2} U_{ix}^{*}U_{ix} \end{aligned} \tag{A.13}$$

Therefore, we finally have

$$\boxed{E_{MF} = -\sum_{\langle i,j\rangle}\left[N^{2}|A_{ij}|^{2}+\frac{N}{4}\right]} \tag{A.14}$$

We finally note that only the first term $N^2|A_{ij}|^2$ matters when we compute the difference between the monopole and the Dirac energy. The single-monople gap is obtained by taking the difference between the case with one monopole (spread over the entire torus) and no monopoles (i.e., the Dirac state):

$$\Delta E_0 = -N_f^2\sum_{\langle i,j\rangle}\left[|A_{i,j}^{\text{monopole}}|^2-|A_{i,j}^{\text{Dirac}}|^2\right] \tag{A.15}$$

For the projected wave functions, we use the Monte Carlo sampling to evaluate the variational energies corresponding to the single monopole and the Dirac state (in both cases, the Gutzwiller projector imposes to have $\mathrm{N}_f/2$ fermions per site). The size scaling of the total monopole energy for $\mathrm{N}_f = 2,4,6,8,10$, and 12 is shown in Fig. A.1.

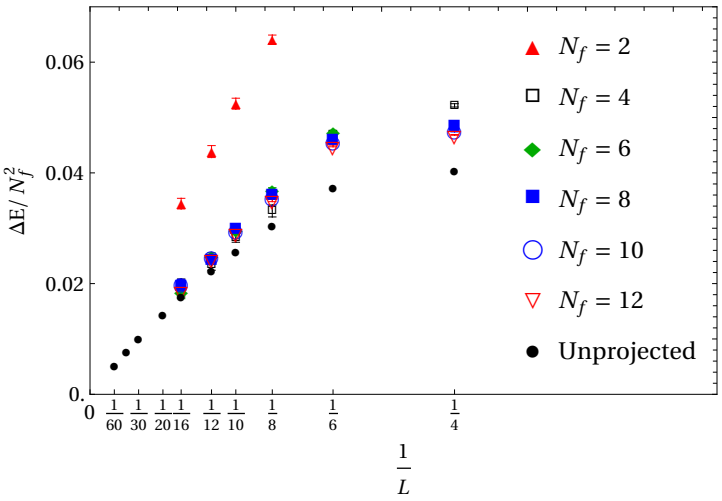

Figure A.2: Single-monopole energies scaled by N_f^2, shown along with the unprojected energy difference Δ_0/N_f^2 from Eq. (A.15).

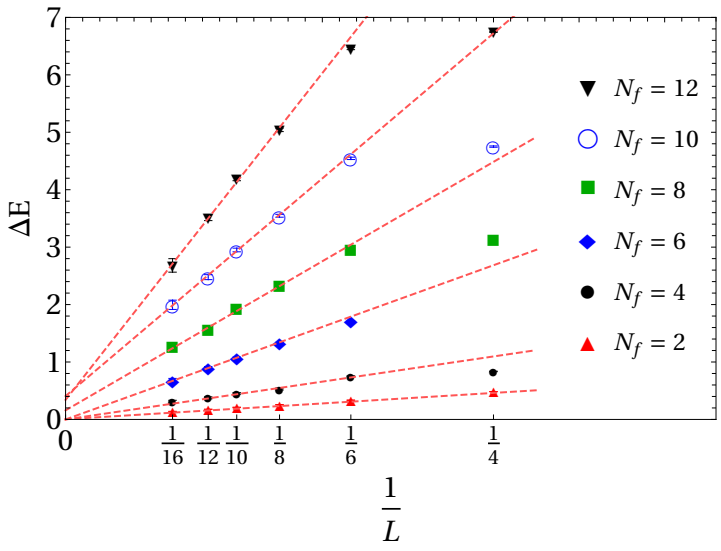

Figure A.1: Single-monopole gap as a function of $1/L$ for various values of N_f, along with best linear fits.

At first glance, the data for $N_f \geq 8$ would suggest a gapped monopole in the thermodynamic limit. However, after further investigation, we believe this to be a finite-size effect. Indeed, by scaling the projected energies by N_f^2, we observe that all the data (except $N_f = 2$) collapse perfectly on top of each other, see Fig. A.2. Furthermore, there is very good agreement between the projected and the unprojected energies calculated from Eq. (A.15), which increases with system size. Finally, we remark that the unprojected data indicates a gapless monopole only if large enough system sizes $L \geq 30$ are considered, which are very difficult to access for the projected wave functions.

APPENDIX B

COMPUTING CHERN NUMBER

Here, we outline the algorithm proposed by Fukui, Hatsugai and Suzuki for computing Chern number [209]. As a reminder, the Chern number of a band is given by the integral of the Berry curvature in the Brillouin Zone (or a sum in a discretized BZ)

$$c = \frac{1}{2\pi i}\int_{\mathrm{BZ}} F(k)dk \tag{B.1}$$

where $F(k)$ is the Berry curvature. Consider a two-dimensional BZ of dimensions $k_i \in [0, 2\pi/q_i)$, where $i = 1,2$. We then discretize the BZ by defining the step sizes $\delta k_i = 2\pi/(q_i N_i)$. Thus, the BZ contains $N_1 N_2$ points $\mathbf{k} = (k_1, k_2)$ given by

$$k_i = 0, \frac{2\pi}{q_i N_i}, \frac{4\pi}{q_i N_i}, \ldots, \frac{2\pi(N_i - 1)}{q_i N_i}, \qquad i = 1,2 \tag{B.2}$$

To compute chern number of a given band, we need the eigenvectors at every $\mathbf{k}$ point, which we denote as $|\Psi(k_1, k_2)\rangle$. These wavefunctions must be periodic in the BZ: $|\Psi(k_1 + 2\pi/q_1, k_2)\rangle = |\Psi(k_1, k_2)\rangle = |\Psi(k_1, k_2 + 2\pi/q_2)\rangle$. The algorithm consists of computing the following phases, called 'link variables'

$$U_1(\mathbf{k}) = \frac{\langle\Psi(k_1,k_2)|\Psi(k_1+\delta k_1,k_2)\rangle}{|\langle\Psi(k_1,k_2)|\Psi(k_1+\delta k_1,k_2)\rangle|} \qquad U_2(\mathbf{k}) = \frac{\langle\Psi(k_1,k_2)|\Psi(k_1,k_2+\delta k_2)\rangle}{|\langle\Psi(k_1,k_2)|\Psi(k_1,k_2+\delta k_2)\rangle|} \tag{B.3}$$

Then, we define the following lattice field strength

$$F(\mathbf{k}) = \ln\left(\frac{U_1(k_1,k_2)\, U_2(k_1+\delta k_1,k_2)}{U_2(k_1,k_2)\, U_1(k_1,k_2+\delta k_2)}\right) \tag{B.4}$$

Essentially, $F(\mathbf{k})$ measures the flux of the gauge field U through the plaquette at $\mathbf{k}$. Care must be taken to ensure that $F(\mathbf{k})$ always lies in the range $[-\pi, \pi)$. The Chern number is then obtained by

summing over the Berry curvature contributions from all the plaquettes in the BZ:

$$c = \frac{1}{2\pi i} \sum_{\mathbf{k}} F(\mathbf{k}) \tag{B.5}$$

This method always yields an integer Chern number irrespective of the number of grids in the BZ. Additionally, it has the advantage of not requiring a gauge-fixing procedure for the phases of the eigenstates since we only deal with fluxes through the plaquettes. In practice, this method yields the correct Chern numbers even at coarse discretizations of the BZ. For more details, we refer the reader to [209].

BIBLIOGRAPHY

[1] Lucile Savary and Leon Balents. “Quantum spin liquids: a review”. In: *Reports on Progress in Physics* 80.1 (2016), p. 016502.

[2] M. Hermanns, I. Kimchi, and J. Knolle. “Physics of the Kitaev Model: Fractionalization, Dynamic Correlations, and Material Connections”. In: *Annual Review of Condensed Matter Physics* 9.Volume 9, 2018 (2018), pp. 17–33. ISSN: 1947-5462. DOI: https://doi.org/10.1146/annurev-conmatphys-033117-053934. URL: https://www.annualreviews.org/content/journals/10.1146/annurev-conmatphys-033117-053934.

[3] C. Broholm et al. “Quantum spin liquids”. In: *Science* 367.6475 (2020), eaay0668. DOI: 10.1126/science.aay0668. eprint: https://www.science.org/doi/pdf/10.1126/science.aay0668. URL: https://www.science.org/doi/abs/10.1126/science.aay0668.

[4] Yi Zhou, Kazushi Kanoda, and Tai-Kai Ng. “Quantum spin liquid states”. In: *Rev. Mod. Phys.* 89.2 (2017), p. 025003.

[5] Philip W Anderson. “Resonating valence bonds: A new kind of insulator?” In: *Materials Research Bulletin* 8.2 (1973), pp. 153–160.

[6] Xiao-Gang Wen. “Quantum orders and symmetric spin liquids”. In: *Phys. Rev. B* 65 (16 Apr. 2002), p. 165113. DOI: 10.1103/PhysRevB.65.165113. URL: https://link.aps.org/doi/10.1103/PhysRevB.65.165113.

[7] G. Baskaran and P. W. Anderson. “Gauge theory of high-temperature superconductors and strongly correlated Fermi systems”. In: *Phys. Rev. B* 37 (1 Jan. 1988), pp. 580–583. DOI: 10.1103/PhysRevB.37.580. URL: https://link.aps.org/doi/10.1103/PhysRevB.37.580.

[8] G. Baskaran, Z. Zou, and P.W. Anderson. “The resonating valence bond state and high-Tc superconductivity — a mean field theory”. In: *Solid State Communications* 88.11 (1993). Special Issue A Celebratory Issue to Commemorate 30 Years of Solid State Communications, pp. 853–856. ISSN: 0038-1098. DOI: https://doi.org/10.1016/0038-1098(93)90256-M. URL: https://www.sciencedirect.com/science/article/pii/003810989390256M.

[9] Patrick A. Lee, Naoto Nagaosa, and Xiao-Gang Wen. “Doping a Mott insulator: Physics of high-temperature superconductivity”. In: *Rev. Mod. Phys.* 78 (1 Jan. 2006), pp. 17–85. DOI: 10.1103/RevModPhys.78.17. URL: https://link.aps.org/doi/10.1103/RevModPhys.78.17.

[10] C. Lacroix, P. Mendels, and F. Mila. *Introduction to Frustrated Magnetism: Materials, Experiments, Theory*. Springer Series in Solid-State Sciences, 2011. DOI: 10.1007/978-3-642-10589-0. URL: https://link.springer.com/book/10.1007/978-3-642-10589-0#bibliographic-information.

[11] Luca Capriotti, Adolfo E Trumper, and Sandro Sorella. “Long-range Néel order in the triangular Heisenberg model”. In: *Physical review letters* 82.19 (1999), p. 3899.

[12] Lev Davidovich Landau et al. “On the theory of phase transitions”. In: *Zh. eksp. teor. Fiz* 7.19-32 (1937), p. 926.

[13] Xiao-Gang Wen. “Quantum orders and symmetric spin liquids”. In: *Physical Review B* 65.16 (2002), p. 165113.

[14] Xiao-Gang Wen. “Quantum orders in an exact soluble model”. In: *Physical review letters* 90.1 (2003), p. 016803.

[15] Xiao-Gang Wen. *Quantum Field Theory of Many-Body Systems: From the Origin of Sound to an Origin of Light and Electrons*. Oxford University Press, Sept. 2007. ISBN: 9780199227259. DOI: 10.1093/acprof:oso/9780199227259.001.0001. URL: https://doi.org/10.1093/acprof:oso/9780199227259.001.0001.

[16] Francesco Ferrari. “Static and dynamical properties of frustrated spin models”. PhD thesis. SISSA, 2019.

[17] Jonas Sonnenschein. “Mean-field theory and projective symmetry group classifications of quantum spin liquids”. PhD thesis. Freie Universitaet Berlin (Germany), 2020.

[18] Hans Bethe. “On the theory of metals, I. Eigenvalues and eigenfunctions of a linear chain of atoms”. In: *Selected Works Of Hans A Bethe: (With Commentary)*. World Scientific, 1997, pp. 155–183.

[19] Bella Lake et al. “Quantum criticality and universal scaling of a quantum antiferromagnet”. In: *Nature materials* 4.4 (2005), pp. 329–334.

[20] A. Kitaev. “Anyons in an exactly solved model and beyond”. In: *Ann. Phys. (Amst.)* 321.1 (2006), pp. 2–111. DOI: https://doi.org/10.1016/j.aop.2005.10.005. URL: https://www.sciencedirect.com/science/article/pii/S0003491605002381.

[21] A.Yu. Kitaev. “Fault-tolerant quantum computation by anyons”. In: *Annals of Physics* 303.1 (2003), pp. 2–30. ISSN: 0003-4916. DOI: https://doi.org/10.1016/S0003-4916(02)00018-0. URL: https://www.sciencedirect.com/science/article/pii/S0003491602000180.

[22] Xiao-Gang Wen. “Topological orders in rigid states”. In: *International Journal of Modern Physics B* 4.02 (1990), pp. 239–271.

[23] Michael Levin and Xiao-Gang Wen. “Detecting topological order in a ground state wave function”. In: *Physical review letters* 96.11 (2006), p. 110405.

[24] Alexei Kitaev and John Preskill. “Topological entanglement entropy”. In: *Physical review letters* 96.11 (2006), p. 110404.

[25] Hong-Chen Jiang, Zhenghan Wang, and Leon Balents. “Identifying topological order by entanglement entropy”. In: *Nature Physics* 8.12 (2012), pp. 902–905.

[26] Thomas Werkmeister et al. *Anyon braiding and telegraph noise in a graphene interferometer*. 2024. arXiv: 2403.18983 [cond-mat.mes-hall]. URL: https://arxiv.org/abs/2403.18983.

[27] Chetan Nayak et al. “Non-Abelian anyons and topological quantum computation”. In: *Reviews of Modern Physics* 80.3 (2008), pp. 1083–1159.

[28] Michael A Levin and Xiao-Gang Wen. “String-net condensation: A physical mechanism for topological phases”. In: *Physical Review B—Condensed Matter and Materials Physics* 71.4 (2005), p. 045110.

[29] Oliver Buerschaper and Miguel Aguado. “Mapping Kitaev’s quantum double lattice models to Levin and Wen’s string-net models”. In: *Phys. Rev. B* 80 (15 Oct. 2009), p. 155136. DOI: 10.1103/PhysRevB.80.155136. URL: https://link.aps.org/doi/10.1103/PhysRevB.80.155136.

[30] Zheng-Cheng Gu et al. “Tensor-product representations for string-net condensed states”. In: *Physical Review B—Condensed Matter and Materials Physics* 79.8 (2009), p. 085118.

[31] Liang Kong. “Anyon condensation and tensor categories”. In: *Nuclear Physics B* 886 (2014), pp. 436–482.

[32] M. R. Norman. “Colloquium: Herbertsmithite and the search for the quantum spin liquid”. In: *Rev. Mod. Phys.* 88 (4 Dec. 2016), p. 041002. DOI: 10.1103/RevModPhys.88.041002. URL: https://link.aps.org/doi/10.1103/RevModPhys.88.041002.

[33] Y. Y. Huang et al. “Heat Transport in Herbertsmithite: Can a Quantum Spin Liquid Survive Disorder?” In: *Phys. Rev. Lett.* 127 (26 Dec. 2021), p. 267202. DOI: 10.1103/PhysRevLett.127.267202. URL: https://link.aps.org/doi/10.1103/PhysRevLett.127.267202.

[34] Tokuro Shimokawa, Ken Watanabe, and Hikaru Kawamura. “Static and dynamical spin correlations of the $S = \frac{1}{2}$ random-bond antiferromagnetic Heisenberg model on the triangular and kagome lattices”. In: *Phys. Rev. B* 92 (13 Oct. 2015), p. 134407. DOI: 10.1103/PhysRevB.92.134407. URL: https://link.aps.org/doi/10.1103/PhysRevB.92.134407.

[35] Zhenyuan Zeng et al. “Possible Dirac quantum spin liquid in the kagome quantum antiferromagnet $YCu_3(OH)_6Br_2[Br_x(OH)_{1-x}]$”. In: *Phys. Rev. B* 105 (12 Mar. 2022), p. L121109. DOI: 10.1103/PhysRevB.105.L121109. URL: https://link.aps.org/doi/10.1103/PhysRevB.105.L121109.

[36] Zhenyuan Zeng et al. “Spectral evidence for Dirac spinons in a kagome lattice antiferromagnet”. In: *Nature Physics* 20.7 (July 2024), pp. 1097–1102. ISSN: 1745-2481. DOI: 10.1038/s41567-024-02495-z. URL: https://doi.org/10.1038/s41567-024-02495-z.

[37] Yuesheng Li et al. “Gapless quantum spin liquid ground state in the two-dimensional spin-1/2 triangular antiferromagnet $YbMgGaO_4$”. In: *Scientific Reports* 5.1 (Nov. 2015), p. 16419. ISSN: 2045-2322. DOI: 10.1038/srep16419. URL: https://doi.org/10.1038/srep16419.

[38] Yuesheng Li et al. “Rare-Earth Triangular Lattice Spin Liquid: A Single-Crystal Study of $YbMgGaO_4$”. In: *Phys. Rev. Lett.* 115 (16 Oct. 2015), p. 167203. DOI: 10.1103/PhysRevLett.115.167203. URL: https://link.aps.org/doi/10.1103/PhysRevLett.115.167203.

[39] Yuesheng Li et al. “Muon Spin Relaxation Evidence for the $U(1)$ Quantum Spin-Liquid Ground State in the Triangular Antiferromagnet $YbMgGaO_4$”. In: *Phys. Rev. Lett.* 117 (9 Aug. 2016), p. 097201. DOI: 10.1103/PhysRevLett.117.097201. URL: https://link.aps.org/doi/10.1103/PhysRevLett.117.097201.

[40] Joseph A.M. Paddison et al. “Continuous excitations of the triangular-lattice quantum spin liquid $YbMgGaO_4$”. In: *Nature Physics* 13.2 (Feb. 2017), pp. 117–122. ISSN: 1745-2481. DOI: 10.1038/nphys3971. URL: https://doi.org/10.1038/nphys3971.

[41] Yuesheng Li et al. “Nearest-neighbour resonating valence bonds in $YbMgGaO_4$”. In: *Nature Communications* 8.1 (June 2017), p. 15814. ISSN: 2041-1723. DOI: 10.1038/ncomms15814. URL: https://doi.org/10.1038/ncomms15814.

[42] Yao Shen et al. “Fractionalized excitations in the partially magnetized spin liquid candidate $YbMgGaO_4$”. In: *Nature Communications* 9.1 (Oct. 2018), p. 4138. ISSN: 2041-1723. DOI: 10.1038/s41467-018-06588-1. URL: https://doi.org/10.1038/s41467-018-06588-1.

[43] Y. Xu et al. “Absence of Magnetic Thermal Conductivity in the Quantum Spin-Liquid Candidate $YbMgGaO_4$”. In: *Phys. Rev. Lett.* 117 (26 Dec. 2016), p. 267202. DOI: 10.1103/PhysRevLett.117.267202. URL: https://link.aps.org/doi/10.1103/PhysRevLett.117.267202.

[44] Zhenyue Zhu et al. “Disorder-Induced Mimicry of a Spin Liquid in $YbMgGaO_4$”. In: *Phys. Rev. Lett.* 119 (15 Oct. 2017), p. 157201. DOI: 10.1103/PhysRevLett.119.157201. URL: https://link.aps.org/doi/10.1103/PhysRevLett.119.157201.

[45] Zhen Ma et al. “Spin-Glass Ground State in a Triangular-Lattice Compound $YbZnGaO_4$”. In: *Phys. Rev. Lett.* 120 (8 Feb. 2018), p. 087201. DOI: 10.1103/PhysRevLett.120.087201. URL: https://link.aps.org/doi/10.1103/PhysRevLett.120.087201.

[46] Itamar Kimchi, Adam Nahum, and T. Senthil. “Valence Bonds in Random Quantum Magnets: Theory and Application to $YbMgGaO_4$”. In: *Phys. Rev. X* 8 (3 July 2018), p. 031028. DOI: 10.1103/PhysRevX.8.031028. URL: https://link.aps.org/doi/10.1103/PhysRevX.8.031028.

[47] Lei Ding et al. “Gapless spin-liquid state in the structurally disorder-free triangular antiferromagnet $NaYbO_2$”. In: *Phys. Rev. B* 100 (14 Oct. 2019), p. 144432. DOI: 10.1103/PhysRevB.100.144432. URL: https://link.aps.org/doi/10.1103/PhysRevB.100.144432.

[48] Mitchell M. Bordelon et al. “Field-tunable quantum disordered ground state in the triangular-lattice antiferromagnet $NaYbO_2$”. In: *Nature Physics* 15.10 (Oct. 2019), pp. 1058–1064. ISSN: 1745-2481. DOI: 10.1038/s41567-019-0594-5. URL: https://doi.org/10.1038/s41567-019-0594-5.

[49] Mitchell M. Bordelon et al. “Spin excitations in the frustrated triangular lattice antiferromagnet $NaYbO_2$”. In: *Phys. Rev. B* 101 (22 June 2020), p. 224427. DOI: 10.1103/PhysRevB.101.224427. URL: https://link.aps.org/doi/10.1103/PhysRevB.101.224427.

[50] Peng-Ling Dai et al. “Spinon Fermi Surface Spin Liquid in a Triangular Lattice Antiferromagnet $NaYbSe_2$”. In: *Phys. Rev. X* 11 (2 May 2021), p. 021044. DOI: 10.1103/PhysRevX.11.021044. URL: https://link.aps.org/doi/10.1103/PhysRevX.11.021044.

[51] Ya-Ting Jia et al. “Mott Transition and Superconductivity in Quantum Spin Liquid Candidate $NaYbSe_2$”. In: *Chinese Physics Letters* 37.9 (Sept. 2020), p. 097404. DOI: 10.1088/0256-307X/37/9/097404. URL: https://dx.doi.org/10.1088/0256-307X/37/9/097404.

[52] Jiangtao Wu et al. “Magnetic field effects on the quantum spin liquid behaviors of $NaYbS_2$”. In: *Quantum Frontiers* 1.1 (Nov. 2022), p. 13. ISSN: 2731-6106. DOI: 10.1007/s44214-022-00011-z. URL: https://doi.org/10.1007/s44214-022-00011-z.

[53] Satoshi Yamashita et al. “Thermodynamic properties of a spin-1/2 spin-liquid state in a κ-type organic salt”. In: *Nature Physics* 4.6 (June 2008), pp. 459–462. ISSN: 1745-2481. DOI: 10.1038/nphys942. URL: https://doi.org/10.1038/nphys942.

[54] Minoru Yamashita et al. “Highly mobile gapless excitations in a two-dimensional candidate quantum spin liquid”. en. In: *Science* 328.5983 (June 2010), pp. 1246–1248.

[55] Sijie Xu et al. *Realization of U(1) Dirac Quantum Spin Liquid in YbZn2GaO5*. 2023. arXiv: 2305.20040.

[56] Simon Trebst and Ciarán Hickey. "Kitaev materials". In: *Physics Reports* 950 (2022), pp. 1–37. ISSN: 0370-1573. DOI: https://doi.org/10.1016/j.physrep.2021.11.003. URL: https://www.sciencedirect.com/science/article/pii/S0370157321004051.

[57] Y. Kasahara et al. "Majorana quantization and half-integer thermal quantum Hall effect in a Kitaev spin liquid". In: *Nature* 559.7713 (July 2018), pp. 227–231. ISSN: 1476-4687. DOI: 10.1038/s41586-018-0274-0. URL: https://doi.org/10.1038/s41586-018-0274-0.

[58] G. Jackeli and G. Khaliullin. "Mott Insulators in the Strong Spin-Orbit Coupling Limit: From Heisenberg to a Quantum Compass and Kitaev Models". In: *Phys. Rev. Lett.* 102 (1 Jan. 2009), p. 017205. DOI: 10.1103/PhysRevLett.102.017205. URL: https://link.aps.org/doi/10.1103/PhysRevLett.102.017205.

[59] Clemens Kuhlenkamp et al. "Chiral Pseudospin Liquids in Moiré Heterostructures". In: *Physical Review X* 14.2 (2024), p. 021013.

[60] Hendrik Weimer et al. "A Rydberg quantum simulator". In: *Nature Physics* 6.5 (2010), pp. 382–388.

[61] Rhine Samajdar et al. "Emergent $\mathbb{Z}_2$ Gauge Theories and Topological Excitations in Rydberg Atom Arrays". In: *Phys. Rev. Lett.* 130 (4 Jan. 2023), p. 043601. DOI: 10.1103/PhysRevLett.130.043601. URL: https://link.aps.org/doi/10.1103/PhysRevLett.130.043601.

[62] Rhine Samajdar et al. "Quantum phases of Rydberg atoms on a kagome lattice". In: *Proceedings of the National Academy of Sciences* 118.4 (2021), e2015785118.

[63] Ruben Verresen, Mikhail D. Lukin, and Ashvin Vishwanath. "Prediction of Toric Code Topological Order from Rydberg Blockade". In: *Phys. Rev. X* 11 (3 July 2021), p. 031005. DOI: 10.1103/PhysRevX.11.031005. URL: https://link.aps.org/doi/10.1103/PhysRevX.11.031005.

[64] P. S. Tarabunga et al. "Gauge-Theoretic Origin of Rydberg Quantum Spin Liquids". In: *Phys. Rev. Lett.* 129 (19 Nov. 2022), p. 195301. DOI: 10.1103/PhysRevLett.129.195301. URL: https://link.aps.org/doi/10.1103/PhysRevLett.129.195301.

[65] Bo-Ye Sun et al. "Engineering and Probing Non-Abelian Chiral Spin Liquids Using Periodically Driven Ultracold Atoms". In: *PRX Quantum* 4 (2 May 2023), p. 020329. DOI: 10.1103/PRXQuantum.4.020329. URL: https://link.aps.org/doi/10.1103/PRXQuantum.4.020329.

[66] Matthieu Mambrini and Didier Poilblanc. “Quantum state preparation of topological chiral spin liquids via Floquet engineering”. In: *SciPost Phys.* 17 (2024), p. 011. DOI: 10.21468/SciPostPhys.17.1.011. URL: https://scipost.org/10.21468/SciPostPhys.17.1.011.

[67] Tian-Hua Yang et al. “Quantum Hall states for Rydberg arrays with laser-assisted dipole-dipole interactions”. In: *Physical Review A* 106.2 (2022), p. L021101.

[68] Marcin Kalinowski, Nishad Maskara, and Mikhail D Lukin. “Non-abelian floquet spin liquids in a digital Rydberg simulator”. In: *Physical Review X* 13.3 (2023), p. 031008.

[69] Simon Ohler, Maximilian Kiefer-Emmanouilidis, and Michael Fleischhauer. “Quantum spin liquids of Rydberg excitations in a honeycomb lattice induced by density-dependent Peierls phases”. In: *Phys. Rev. Res.* 5 (1 Feb. 2023), p. 013157. DOI: 10.1103/PhysRevResearch.5.013157. URL: https://link.aps.org/doi/10.1103/PhysRevResearch.5.013157.

[70] S. Weber et al. “Experimentally Accessible Scheme for a Fractional Chern Insulator in Rydberg Atoms”. In: *PRX Quantum* 3 (3 July 2022), p. 030302. DOI: 10.1103/PRXQuantum.3.030302. URL: https://link.aps.org/doi/10.1103/PRXQuantum.3.030302.

[71] J. Knolle and R. Moessner. “A Field Guide to Spin Liquids”. In: *Annual Review of Condensed Matter Physics* 10.1 (2019), pp. 451–472. DOI: 10.1146/annurev-conmatphys-031218-013401. eprint: https://doi.org/10.1146/annurev-conmatphys-031218-013401. URL: https://doi.org/10.1146/annurev-conmatphys-031218-013401.

[72] Tian-Heng Han et al. “Fractionalized excitations in the spin-liquid state of a kagome-lattice antiferromagnet”. In: *Nature* 492.7429 (2012), pp. 406–410.

[73] T. Itou et al. “Quantum spin liquid in the spin-12 triangular antiferromagnet $EtMe_3Sb[Pd(dmit)_2]_2$”. In: *Phys. Rev. B* 77 (10 Mar. 2008), p. 104413. DOI: 10.1103/PhysRevB.77.104413. URL: https://link.aps.org/doi/10.1103/PhysRevB.77.104413.

[74] Y. Ran et al. “Projected-Wave-Function Study of the Spin-1/2 Heisenberg Model on the Kagomé Lattice”. In: *Phys. Rev. Lett.* 98 (11 Mar. 2007), p. 117205. DOI: 10.1103/PhysRevLett.98.117205. URL: https://link.aps.org/doi/10.1103/PhysRevLett.98.117205.

[75] W. L. McMillan. “Ground State of Liquid He^4”. In: *Phys. Rev.* 138 (2A Apr. 1965), A442–A451. DOI: 10.1103/PhysRev.138.A442. URL: https://link.aps.org/doi/10.1103/PhysRev.138.A442.

[76] D. Ceperley, G. V. Chester, and M. H. Kalos. “Monte Carlo simulation of a many-fermion study”. In: *Phys. Rev. B* 16 (7 Oct. 1977), pp. 3081–3099. DOI: 10.1103/PhysRevB.16.3081. URL: https://link.aps.org/doi/10.1103/PhysRevB.16.3081.

[77] V. R. Pandharipande, Steven C. Pieper, and R. B. Wiringa. "Variational Monte Carlo calculations of ground states of liquid ^{4}He and ^{3}He drops". In: *Phys. Rev. B* 34 (7 Oct. 1986), pp. 4571–4582. DOI: 10.1103/PhysRevB.34.4571. URL: https://link.aps.org/doi/10.1103/PhysRevB.34.4571.

[78] J. Carlson et al. "Quantum Monte Carlo methods for nuclear physics". In: *Rev. Mod. Phys.* 87 (3 Sept. 2015), pp. 1067–1118. DOI: 10.1103/RevModPhys.87.1067. URL: https://link.aps.org/doi/10.1103/RevModPhys.87.1067.

[79] Brian L Hammond, William A Lester Jr, and Peter James Reynolds. *Monte Carlo methods in ab initio quantum chemistry*. World Scientific, 1994.

[80] Federico Becca and Sandro Sorella. *Quantum Monte Carlo approaches for correlated systems*. Cambridge University Press, 2017.

[81] Sandro Sorella. "Green function Monte Carlo with stochastic reconfiguration". In: *Physical review letters* 80.20 (1998), p. 4558.

[82] Sandro Sorella. "Generalized Lanczos algorithm for variational quantum Monte Carlo". In: *Physical Review B* 64.2 (2001), p. 024512.

[83] Alexandra Nagy and Vincenzo Savona. "Variational quantum Monte Carlo method with a neural-network ansatz for open quantum systems". In: *Physical review letters* 122.25 (2019), p. 250501.

[84] Corey Adams et al. "Variational Monte Carlo Calculations of $A \leq 4$ Nuclei with an Artificial Neural-Network Correlator Ansatz". In: *Phys. Rev. Lett.* 127 (2 July 2021), p. 022502. DOI: 10.1103/PhysRevLett.127.022502. URL: https://link.aps.org/doi/10.1103/PhysRevLett.127.022502.

[85] Christopher Roth, Attila Szabó, and Allan H MacDonald. "High-accuracy variational Monte Carlo for frustrated magnets with deep neural networks". In: *Physical Review B* 108.5 (2023), p. 054410.

[86] Olga Sikora et al. "Variational Monte Carlo simulations using tensor-product projected states". In: *Phys. Rev. B* 91 (16 Apr. 2015), p. 165113. DOI: 10.1103/PhysRevB.91.165113. URL: https://link.aps.org/doi/10.1103/PhysRevB.91.165113.

[87] Erez Zohar and J. Ignacio Cirac. "Combining tensor networks with Monte Carlo methods for lattice gauge theories". In: *Phys. Rev. D* 97 (3 Feb. 2018), p. 034510. DOI: 10.1103/PhysRevD.97.034510. URL: https://link.aps.org/doi/10.1103/PhysRevD.97.034510.

[88] Patrick Emonts et al. "Variational Monte Carlo simulation with tensor networks of a pure $\mathbb{Z}_3$ gauge theory in $(2+1)$D". In: *Phys. Rev. D* 102 (7 Oct. 2020), p. 074501. DOI: 10.1103/PhysRevD.102.074501. URL: https://link.aps.org/doi/10.1103/PhysRevD.102.074501.

[89] Anders W Sandvik. “Computational studies of quantum spin systems”. In: *AIP Conference Proceedings*. Vol. 1297. 1. American Institute of Physics. 2010, pp. 135–338.

[90] Julien Toulouse, Roland Assaraf, and Cyrus J Umrigar. “Introduction to the variational and diffusion Monte Carlo methods”. In: *Advances in Quantum Chemistry*. Vol. 73. Elsevier, 2016, pp. 285–314.

[91] G Sugiyama and SE Koonin. “Auxiliary field Monte-Carlo for quantum many-body ground states”. In: *Annals of Physics* 168.1 (1986), pp. 1–26.

[92] FF Assaad and HG Evertz. “World-line and determinantal quantum Monte Carlo methods for spins, phonons and electrons”. In: *Computational Many-Particle Physics*. Springer, 2008, pp. 277–356.

[93] Yasir Iqbal et al. “Gutzwiller projected states for the J 1- J 2 Heisenberg model on the Kagome lattice: Achievements and pitfalls”. In: *Physical Review B* 104.14 (2021), p. 144406.

[94] Paolo Zanardi and Nikola Paunkovi ć. “Ground state overlap and quantum phase transitions”. In: *Phys. Rev. E* 74 (3 Sept. 2006), p. 031123. DOI: 10.1103/PhysRevE.74.031123. URL: https://link.aps.org/doi/10.1103/PhysRevE.74.031123.

[95] Yi Zhang et al. “Quasiparticle statistics and braiding from ground-state entanglement”. In: *Phys. Rev. B* 85 (23 June 2012), p. 235151. DOI: 10.1103/PhysRevB.85.235151. URL: https://link.aps.org/doi/10.1103/PhysRevB.85.235151.

[96] Jia-Wei Mei and Xiao-Gang Wen. “Modular matrices from universal wave-function overlaps in Gutzwiller-projected parton wave functions”. In: *Phys. Rev. B* 91 (12 Mar. 2015), p. 125123. DOI: 10.1103/PhysRevB.91.125123. URL: https://link.aps.org/doi/10.1103/PhysRevB.91.125123.

[97] Giuseppe Carleo et al. “Localization and Glassy Dynamics Of Many-Body Quantum Systems”. In: *Scientific Reports* 2.1 (Feb. 2012), p. 243. ISSN: 2045-2322. DOI: 10.1038/srep00243. URL: https://doi.org/10.1038/srep00243.

[98] Giuseppe Carleo et al. “Light-cone effect and supersonic correlations in one- and two-dimensional bosonic superfluids”. In: *Phys. Rev. A* 89 (3 Mar. 2014), p. 031602. DOI: 10.1103/PhysRevA.89.031602. URL: https://link.aps.org/doi/10.1103/PhysRevA.89.031602.

[99] Giuseppe Carleo et al. “Unitary Dynamics of Strongly Interacting Bose Gases with the Time-Dependent Variational Monte Carlo Method in Continuous Space”. In: *Phys. Rev. X* 7 (3 Aug. 2017), p. 031026. DOI: 10.1103/PhysRevX.7.031026. URL: https://link.aps.org/doi/10.1103/PhysRevX.7.031026.

[100] Tao Li and Fan Yang. “Variational study of the neutron resonance mode in the cuprate superconductors”. In: *Phys. Rev. B* 81 (21 June 2010), p. 214509. DOI: 10.1103/PhysRevB.81.214509. URL: https://link.aps.org/doi/10.1103/PhysRevB.81.214509.

[101] Francesco Ferrari et al. “Dynamical structure factor of the $J_1 - J_2$ Heisenberg model in one dimension: The variational Monte Carlo approach”. In: *Phys. Rev. B* 97 (23 June 2018), p. 235103. DOI: 10.1103/PhysRevB.97.235103. URL: https://link.aps.org/doi/10.1103/PhysRevB.97.235103.

[102] Francesco Ferrari and Federico Becca. “Dynamical Structure Factor of the $J_1 - J_2$ Heisenberg Model on the Triangular Lattice: Magnons, Spinons, and Gauge Fields”. In: *Phys. Rev. X* 9 (3 Aug. 2019), p. 031026. DOI: 10.1103/PhysRevX.9.031026. URL: https://link.aps.org/doi/10.1103/PhysRevX.9.031026.

[103] Yi Zhang, Tarun Grover, and Ashvin Vishwanath. “Entanglement Entropy of Critical Spin Liquids”. In: *Phys. Rev. Lett.* 107 (6 Aug. 2011), p. 067202. DOI: 10.1103/PhysRevLett.107.067202. URL: https://link.aps.org/doi/10.1103/PhysRevLett.107.067202.

[104] Yi Zhang, Tarun Grover, and Ashvin Vishwanath. “Topological entanglement entropy of $\mathbb{Z}_2$ spin liquids and lattice Laughlin states”. In: *Phys. Rev. B* 84 (7 Aug. 2011), p. 075128. DOI: 10.1103/PhysRevB.84.075128. URL: https://link.aps.org/doi/10.1103/PhysRevB.84.075128.

[105] Yoav Levine et al. “Quantum entanglement in deep learning architectures”. In: *Physical review letters* 122.6 (2019), p. 065301.

[106] Mari Carmen Banuls and Krzysztof Cichy. “Review on novel methods for lattice gauge theories”. In: *Reports on Progress in Physics* 83.2 (2020), p. 024401.

[107] Brian Swingle. “Entanglement renormalization and holography”. In: *Physical Review D—Particles, Fields, Gravitation, and Cosmology* 86.6 (2012), p. 065007.

[108] Steven R White. “Density matrix formulation for quantum renormalization groups”. In: *Physical review letters* 69.19 (1992), p. 2863.

[109] Steven R White. “Density-matrix algorithms for quantum renormalization groups”. In: *Physical review b* 48.14 (1993), p. 10345.

[110] Frank Verstraete and J Ignacio Cirac. “Renormalization algorithms for quantum-many body systems in two and higher dimensions”. In: *arXiv preprint cond-mat/0407066* (2004).

[111] J Ignacio Cirac et al. “Matrix product states and projected entangled pair states: Concepts, symmetries, theorems”. In: *Reviews of Modern Physics* 93.4 (2021), p. 045003.

[112] Philippe Corboz and Guifré Vidal. “Fermionic multiscale entanglement renormalization ansatz”. In: *Physical Review B—Condensed Matter and Materials Physics* 80.16 (2009), p. 165129.

[113] Christina V. Kraus et al. “Fermionic projected entangled pair states”. In: *Phys. Rev. A* 81 (5 May 2010), p. 052338. DOI: 10.1103/PhysRevA.81.052338. URL: https://link.aps.org/doi/10.1103/PhysRevA.81.052338.

[114] Philippe Corboz et al. “Simulation of strongly correlated fermions in two spatial dimensions with fermionic projected entangled-pair states”. In: *Physical Review B* 81.16 (2010), p. 165104.

[115] Norbert Schuch, Ignacio Cirac, and David Pérez-García. “PEPS as ground states: Degeneracy and topology”. In: *Annals of Physics* 325.10 (2010), pp. 2153–2192. ISSN: 0003-4916. DOI: https://doi.org/10.1016/j.aop.2010.05.008. URL: https://www.sciencedirect.com/science/article/pii/S0003491610000990.

[116] Ulrich Schollwöck. “The density-matrix renormalization group in the age of matrix product states”. In: *Annals of physics* 326.1 (2011), pp. 96–192.

[117] Román Orús. “A practical introduction to tensor networks: Matrix product states and projected entangled pair states”. In: *Annals of physics* 349 (2014), pp. 117–158.

[118] Mari Carmen Banuls. *Tensor Network States: basic introduction*. https://www.ggi.infn.it/sft/SFT_2022/Banuls-TNS-Lecture_Notes_220208.pdf. 2022.

[119] Guifré Vidal. “Class of quantum many-body states that can be efficiently simulated”. In: *Physical review letters* 101.11 (2008), p. 110501.

[120] Luca Bombelli et al. “Quantum source of entropy for black holes”. In: *Phys. Rev. D* 34 (2 July 1986), pp. 373–383. DOI: 10.1103/PhysRevD.34.373. URL: https://link.aps.org/doi/10.1103/PhysRevD.34.373.

[121] Matthew B Hastings. “An area law for one-dimensional quantum systems”. In: *Journal of statistical mechanics: theory and experiment* 2007.08 (2007), P08024.

[122] Nicolas Laflorencie. “Quantum entanglement in condensed matter systems”. In: *Physics Reports* 646 (2016), pp. 1–59.

[123] David Poulin et al. “Quantum Simulation of Time-Dependent Hamiltonians and the Convenient Illusion of Hilbert Space”. In: *Phys. Rev. Lett.* 106 (17 Apr. 2011), p. 170501. DOI: 10.1103/PhysRevLett.106.170501. URL: https://link.aps.org/doi/10.1103/PhysRevLett.106.170501.

[124] Frank Verstraete et al. “Criticality, the area law, and the computational power of projected entangled pair states”. In: *Physical review letters* 96.22 (2006), p. 220601.

[125] Norbert Schuch et al. “Resonating valence bond states in the PEPS formalism”. In: *Physical Review B—Condensed Matter and Materials Physics* 86.11 (2012), p. 115108.

[126] Michael A Nielsen and Isaac L Chuang. *Quantum computation and quantum information*. Cambridge university press, 2010.

[127] Hui Li and F Duncan M Haldane. “Entanglement Spectrum as a Generalization of Entanglement Entropy: Identification<? format?> of Topological Order in Non-Abelian Fractional Quantum Hall Effect States”. In: *Physical review letters* 101.1 (2008), p. 010504.

[128] J Ignacio Cirac et al. “Entanglement spectrum and boundary theories with projected entangled-pair states”. In: *Physical Review B—Condensed Matter and Materials Physics* 83.24 (2011), p. 245134.

[129] V. Murg, F. Verstraete, and J. I. Cirac. “Variational study of hard-core bosons in a two-dimensional optical lattice using projected entangled pair states”. In: *Phys. Rev. A* 75 (3 Mar. 2007), p. 033605. DOI: 10.1103/PhysRevA.75.033605. URL: https://link.aps.org/doi/10.1103/PhysRevA.75.033605.

[130] Jacob Jordan et al. “Classical simulation of infinite-size quantum lattice systems in two spatial dimensions”. In: *Physical review letters* 101.25 (2008), p. 250602.

[131] V. Zauner-Stauber et al. “Variational optimization algorithms for uniform matrix product states”. In: *Phys. Rev. B* 97 (4 Jan. 2018), p. 045145. DOI: 10.1103/PhysRevB.97.045145. URL: https://link.aps.org/doi/10.1103/PhysRevB.97.045145.

[132] Michael Levin and Cody P Nave. “Tensor renormalization group approach to two-dimensional classical lattice models”. In: *Physical review letters* 99.12 (2007), p. 120601.

[133] Z. Y. Xie et al. “Second Renormalization of Tensor-Network States”. In: *Phys. Rev. Lett.* 103 (16 Oct. 2009), p. 160601. DOI: 10.1103/PhysRevLett.103.160601. URL: https://link.aps.org/doi/10.1103/PhysRevLett.103.160601.

[134] Glen Evenbly and Guifre Vidal. “Local scale transformations on the lattice with tensor network renormalization”. In: *Physical review letters* 116.4 (2016), p. 040401.

[135] Shuo Yang, Zheng-Cheng Gu, and Xiao-Gang Wen. “Loop Optimization for Tensor Network Renormalization”. In: *Phys. Rev. Lett.* 118 (11 Mar. 2017), p. 110504. DOI: 10.1103/PhysRevLett.118.110504. URL: https://link.aps.org/doi/10.1103/PhysRevLett.118.110504.

[136] T. Nishino, K. Okunishi, and M. Kikuchi. “Numerical renormalization group at criticality”. In: *Physics Letters A* 213.1 (1996), pp. 69–72. ISSN: 0375-9601. DOI: https://doi.org/10.1016/0375-9601(96)00128-4. URL: https://www.sciencedirect.com/science/article/pii/0375960196001284.

[137] Román Orús and Guifré Vidal. “Simulation of two-dimensional quantum systems on an infinite lattice revisited: Corner transfer matrix for tensor contraction”. In: *Phys. Rev. B* 80 (9 Sept. 2009), p. 094403. DOI: 10.1103/PhysRevB.80.094403. URL: https://link.aps.org/doi/10.1103/PhysRevB.80.094403.

[138] Michael P. Zaletel and Frank Pollmann. “Isometric Tensor Network States in Two Dimensions”. In: *Phys. Rev. Lett.* 124 (3 Jan. 2020), p. 037201. DOI: 10.1103/PhysRevLett.124.037201. URL: https://link.aps.org/doi/10.1103/PhysRevLett.124.037201.

[139] Tomotoshi Nishino and Kouichi Okunishi. “Corner transfer matrix renormalization group method”. In: *Journal of the Physical Society of Japan* 65.4 (1996), pp. 891–894.

[140] Tomotoshi Nishino and Kouichi Okunishi. “Corner transfer matrix algorithm for classical renormalization group”. In: *Journal of the Physical Society of Japan* 66.10 (1997), pp. 3040–3047.

[141] Rodney J Baxter. “Dimers on a rectangular lattice”. In: *Journal of Mathematical Physics* 9.4 (1968), pp. 650–654.

[142] Rodney J Baxter. “Variational approximations for square lattice models in statistical mechanics”. In: *Journal of Statistical Physics* 19 (1978), pp. 461–478.

[143] Sasank Budaraju, Didier Poilblanc, and Sen Niu. “Simulating chiral spin liquids with fermionic projected entangled pair states”. In: *Phys. Rev. B* 110 (6 Aug. 2024), p. 064402. DOI: 10.1103/PhysRevB.110.064402. URL: https://link.aps.org/doi/10.1103/PhysRevB.110.064402.

[144] X. G. Wen, Frank Wilczek, and A. Zee. “Chiral spin states and superconductivity”. In: *Phys. Rev. B* 39 (16 June 1989), pp. 11413–11423. DOI: 10.1103/PhysRevB.39.11413. URL: https://link.aps.org/doi/10.1103/PhysRevB.39.11413.

[145] Xiao-Gang Wen. “Gapless boundary excitations in the quantum Hall states and in the chiral spin states”. In: *Phys. Rev. B* 43.13 (1991), p. 11025.

[146] Bela Bauer et al. “Chiral spin liquid and emergent anyons in a Kagome lattice Mott insulator”. In: *Nature communications* 5.1 (2014), p. 5137.

[147] Alexander Wietek and Andreas M. Läuchli. “Chiral spin liquid and quantum criticality in extended $S = \frac{1}{2}$ Heisenberg models on the triangular lattice”. In: *Phys. Rev. B* 95 (3 Jan. 2017), p. 035141. DOI: 10.1103/PhysRevB.95.035141. URL: https://link.aps.org/doi/10.1103/PhysRevB.95.035141.

[148] Ciarán Hickey et al. “Emergence of chiral spin liquids via quantum melting of noncoplanar magnetic orders”. In: *Phys. Rev. B* 96 (11 Sept. 2017), p. 115115. DOI: 10.1103/PhysRevB.96.115115. URL: https://link.aps.org/doi/10.1103/PhysRevB.96.115115.

[149] Laura Messio et al. “Chiral Spin Liquid on a Kagome Antiferromagnet Induced by the Dzyaloshinskii-Moriya Interaction”. In: *Phys. Rev. Lett.* 118 (26 June 2017), p. 267201. DOI: 10.1103/PhysRevLett.118.267201. URL: https://link.aps.org/doi/10.1103/PhysRevLett.118.267201.

[150] Samuel Bieri, Claire Lhuillier, and Laura Messio. “Projective symmetry group classification of chiral spin liquids”. In: *Phys. Rev. B* 93 (9 Mar. 2016), p. 094437. DOI: 10.1103/PhysRevB.93.094437. URL: https://link.aps.org/doi/10.1103/PhysRevB.93.094437.

[151] Wen-Jun Hu, Shou-Shu Gong, and D. N. Sheng. “Variational Monte Carlo study of chiral spin liquid in quantum antiferromagnet on the triangular lattice”. In: *Phys. Rev. B* 94 (7 Aug. 2016), p. 075131. DOI: 10.1103/PhysRevB.94.075131. URL: https://link.aps.org/doi/10.1103/PhysRevB.94.075131.

[152] Alexander Wietek, Antoine Sterdyniak, and Andreas M. Läuchli. “Nature of chiral spin liquids on the kagome lattice”. In: *Phys. Rev. B* 92 (12 Sept. 2015), p. 125122. DOI: 10.1103/PhysRevB.92.125122. URL: https://link.aps.org/doi/10.1103/PhysRevB.92.125122.

[153] Hong Yao and Dung-Hai Lee. “Fermionic Magnons, Non-Abelian Spinons, and the Spin Quantum Hall Effect from an Exactly Solvable Spin-1/2 Kitaev Model with SU(2) Symmetry”. In: *Phys. Rev. Lett.* 107 (8 Aug. 2011), p. 087205. DOI: 10.1103/PhysRevLett.107.087205. URL: https://link.aps.org/doi/10.1103/PhysRevLett.107.087205.

[154] Ji-Yao Chen et al. “Abelian SU (N) 1 chiral spin liquids on the square lattice”. In: *Physical Review B* 104.23 (2021), p. 235104.

[155] Michael Hermele, Victor Gurarie, and Ana Maria Rey. “Mott Insulators of Ultracold Fermionic Alkaline Earth Atoms: Underconstrained Magnetism and Chiral Spin Liquid”. In: *Phys. Rev. Lett.* 103 (13 Sept. 2009), p. 135301. DOI: 10.1103/PhysRevLett.103.135301. URL: https://link.aps.org/doi/10.1103/PhysRevLett.103.135301.

[156] Pierre Nataf et al. “Chiral Spin Liquids in Triangular-Lattice SU(N) Fermionic Mott Insulators with Artificial Gauge Fields”. In: *Phys. Rev. Lett.* 117 (16 Oct. 2016), p. 167202. DOI: 10.1103/PhysRevLett.117.167202. URL: https://link.aps.org/doi/10.1103/PhysRevLett.117.167202.

[157] Ji-Yao Chen et al. “SU$(3)_1$ Chiral Spin Liquid on the Square Lattice: A View from Symmetric Projected Entangled Pair States”. In: *Phys. Rev. Lett.* 125 (1 June 2020), p. 017201. DOI: 10.1103/PhysRevLett.125.017201. URL: https://link.aps.org/doi/10.1103/PhysRevLett.125.017201.

[158] Ya-Hui Zhang, D. N. Sheng, and Ashvin Vishwanath. “SU(4) Chiral Spin Liquid, Exciton Supersolid, and Electric Detection in Moiré Bilayers”. In: *Phys. Rev. Lett.* 127 (24 Dec. 2021), p. 247701. DOI: 10.1103/PhysRevLett.127.247701. URL: https://link.aps.org/doi/10.1103/PhysRevLett.127.247701.

[159] Xu-Ping Yao, Yonghao Gao, and Gang Chen. "Topological chiral spin liquids and competing states in triangular lattice SU(N) Mott insulators". In: *Phys. Rev. Res.* 3 (2 May 2021), p. 023138. DOI: 10.1103/PhysRevResearch.3.023138. URL: https://link.aps.org/doi/10.1103/PhysRevResearch.3.023138.

[160] Gang Chen et al. "Synthetic-gauge-field stabilization of the chiral-spin-liquid phase". In: *Phys. Rev. A* 93 (6 June 2016), p. 061601. DOI: 10.1103/PhysRevA.93.061601. URL: https://link.aps.org/doi/10.1103/PhysRevA.93.061601.

[161] Michael Hermele and Victor Gurarie. "Topological liquids and valence cluster states in two-dimensional SU(N) magnets". In: *Phys. Rev. B* 84 (17 Nov. 2011), p. 174441. DOI: 10.1103/PhysRevB.84.174441. URL: https://link.aps.org/doi/10.1103/PhysRevB.84.174441.

[162] Yin-Chen He, D. N. Sheng, and Yan Chen. "Chiral Spin Liquid in a Frustrated Anisotropic Kagome Heisenberg Model". In: *Phys. Rev. Lett.* 112 (13 Apr. 2014), p. 137202. DOI: 10.1103/PhysRevLett.112.137202. URL: https://link.aps.org/doi/10.1103/PhysRevLett.112.137202.

[163] Wen-Jun Hu et al. "Variational Monte Carlo study of a chiral spin liquid in the extended Heisenberg model on the kagome lattice". In: *Phys. Rev. B* 91 (4 Jan. 2015), p. 041124. DOI: 10.1103/PhysRevB.91.041124. URL: https://link.aps.org/doi/10.1103/PhysRevB.91.041124.

[164] Yin-Chen He and Yan Chen. "Distinct Spin Liquids and Their Transitions in Spin-1/2 XXZ Kagome Antiferromagnets". In: *Phys. Rev. Lett.* 114 (3 Jan. 2015), p. 037201. DOI: 10.1103/PhysRevLett.114.037201. URL: https://link.aps.org/doi/10.1103/PhysRevLett.114.037201.

[165] Shou-Shu Gong et al. "Global phase diagram of competing ordered and quantum spin-liquid phases on the kagome lattice". In: *Phys. Rev. B* 91 (7 Feb. 2015), p. 075112. DOI: 10.1103/PhysRevB.91.075112. URL: https://link.aps.org/doi/10.1103/PhysRevB.91.075112.

[166] Shou-Shu Gong, Wei Zhu, and DN Sheng. "Emergent chiral spin liquid: Fractional quantum Hall effect in a kagome Heisenberg model". In: *Scientific reports* 4.1 (2014), p. 6317.

[167] Tigran A. Sedrakyan, Leonid I. Glazman, and Alex Kamenev. "Spontaneous Formation of a Nonuniform Chiral Spin Liquid in a Moat-Band Lattice". In: *Phys. Rev. Lett.* 114 (3 Jan. 2015), p. 037203. DOI: 10.1103/PhysRevLett.114.037203. URL: https://link.aps.org/doi/10.1103/PhysRevLett.114.037203.

[168] N. Y. Yao et al. "A quantum dipolar spin liquid". In: *Nature Physics* 14.4 (Apr. 2018), pp. 405–410. ISSN: 1745-2481. DOI: 10.1038/s41567-017-0030-7. URL: https://doi.org/10.1038/s41567-017-0030-7.

[169] Aaron Szasz et al. “Chiral Spin Liquid Phase of the Triangular Lattice Hubbard Model: A Density Matrix Renormalization Group Study”. In: *Phys. Rev. X* 10 (2 May 2020), p. 021042. DOI: 10.1103/PhysRevX.10.021042. URL: https://link.aps.org/doi/10.1103/PhysRevX.10.021042.

[170] Alexei Kitaev. “Anyons in an exactly solved model and beyond”. In: *Annals of Physics* 321.1 (2006). January Special Issue, pp. 2–111. ISSN: 0003-4916. DOI: https://doi.org/10.1016/j.aop.2005.10.005. URL: https://www.sciencedirect.com/science/article/pii/S0003491605002381.

[171] Hong Yao and Steven A. Kivelson. “Exact Chiral Spin Liquid with Non-Abelian Anyons”. In: *Phys. Rev. Lett.* 99 (24 Dec. 2007), p. 247203. DOI: 10.1103/PhysRevLett.99.247203. URL: https://link.aps.org/doi/10.1103/PhysRevLett.99.247203.

[172] Adolfo G. Grushin and Cécile Repellin. “Amorphous and Polycrystalline Routes toward a Chiral Spin Liquid”. In: *Phys. Rev. Lett.* 130 (18 May 2023), p. 186702. DOI: 10.1103/PhysRevLett.130.186702. URL: https://link.aps.org/doi/10.1103/PhysRevLett.130.186702.

[173] V. Peri et al. “Non-Abelian chiral spin liquid on a simple non-Archimedean lattice”. In: *Phys. Rev. B* 101 (4 Jan. 2020), p. 041114. DOI: 10.1103/PhysRevB.101.041114. URL: https://link.aps.org/doi/10.1103/PhysRevB.101.041114.

[174] M. A. Keskiner, O. Erten, and M. Ö. Oktel. “Kitaev-type spin liquid on a quasicrystal”. In: *Phys. Rev. B* 108 (10 Sept. 2023), p. 104208. DOI: 10.1103/PhysRevB.108.104208. URL: https://link.aps.org/doi/10.1103/PhysRevB.108.104208.

[175] G. Cassella et al. “An exact chiral amorphous spin liquid”. In: *Nature Communications* 14.1 (Oct. 2023), p. 6663. ISSN: 2041-1723. DOI: 10.1038/s41467-023-42105-9. URL: https://doi.org/10.1038/s41467-023-42105-9.

[176] Victor Chua and Gregory A. Fiete. “Exactly solvable topological chiral spin liquid with random exchange”. In: *Phys. Rev. B* 84 (19 Nov. 2011), p. 195129. DOI: 10.1103/PhysRevB.84.195129. URL: https://link.aps.org/doi/10.1103/PhysRevB.84.195129.

[177] Victor Chua, Hong Yao, and Gregory A. Fiete. “Exact chiral spin liquid with stable spin Fermi surface on the kagome lattice”. In: *Phys. Rev. B* 83 (18 May 2011), p. 180412. DOI: 10.1103/PhysRevB.83.180412. URL: https://link.aps.org/doi/10.1103/PhysRevB.83.180412.

[178] Jianlong Fu. “Exact chiral-spin-liquid state in a Kitaev-type spin model”. In: *Phys. Rev. B* 100 (19 Nov. 2019), p. 195131. DOI: 10.1103/PhysRevB.100.195131. URL: https://link.aps.org/doi/10.1103/PhysRevB.100.195131.

[179] Darrell F. Schroeter et al. “Spin Hamiltonian for which the Chiral Spin Liquid is the Exact Ground State”. In: *Phys. Rev. Lett.* 99 (9 Aug. 2007), p. 097202. DOI: 10.1103/PhysRevLett.99.097202. URL: https://link.aps.org/doi/10.1103/PhysRevLett.99.097202.

[180] Ronny Thomale et al. “Parent Hamiltonian for the chiral spin liquid”. In: *Phys. Rev. B* 80 (10 Sept. 2009), p. 104406. DOI: 10.1103/PhysRevB.80.104406. URL: https://link.aps.org/doi/10.1103/PhysRevB.80.104406.

[181] Martin Greiter, Darrell F. Schroeter, and Ronny Thomale. “Parent Hamiltonian for the non-Abelian chiral spin liquid”. In: *Phys. Rev. B* 89 (16 Apr. 2014), p. 165125. DOI: 10.1103/PhysRevB.89.165125. URL: https://link.aps.org/doi/10.1103/PhysRevB.89.165125.

[182] Frank Verstraete et al. “Criticality, the area law, and the computational power of projected entangled pair states”. In: *Phys. Rev. Lett.* 96.22 (2006), p. 220601.

[183] Didier Poilblanc, J Ignacio Cirac, and Norbert Schuch. “Chiral topological spin liquids with projected entangled pair states”. In: *Phys. Rev. B* 91.22 (2015), p. 224431.

[184] Didier Poilblanc, Norbert Schuch, and Ian Affleck. “$SU(2)_1$ chiral edge modes of a critical spin liquid”. In: *Phys. Rev. B* 93.17 (2016), p. 174414.

[185] Didier Poilblanc. “Investigation of the chiral antiferromagnetic Heisenberg model using projected entangled pair states”. In: *Phys. Rev. B* 96 (12 Sept. 2017), p. 121118. DOI: 10.1103/PhysRevB.96.121118. URL: https://link.aps.org/doi/10.1103/PhysRevB.96.121118.

[186] Sen Niu et al. “Chiral spin liquids on the kagome lattice with projected entangled simplex states”. In: *Physical Review B* 106.24 (2022), p. 245119.

[187] Shuo Yang et al. “Chiral projected entangled-pair state with topological order”. In: *Physical review letters* 114.10 (2015), p. 106803.

[188] Anne E. B. Nielsen, Germán Sierra, and J. Ignacio Cirac. “Local models of fractional quantum Hall states in lattices and physical implementation”. In: *Nature Communications* 4 (2013), p. 2864. DOI: 10.1038/ncomms3864. URL: http://dx.doi.org/10.1038/ncomms3864.

[189] Jianwei Yang, Zhao Liu, and Ling Wang. *Ground state phase diagram and the exotic phases in the spin-1/2 square lattice J_1-J_2-J_χ model*. 2024. eprint: arXiv:2401.03434 (cond-mat.str-el).

[190] Xiao-Tian Zhang et al. *Chiral spin liquid and quantum phase diagram of spin-1/2 J_1-J_2-J_χ model on the square lattice*. 2024. eprint: arXiv:2401.07461 (cond-mat.str-el).

[191] K. v. Klitzing, G. Dorda, and M. Pepper. “New Method for High-Accuracy Determination of the Fine-Structure Constant Based on Quantized Hall Resistance”. In: *Phys. Rev. Lett.* 45 (6 Aug. 1980), pp. 494–497. DOI: 10.1103/PhysRevLett.45.494. URL: https://link.aps.org/doi/10.1103/PhysRevLett.45.494.

[192] David J Thouless et al. “Quantized Hall conductance in a two-dimensional periodic potential”. In: *Physical review letters* 49.6 (1982), p. 405.

[193] F Duncan M Haldane. “Model for a quantum Hall effect without Landau levels: Condensed-matter realization of the" parity anomaly"”. In: *Physical review letters* 61.18 (1988), p. 2015.

[194] S. Pancharatnam. “Generalized theory of interference and its applications”. In: *Proceedings of the Indian Academy of Sciences - Section A* 44.6 (Dec. 1956), pp. 398–417. ISSN: 0370-0089. DOI: 10.1007/BF03046095. URL: https://doi.org/10.1007/BF03046095.

[195] M. V. Berry. “Quantal Phase Factors Accompanying Adiabatic Changes”. In: *Proceedings of the Royal Society of London. Series A, Mathematical and Physical Sciences* 392.1802 (2024/07/18/ 1984). Full publication date: Mar. 8, 1984, pp. 45–57. ISSN: 00804630. URL: http://www.jstor.org/stable/2397741.

[196] Di Xiao, Ming-Che Chang, and Qian Niu. “Berry phase effects on electronic properties”. In: *Rev. Mod. Phys.* 82 (3 July 2010), pp. 1959–2007. DOI: 10.1103/RevModPhys.82.1959. URL: https://link.aps.org/doi/10.1103/RevModPhys.82.1959.

[197] Yasuhiro Hatsugai. “Chern number and edge states in the integer quantum Hall effect”. In: *Physical review letters* 71.22 (1993), p. 3697.

[198] Cui-Zu Chang, Chao-Xing Liu, and Allan H MacDonald. “Colloquium: Quantum anomalous hall effect”. In: *Reviews of Modern Physics* 95.1 (2023), p. 011002.

[199] Monika Aidelsburger et al. “Realization of the Hofstadter Hamiltonian with ultracold atoms in optical lattices”. In: *Physical review letters* 111.18 (2013), p. 185301.

[200] Monika Aidelsburger et al. “Measuring the Chern number of Hofstadter bands with ultracold bosonic atoms”. In: *Nature Physics* 11.2 (2015), pp. 162–166.

[201] N. Regnault and B. Andrei Bernevig. “Fractional Chern Insulator”. In: *Phys. Rev. X* 1 (2 Dec. 2011), p. 021014. DOI: 10.1103/PhysRevX.1.021014. URL: https://link.aps.org/doi/10.1103/PhysRevX.1.021014.

[202] Titus Neupert et al. “Fractional (Chern and topological) insulators”. In: *Physica Scripta* 2015.T164 (2015), p. 014005.

[203] M. Z. Hasan and C. L. Kane. “Colloquium: Topological insulators”. In: *Rev. Mod. Phys.* 82 (4 Nov. 2010), pp. 3045–3067. DOI: 10.1103/RevModPhys.82.3045. URL: https://link.aps.org/doi/10.1103/RevModPhys.82.3045.

[204] R. Peierls. “Zur Theorie des Diamagnetismus von Leitungselektronen”. In: *Zeitschrift für Physik* 80.11 (Nov. 1933), pp. 763–791. ISSN: 0044-3328. DOI: 10.1007/BF01342591. URL: https://doi.org/10.1007/BF01342591.

[205] Yakir Aharonov and David Bohm. “Significance of electromagnetic potentials in the quantum theory”. In: *Physical review* 115.3 (1959), p. 485.

[206] Richard P. Feynman, Robert B. Leighton, and Matthew Sands. *The Feynman Lectures on Physics, Vol. III: Quantum Mechanics*. Reading, MA: Addison-Wesley, 1965. ISBN: 978-0-201-02118-2.

[207] Douglas R. Hofstadter. “Energy levels and wave functions of Bloch electrons in rational and irrational magnetic fields”. In: *Phys. Rev. B* 14 (6 Sept. 1976), pp. 2239–2249. DOI: 10.1103/PhysRevB.14.2239. URL: https://link.aps.org/doi/10.1103/PhysRevB.14.2239.

[208] Tomoki Ozawa et al. “Topological photonics”. In: *Rev. Mod. Phys.* 91 (1 Mar. 2019), p. 015006. DOI: 10.1103/RevModPhys.91.015006. URL: https://link.aps.org/doi/10.1103/RevModPhys.91.015006.

[209] Takahiro Fukui, Yasuhiro Hatsugai, and Hiroshi Suzuki. “Chern numbers in discretized Brillouin zone: efficient method of computing (spin) Hall conductances”. In: *Journal of the Physical Society of Japan* 74.6 (2005), pp. 1674–1677.

[210] Jerome Dubail and Nicholas Read. “Tensor network trial states for chiral topological phases in two dimensions and a no-go theorem in any dimension”. In: *Phys. Rev. B* 92.20 (2015), p. 205307.

[211] Thorsten B Wahl et al. “Projected entangled-pair states can describe chiral topological states”. In: *Phys. Rev. Lett.* 111.23 (2013), p. 236805.

[212] Juraj Hasik et al. “Simulating Chiral Spin Liquids with Projected Entangled-Pair States”. In: *Phys. Rev. Lett.* 129.11 (2022), p. 177201.

[213] Gregory H. Wannier. “The Structure of Electronic Excitation Levels in Insulating Crystals”. In: *Phys. Rev.* 52 (3 Aug. 1937), pp. 191–197. DOI: 10.1103/PhysRev.52.191. URL: https://link.aps.org/doi/10.1103/PhysRev.52.191.

[214] Nicola Marzari et al. “Maximally localized Wannier functions: Theory and applications”. In: *Reviews of Modern Physics* 84.4 (2012), pp. 1419–1475.

[215] Christian Brouder et al. “Exponential Localization of Wannier Functions in Insulators”. In: *Phys. Rev. Lett.* 98 (4 Jan. 2007), p. 046402. DOI: 10.1103/PhysRevLett.98.046402. URL: https://link.aps.org/doi/10.1103/PhysRevLett.98.046402.

[216] Ji-Yao Chen et al. “Non-Abelian chiral spin liquid in a quantum antiferromagnet revealed by an iPEPS study”. In: *Phys. Rev. B* 98.18 (2018), p. 184409.

[217] J Hasik and GB Mbeng. *peps-torch: A differentiable tensor network library for two-dimensional lattice models*. 2020.

[218] Ji-Yao Chen et al. "$SU(3)_1$ chiral spin liquid on the square lattice: A view from symmetric projected entangled pair states". In: *Phys. Rev. Lett.* 125.1 (2020), p. 017201.

[219] Sen Niu et al. "Chiral spin liquids with projected Gaussian fermionic entangled pair states". In: *Physical Review B* 109.8 (2024), p. L081107.

[220] Yi Zhang et al. "Quasiparticle statistics and braiding from ground-state entanglement". In: *Phys. Rev. B* 85 (23 June 2012), p. 235151. DOI: 10.1103/PhysRevB.85.235151. URL: https://link.aps.org/doi/10.1103/PhysRevB.85.235151.

[221] Philippe Francesco, Pierre Mathieu, and David Sénéchal. *Conformal field theory*. Springer Science & Business Media, 2012.

[222] Quinten Mortier et al. "Tensor networks can resolve Fermi surfaces". In: *Physical Review Letters* 129.20 (2022), p. 206401.

[223] Jheng-Wei Li, Jan von Delft, and Hong-Hao Tu. "$U(1)$-symmetric Gaussian fermionic projected entangled paired states and their Gutzwiller projection". In: *Physical Review B* 107.8 (2023), p. 085148.

[224] F. Becca and S. Sorella. *Quantum Monte Carlo Approaches for Correlated Systems*. Cambridge University Press, 2017. DOI: 10.1017/9781316417041. URL: https://www.cambridge.org/core/books/quantum-monte-carlo-approaches-for-correlated-systems/EB88C86BD9553A0738BDAE400D0B2900.

[225] Hai-Jun Liao et al. "Differentiable programming tensor networks". In: *Phys. Rev. X* 9.3 (2019), p. 031041.

[226] Tomotoshi Nishino and Kouichi Okunishi. "Corner transfer matrix renormalization group method". In: *Journal of the Physical Society of Japan* 65.4 (1996), pp. 891–894.

[227] Philippe Corboz, T Maurice Rice, and Matthias Troyer. "Competing states in the t-J model: Uniform D-wave state versus stripe state". In: *Phys. Rev. Lett.* 113.4 (2014), p. 046402.

[228] Yi Zhang, Tarun Grover, and Ashvin Vishwanath. "Topological entanglement entropy of $\mathbb{Z}_2$ spin liquids and lattice Laughlin states". In: *Physical Review B* 84.7 (2011), p. 075128.

[229] Jia-Wei Mei and Xiao-Gang Wen. "Modular matrices from universal wave-function overlaps in Gutzwiller-projected parton wave functions". In: *Physical Review B* 91.12 (2015), p. 125123.

[230] X. G. Wen and Q. Niu. "Ground-state degeneracy of the fractional quantum Hall states in the presence of a random potential and on high-genus Riemann surfaces". In: *Phys. Rev. B* 41 (13 May 1990), pp. 9377–9396. DOI: 10.1103/PhysRevB.41.9377. URL: https://link.aps.org/doi/10.1103/PhysRevB.41.9377.

[231] Leticia Tarruell and Laurent Sanchez-Palencia. “Quantum simulation of the Hubbard model with ultracold fermions in optical lattices”. In: *Comptes Rendus Physique* 19.6 (2018). Quantum simulation / Simulation quantique, pp. 365–393. ISSN: 1631-0705. DOI: https://doi.org/10.1016/j.crhy.2018.10.013. URL: https://www.sciencedirect.com/science/article/pii/S1631070518300926.

[232] Xiqiao Wang et al. “Experimental realization of an extended Fermi-Hubbard model using a 2D lattice of dopant-based quantum dots”. In: *Nature Communications* 13.1 (Nov. 2022), p. 6824. ISSN: 2041-1723. DOI: 10.1038/s41467-022-34220-w. URL: https://doi.org/10.1038/s41467-022-34220-w.

[233] Benjamin M. Spar et al. “Realization of a Fermi-Hubbard Optical Tweezer Array”. In: *Phys. Rev. Lett.* 128 (22 June 2022), p. 223202. DOI: 10.1103/PhysRevLett.128.223202. URL: https://link.aps.org/doi/10.1103/PhysRevLett.128.223202.

[234] Anna Hackenbroich, Antoine Sterdyniak, and Norbert Schuch. “Interplay of SU(2), point group, and translational symmetry for projected entangled pair states: Application to a chiral spin liquid”. In: *Phys. Rev. B* 98.8 (2018), p. 085151.

[235] Ari M Turner, Yi Zhang, and Ashvin Vishwanath. “Entanglement and inversion symmetry in topological insulators”. In: *Physical Review B* 82.24 (2010), p. 241102.

[236] Lukasz Fidkowski. “Entanglement spectrum of topological insulators and superconductors”. In: *Physical review letters* 104.13 (2010), p. 130502.

[237] Xiao-Liang Qi, Hosho Katsura, and Andreas WW Ludwig. “General relationship between the entanglement spectrum and the edge state spectrum of topological quantum states”. In: *Physical review letters* 108.19 (2012), p. 196402.

[238] Didier Poilblanc. “Entanglement spectra of quantum Heisenberg ladders”. In: *Physical review letters* 105.7 (2010), p. 077202.

[239] Frank Pollmann et al. “Entanglement spectrum of a topological phase in one dimension”. In: *Physical Review B—Condensed Matter and Materials Physics* 81.6 (2010), p. 064439.

[240] Yin-Chen He, D. N. Sheng, and Yan Chen. “Chiral Spin Liquid in a Frustrated Anisotropic Kagome Heisenberg Model”. In: *Phys. Rev. Lett.* 112 (13 Apr. 2014), p. 137202. DOI: 10.1103/PhysRevLett.112.137202. URL: https://link.aps.org/doi/10.1103/PhysRevLett.112.137202.

[241] Wei-Lin Tu et al. “Competing orders in the Hofstadter t-J model”. In: *Phys. Rev. B* 97 (3 Jan. 2018), p. 035154. DOI: 10.1103/PhysRevB.97.035154. URL: https://link.aps.org/doi/10.1103/PhysRevB.97.035154.

[242] Y. Iqbal et al. “Gapless spin-liquid phase in the kagome spin-$\frac{1}{2}$ Heisenberg antiferromagnet”. In: *Phys. Rev. B* 87 (6 Feb. 2013), p. 060405. DOI: 10.1103/PhysRevB.87.060405. URL: https://link.aps.org/doi/10.1103/PhysRevB.87.060405.

[243] Yasir Iqbal et al. “Spin liquid nature in the Heisenberg J_1-J_2 triangular antiferromagnet”. In: *Phys. Rev. B* 93 (14 Apr. 2016), p. 144411. DOI: 10.1103/PhysRevB.93.144411. URL: https://link.aps.org/doi/10.1103/PhysRevB.93.144411.

[244] Shijie Hu et al. “Dirac Spin Liquid on the Spin-1/2 Triangular Heisenberg Antiferromagnet”. In: *Phys. Rev. Lett.* 123 (20 Nov. 2019), p. 207203. DOI: 10.1103/PhysRevLett.123.207203. URL: https://link.aps.org/doi/10.1103/PhysRevLett.123.207203.

[245] P. Lecheminant et al. “Order versus disorder in the quantum Heisenberg antiferromagnet on the kagomé lattice using exact spectra analysis”. In: *Phys. Rev. B* 56 (5 Aug. 1997), pp. 2521–2529. DOI: 10.1103/PhysRevB.56.2521. URL: https://link.aps.org/doi/10.1103/PhysRevB.56.2521.

[246] Andreas M. Läuchli, Julien Sudan, and Roderich Moessner. “$S = \frac{1}{2}$ kagome Heisenberg antiferromagnet revisited”. In: *Phys. Rev. B* 100 (15 Oct. 2019), p. 155142. DOI: 10.1103/PhysRevB.100.155142. URL: https://link.aps.org/doi/10.1103/PhysRevB.100.155142.

[247] S. Yan, D. A. Huse, and S. R. White. “Spin-Liquid Ground State of the $S = 1/2$ Kagome Heisenberg Antiferromagnet”. In: *Science* 332.6034 (2011), pp. 1173–1176. DOI: 10.1126/science.1201080. URL: https://science.sciencemag.org/content/332/6034/1173.

[248] S. Depenbrock, I.P. McCulloch, and U. Schollwöck. “Nature of the Spin-Liquid Ground State of the $S = 1/2$ Heisenberg Model on the Kagome Lattice”. In: *Phys. Rev. Lett.* 109 (6 Aug. 2012), p. 067201. DOI: 10.1103/PhysRevLett.109.067201. URL: https://link.aps.org/doi/10.1103/PhysRevLett.109.067201.

[249] Y.-C. He et al. “Signatures of Dirac Cones in a DMRG Study of the Kagome Heisenberg Model”. In: *Phys. Rev. X* 7 (3 July 2017), p. 031020. DOI: 10.1103/PhysRevX.7.031020. URL: https://link.aps.org/doi/10.1103/PhysRevX.7.031020.

[250] H.J. Liao et al. “Gapless Spin-Liquid Ground State in the $S = 1/2$ Kagome Antiferromagnet”. In: *Phys. Rev. Lett.* 118 (13 Mar. 2017), p. 137202. DOI: 10.1103/PhysRevLett.118.137202. URL: https://link.aps.org/doi/10.1103/PhysRevLett.118.137202.

[251] Max Hering et al. “Characterization of quantum spin liquids and their spinon band structures via functional renormalization”. In: *Phys. Rev. B* 99 (10 Mar. 2019), p. 100405. DOI: 10.1103/PhysRevB.99.100405. URL: https://link.aps.org/doi/10.1103/PhysRevB.99.100405.

[252] Zhenyue Zhu and Steven R. White. “Spin liquid phase of the $S = \frac{1}{2}$ $J_1 - J_2$ Heisenberg model on the triangular lattice”. In: *Phys. Rev. B* 92 (4 July 2015), p. 041105. DOI: 10.1103/PhysRevB.92.041105. URL: https://link.aps.org/doi/10.1103/PhysRevB.92.041105.

[253] Wen-Jun Hu et al. “Competing spin-liquid states in the spin-$\frac{1}{2}$ Heisenberg model on the triangular lattice”. In: *Phys. Rev. B* 92 (14 Oct. 2015), p. 140403. DOI: 10.1103/PhysRevB.92.140403. URL: https://link.aps.org/doi/10.1103/PhysRevB.92.140403.

[254] Alexander Wietek, Sylvain Capponi, and Andreas M. Läuchli. “Quantum Electrodynamics in $2+1$ Dimensions as the Organizing Principle of a Triangular Lattice Antiferromagnet”. In: *Phys. Rev. X* 14 (2 Apr. 2024), p. 021010. DOI: 10.1103/PhysRevX.14.021010. URL: https://link.aps.org/doi/10.1103/PhysRevX.14.021010.

[255] Francesco Ferrari and Federico Becca. “Dynamical Structure Factor of the $J_1 - J_2$ Heisenberg Model on the Triangular Lattice: Magnons, Spinons, and Gauge Fields”. In: *Phys. Rev. X* 9 (3 Aug. 2019), p. 031026. DOI: 10.1103/PhysRevX.9.031026. URL: https://link.aps.org/doi/10.1103/PhysRevX.9.031026.

[256] Markus Drescher et al. “Dynamical signatures of symmetry-broken and liquid phases in an $S = \frac{1}{2}$ Heisenberg antiferromagnet on the triangular lattice”. In: *Phys. Rev. B* 108 (22 Dec. 2023), p. L220401. DOI: 10.1103/PhysRevB.108.L220401. URL: https://link.aps.org/doi/10.1103/PhysRevB.108.L220401.

[257] Laura Messio, Bernard Bernu, and Claire Lhuillier. “Kagome Antiferromagnet: A Chiral Topological Spin Liquid?” In: *Phys. Rev. Lett.* 108 (20 May 2012), p. 207204. DOI: 10.1103/PhysRevLett.108.207204. URL: https://link.aps.org/doi/10.1103/PhysRevLett.108.207204.

[258] Rong-Yang Sun et al. *Possible chiral spin liquid state in the $S = 1/2$ kagome Heisenberg model*. 2022. arXiv: 2203.07321 [cond-mat.str-el].

[259] Michael Hermele et al. “Stability of $U(1)$ spin liquids in two dimensions”. In: *Phys. Rev. B* 70 (21 Dec. 2004), p. 214437. DOI: 10.1103/PhysRevB.70.214437. URL: https://link.aps.org/doi/10.1103/PhysRevB.70.214437.

[260] Xue-Yang Song et al. “Unifying description of competing orders in two-dimensional quantum magnets”. In: *Nat. Commun.* 10.1 (2019), p. 4254. DOI: 10.1038/s41467-019-11727-3. URL: https://doi.org/10.1038/s41467-019-11727-3.

[261] Xue-Yang Song et al. “From Spinon Band Topology to the Symmetry Quantum Numbers of Monopoles in Dirac Spin Liquids”. In: *Phys. Rev. X* 10 (1 Feb. 2020), p. 011033. DOI: 10.1103/PhysRevX.10.011033. URL: https://link.aps.org/doi/10.1103/PhysRevX.10.011033.

[262] V. Borokhov, A. Kapustin, and X. Wu. “Topological Disorder Operators in Three-Dimensional Conformal Field Theory”. In: *J. High Energy Phys.* 2002.11 (Jan. 2003), p. 049. DOI: 10.1088/1126-6708/2002/11/049. URL: https://dx.doi.org/10.1088/1126-6708/2002/11/049.

[263] Norbert Schuch et al. “Topological Order in the Projected Entangled-Pair States Formalism: Transfer Operator and Boundary Hamiltonians”. In: *Phys. Rev. Lett.* 111 (9 Aug. 2013), p. 090501. DOI: 10.1103/PhysRevLett.111.090501. URL: https://link.aps.org/doi/10.1103/PhysRevLett.111.090501.